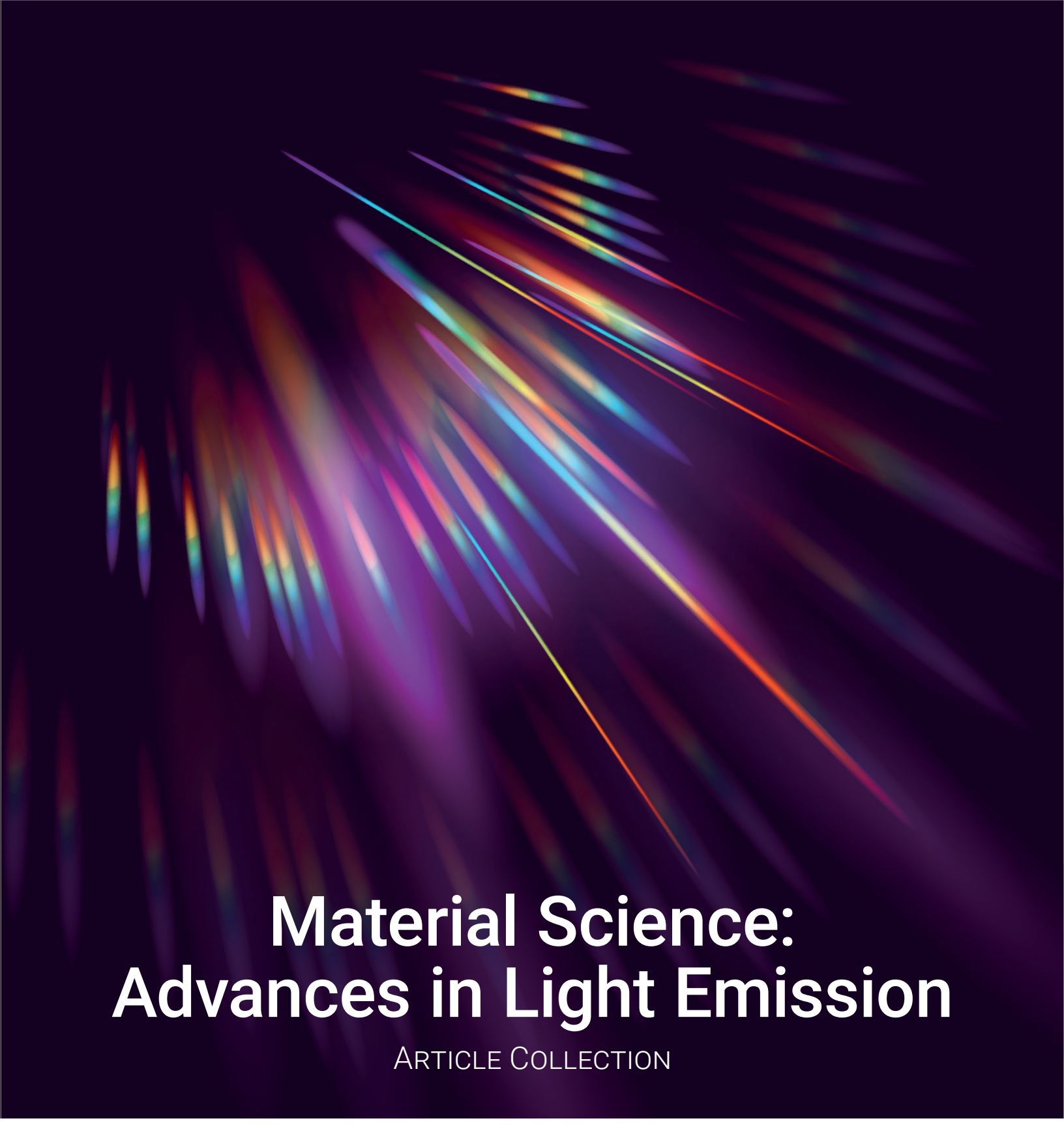

Material Science: Advances in Light Emission

Article Collection

ADVANCED MATERIALS

Sponsored by:

OXFORD INSTRUMENTS ANDOR

OXFORD INSTRUMENTS ANDOR

Spectroscopy Solutions for Material Science

Maximize Performance. **Advance Your Research**

- Sensitive **Cameras** - CCD, EMCCD, ICCD, InGaAs and sCMOS
- High-resolution Modular **Spectrographs**
- Cryogen-Free **Optical Cryostats** from <3k to 500k
- **Software / SDK** Platforms with rich functionality

Accurate. Flexible. Easy to use.

Find out more at **andor.oxinst.com**

Optical Cryostats

Spectrographs

Detectors

Contents

Introduction

In its broadest definition, materials science is the study of matter and its properties. Traditionally, the field was called metallurgy and included the study of metals. Nowadays, the field encompasses the study of all kinds of materials, including metals, ceramics, glasses, polymers, semiconductors, and nanomaterials. Materials scientists can now create materials with specific properties, which has led to the development of new and improved products in a wide range of industries.

In recent years, this field has seen tremendous growth, thanks to the development of nanomaterials and nanostructures with unique properties (optical or electrical) to solve problems in the fields of energy generation, semiconductors, quantum sources, chemical, catalysis, and biomedical industries.

In this article collection, we present recent discoveries in the electronic phase of Weyl semimetals, dielectric nano-resonators, low-cost solid-state light emitters, colloidal semiconductor quantum dots, and light-emitting field-effect transistors.

What you will learn:

- The applications of varied materials
- New developments in phase transitions and nanowires
- The challenges of colloidal quantum dots and light emitting diodes

References

Wang, M., Kumar, A., Dong, H., Woods, J.M., Pondick, J.V., Xu, S., Hynek, D.J., Guo, P., Qiu, D.Y. and Cha, J.J., 2022. A Gapped Phase in Semimetallic T_d-WTe_2 Induced by Lithium Intercalation. *Advanced Materials*, p.2200861.

Li, J., Yao, K., Huang, Y., Fang, J., Kollipara, P.S., Fan, D.E. and Zheng, Y., 2022. Tunable Strong Coupling in Transition Metal Dichalcogenide Nanowires. *Advanced Materials*, p.2200656.

Pradhan, S., Dalmases, M., Taghipour, N., Kundu, B. and Konstantatos, G., 2022. Colloidal Quantum Dot Light Emitting Diodes at Telecom Wavelength with 18% Quantum Efficiency and Over 1 MHz Bandwidth. *Advanced Science*, p.2200637.

Taghipour, N., Tanriover, I., Dalmases, M., Whitworth, G.L., Graham, C., Saha, A., Özdemir, O., Kundu, B., Pruneri, V., Aydin, K. and Konstantatos, G., 2022. Ultra-Thin Infrared Optical Gain Medium and Optically-Pumped Stimulated Emission in PbS Colloidal Quantum Dot LEDs. *Advanced Functional Materials*, p.2200832.

Bederak, D., Shulga, A., Kahmann, S., Talsma, W., Pelanskis, J., Dirin, D.N., Kovalenko, M.V. and Loi, M.A., 2022. Heterostructure from PbS Quantum Dot and Carbon Nanotube Inks for High-Efficiency Near-Infrared Light-Emitting Field-Effect Transistors. *Advanced Electronic Materials*, p.2101126.

ADVANCED MATERIALS
www.advmat.de

A Gapped Phase in Semimetallic T_d-WTe_2 Induced by Lithium Intercalation

*Mengjing Wang, Aakash Kumar, Hao Dong, John M. Woods, Joshua V. Pondick, Shiyu Xu, David J. Hynek, Peijun Guo, Diana Y. Qiu, and Judy J. Cha**

The Weyl semimetal WTe_2 has shown several correlated electronic behaviors, such as the quantum spin Hall effect, superconductivity, ferroelectricity, and a possible exciton insulator state, all of which can be tuned by various physical and chemical approaches. Here, a new electronic phase in WTe_2 induced by lithium intercalation is discovered. The new phase exhibits an increasing resistivity with decreasing temperature and its carrier density is almost two orders of magnitude lower than the carrier density of the semimetallic T_d phase, probed by in situ Hall measurements as a function of lithium intercalation. The theoretical calculations predict the new lithiated phase to be a potential charge density wave (CDW) phase with a bandgap of ≈0.14 eV, in good agreement with the in situ transport data. The new phase is structurally distinct from the initial T_d phase, characterized by polarization-angle-dependent Raman spectroscopy, and large lattice distortions close to 6% are predicted in the new phase. This finding of a new gapped phase in a 2D semimetal demonstrates electrochemical intercalation as a powerful tuning knob for modulating electron density and phase stability in 2D materials.

1. Introduction

2D orthorhombic tungsten ditelluride (T_d-WTe_2) is a type-II Weyl semimetal in bulk and a topological insulator as a monolayer, stimulating studies of quantum transport behaviors, such as the quantum spin Hall effect,[1] ferroelectricity,[2] exciton insulator,[3] unconventional charge spin conversion,[4] and spin–orbit torque.[5] Superconductivity observed in T_d-WTe_2 has also sparked interest for potential topological superconductivity.[6–8] Superconductivity with a T_c of 580 mK was first realized in monolayer T_d-WTe_2 by electrostatic doping at an electron density of 5×10^{12} e cm^{-2},[6,7] and T_c was raised to ≈2.6 K by chemical intercalation of potassium in bulk T_d-WTe_2 where the potassium is expected to donate charge to WTe_2.[9] With electron doping, a charge density wave (CDW) may also emerge in WTe_2 as several 2D chalcogenides, such as TaS_2, possess superconductivity as well as CDWs that are modulated by electron density.[10] Recent theoretical papers indeed predict that a high level of electron doping of over 10^{14} e cm^{-2} in monolayer T_d-WTe_2 can introduce lattice distortions and form a CDW phase, neighboring the superconducting dome at 10^{13} e cm^{-2}.[11,12] However, no experimental reports of a CDW phase in WTe_2 are found in the literature.

Here, we use lithium intercalation to modulate the carrier density of WTe_2 beyond the charge doping range achievable by ionic liquid gating and discover a new electronic phase in WTe_2, which we identify as a potential CDW phase. With controllable lithium intercalation and deintercalation, we observe a reversible structural and electronic phase transition as evidenced by in situ optical, Raman, and electrical transport characterization throughout the intercalation. Structurally, the new phase shows distinct Raman peaks with crystal symmetry different from the T_d symmetry, in agreement with the T_d' phase recently reported by Muscher et al.[13] Electronically, despite the significant electron doping by lithium, the new phase exhibits a reduction of electron carrier density by almost two orders of magnitude compared to the pristine semimetallic WTe_2 and increasing resistance with decreasing temperature, suggesting a bandgap opening. Our ab initio band structure computed within density functional theory (DFT) shows that the lithiated T_d' phase develops an indirect bandgap of 0.14 eV and a direct bandgap of 0.66 eV, consistent with the experimentally observed semiconductor-like electrical behavior. Furthermore, calculations of the phonon dispersion reveal that the T_d phase exhibits a phonon softening with lithium intercalation at the level of the experimental phase transition and at wave vectors roughly

M. Wang, A. Kumar, J. M. Woods, J. V. Pondick, S. Xu, D. J. Hynek, D. Y. Qiu, J. J. Cha
Department of Mechanical Engineering and Materials Science
Yale University
New Haven, CT 06511, USA
E-mail: judy.cha@yale.edu
M. Wang, A. Kumar, H. Dong, J. M. Woods, J. V. Pondick, S. Xu, D. J. Hynek, P. Guo, D. Y. Qiu, J. J. Cha
Energy Sciences Institute
Yale West Campus
West Haven, CT 06516, USA
H. Dong, P. Guo
Department of Chemical and Environmental Engineering
Yale University
New Haven, CT 06511, USA
The ORCID identification number(s) for the author(s) of this article can be found under https://doi.org/10.1002/adma.202200861.

DOI: 10.1002/adma.202200861

consistent with the formation of a 2 × 2 folding of the Brillouin zone. Concomitantly, lithiation stabilizes the T_d' phase, which is a 2 × 2 superlattice of the T_d phase involving a distortion of the W chain along *a*-axis where the W–Te–W bond lengths are shortened and elongated in their successive arrangements in contrast to the identical W–Te–W bond lengths in the T_d phase. Overall, the *a* and *c* lattice parameters are strained by 4.9% and 5.84% respectively when WTe_2 changes from the T_d to the T_d' phase. Thus, we report the first experimental evidence of a gapped phase, potential CDW, in WTe_2 enabled by lithium intercalation.

2. Results and Discussions

2.1. Lithium Intercalation Induced Phase Transition

For lithium intercalation, we construct a WTe_2 flake electrochemical cell using liquid or polymer gel electrolyte with capabilities of in situ Raman and in situ transport measurements (**Figure 1**a, Experimental Section). The exfoliated WTe_2 flakes have a lateral size distribution of 20–50 µm and a thickness range of 30–100 nm (>50 layers) (Figure S1, Supporting Information). By controlling the electrochemical intercalation voltage (V_{EC}) between the WTe_2 flake (cathode) and lithium metal (anode), lithium ions can be controllably inserted into the van der Waals gaps of the WTe_2 flake (Figure 1b). Lower values of V_{EC} represent more lithium ions intercalated into WTe_2 flakes.

A new structural phase emerges with distinct Raman modes at V_{EC} of 0.8 V vs Li^+/Li in a polymer cell (Figure 1c,d, Figure S2, Supporting Information) or at V_{EC} of 1.2 V vs Li^+/Li in a liquid cell (Figure S3, Supporting Information). In the low frequency region (<50 cm^{-1}) of the Raman spectrum where interlayer vibration modes are active, the shear mode of the T_d phase[14] at ≈8 cm^{-1} splits into two peaks at 6 and 13 cm^{-1}, as illustrated in Figure 1c. In the high frequency region (>50 cm^{-1}) where intralayer phonon modes are populated, several Raman modes with distinct peak positions appear (Figure 1d). These new Raman peaks do not match those observed in the initial T_d, 1T′, or 2H phases of WTe_2 (Table S1, Supporting Information). The Raman spectrum of the new phase has two key characteristics: increased number of Raman active modes compared to the T_d phase and no discernible patterns in the peak shifts of the Raman modes relative to the T_d phase. Therefore, the new Raman modes are not a result of strain or electron doping, but a manifestation of phase transition to a new phase with atomic configurations distinct from the T_d phase. Recently, Muscher

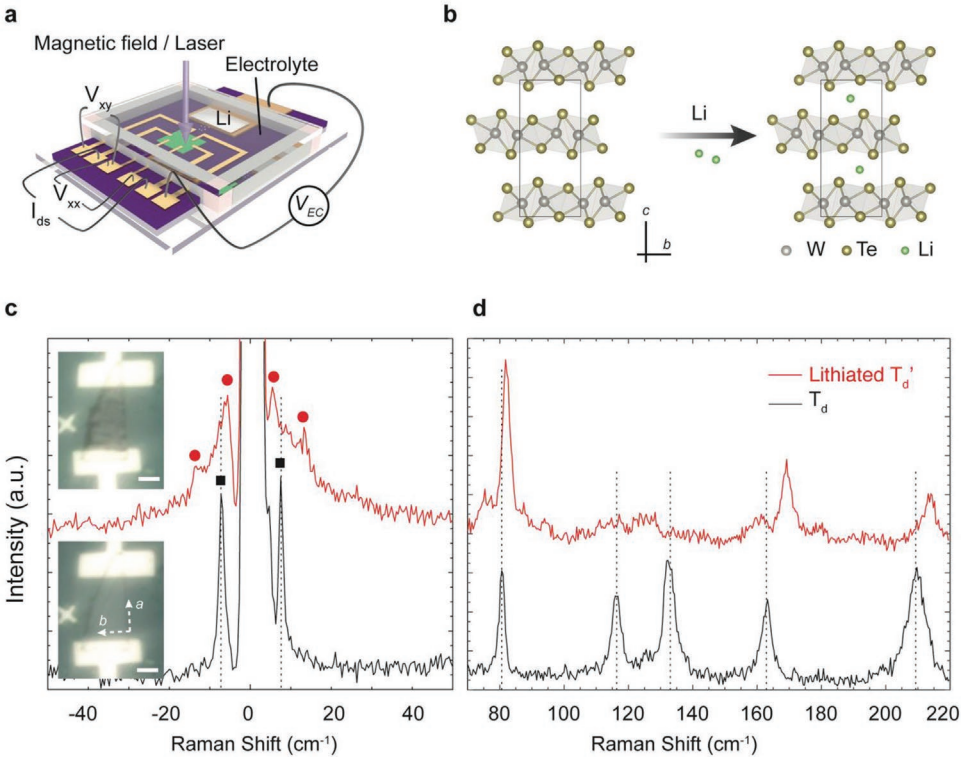

Figure 1. Phase transition in T_d-WTe_2 induced by lithium intercalation. a) Schematic of a lithium-ion electrochemical cell with capabilities of in situ Raman and in situ Hall measurements. V_{EC} represents the electrochemical intercalation voltage applied between the Li (silver rectangle) and WTe_2 (green rectangle). Adapted under the terms of the CC-BY Creative Commons Attribution 4.0 International license (https://creativecommons.org/licenses/by/4.0).[20] Copyright 2021, The Authors, published by Wiley-VCH. b) Side-view of lithium intercalation in the van der Waals gaps of T_d-WTe_2 (W: gray, Te: gold, Li: green). c,d) Low-frequency (c) and high-frequency (d) Raman spectra of the T_d phase (black, bottom) and lithiated T_d' phase (red, top). The insets in (c) are the corresponding optical images of the WTe_2 device before (bottom) and after (top) the phase transition. Scale bars: 10 µm. The red circles and black squares in (c) mark the positions of Raman active modes in T_d and the new phase, respectively. The black vertical dashed lines in (c) and (d) are visual guides for the positions of the Raman modes in the T_d phase.

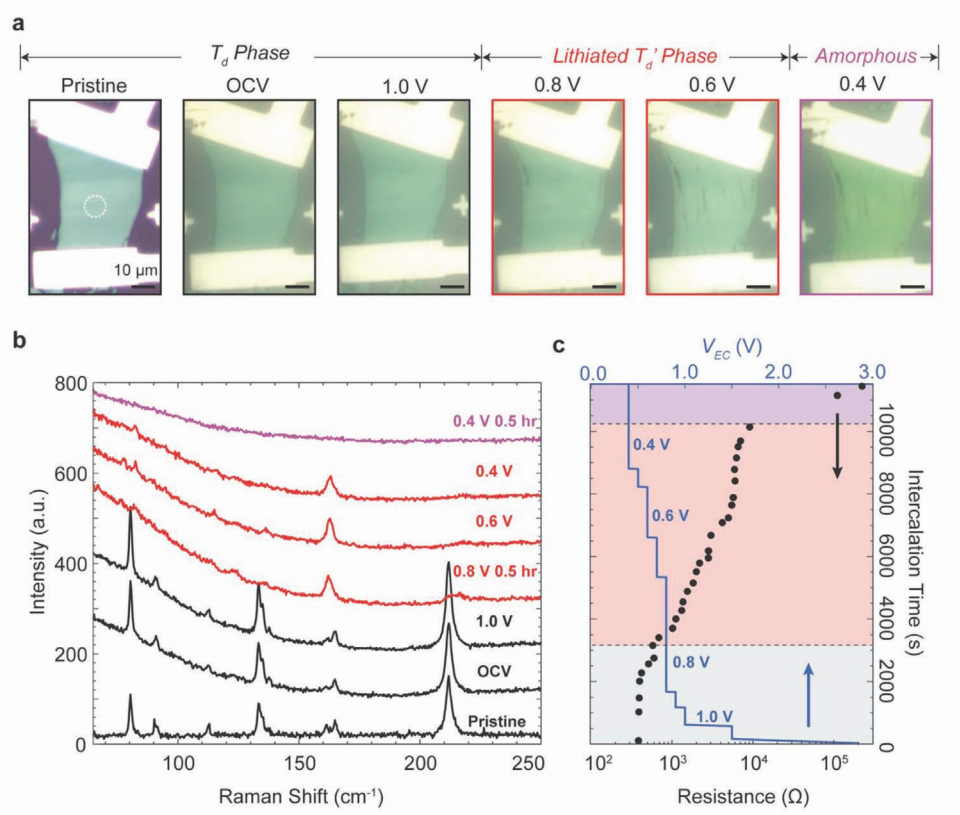

Figure 2. In situ optical characterization and two-terminal electrical transport measurements of a WTe_2 device as a function of electrochemical intercalation voltage. a) Optical images of a WTe_2 device as a function of intercalation driving voltage. According to the optical contrast, the intercalation consists of three stages: T_d phase (black framed), new phase (red framed), and amorphous state (purple framed). The white dashed circle denotes the position for in situ Raman data collection. b) Stacking plot of high-frequency Raman spectra as a function of intercalation voltage with the color scheme corresponding to the phase separation in (a). The background of the Raman spectra from OCV to 0.4 V comes from the polymer electrolyte. c) Simultaneous two-terminal resistance (solid black circles) as function of intercalation time with the intercalation direction lined up with the Raman stacking sequence in (b). The blue line is the profile of electrochemical intercalation voltage as a function of time. In line with (a) and (b), three phases are divided and colored correspondingly.

et al. reported a new lithiated T_d'-WTe_2 phase whose Raman modes match our experimental data (Table S1, Supporting Information).[13] Therefore, we identify the new lithiated phase in this work to be the same as that reported by Muscher et al. and henceforth refer to it as the lithiated T_d' phase (T_d' when referring to the structure without any Li atoms). Optically, when WTe_2 is in the lithiated T_d' phase, dark streaks appear along the crystallographic axis *b*, perpendicular to the direction of the W–W chain, as depicted in the inset of Figure 1c. A closer scrutinization of the streaks via scanning electron microscopy (Figure S4, Supporting Information) indicates them to be wrinkles, suggesting the cause of the dark streaks to be an anisotropic strain induced during the phase transition from T_d to T_d'.

A representative evolution of the high-frequency Raman peaks as V_{EC} is lowered from open-circuit voltage (OCV) to 0.4 V vs Li^+/Li in a polymer cell is shown in **Figure 2**b with corresponding optical images in Figure 2a. Three distinct stages take place in the course of lithium intercalation. First, WTe_2 remains in T_d phase when OCV > V_{EC} > 0.8V vs Li^+/Li with negligible changes in the Raman spectra and the optical contrast. In the second stage, when 0.8 V > V_{EC} > 0.4 V vs Li^+/Li, WTe_2 is in the new lithiated T_d' phase characterized by the distinct Raman modes and dark streaks appearing along the *b* axis (Figure 2a). Lastly, when V_{EC} < 0.4 V vs Li^+/Li, WTe_2 becomes amorphous, supported by the featureless Raman spectrum and a yellowish hue color change in WTe_2.

The resistance of the WTe_2 flake undergoing the phase transition was simultaneously tracked by two-terminal measurements of the same device (Figure 2c). First, the resistance does not change much while WTe_2 remains in the T_d phase (gray shaded region). While V_{EC} is at 0.8 V vs Li^+/Li, the resistance starts to increase from 386 Ω at ≈2000 s to 1015 Ω at ≈3000 s. This resistance increase is surprising as lithium intercalation in transition metal dichalcogenides (such as MoS_2) generally leads to a decreased resistivity due to the extra electrons donated by Li.[15] When WTe_2 is in the lithiated T_d' phase with the distinct Raman modes (V_{EC} = 0.8 V vs Li^+/Li between 3000 s to 10 000 s, pink shaded region), the resistance continues to increase and eventually saturates at 7032 Ω, a nearly twenty times increase in resistance from the pristine T_d phase. The saturated resistance indicates a completion of the phase transition. At V_{EC} of 0.4 vs Li^+/Li, WTe_2 starts to break down and becomes amorphous,

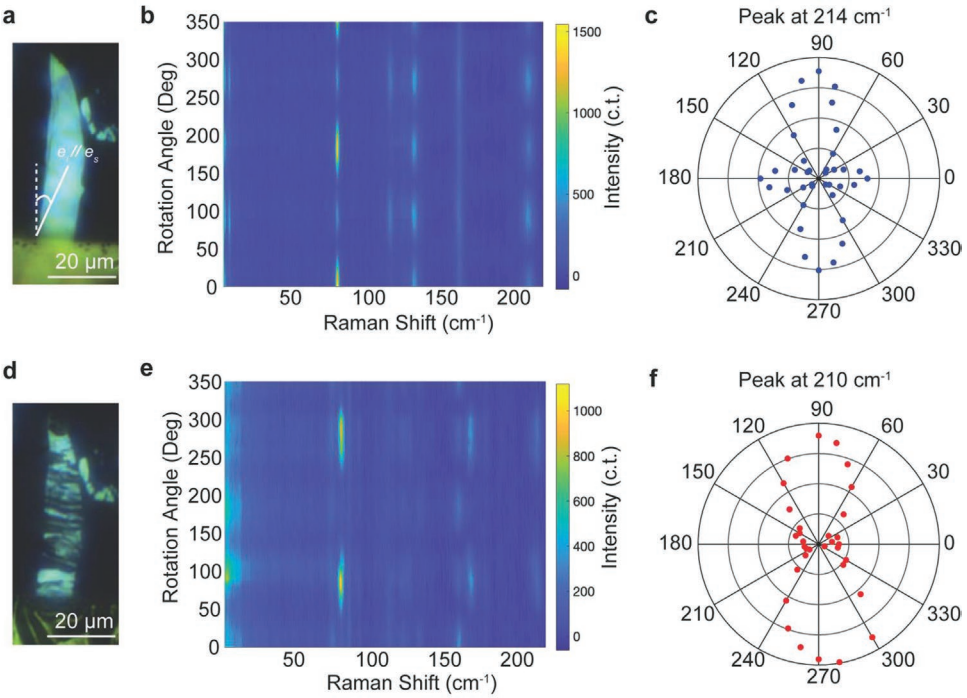

Figure 3. a–f) Angle-resolved Raman characterization of T_d (a–c) and lithiated T_d'-WTe_2 (d–f). a,d) Optical images of the WTe_2 flake in the pristine T_d (a) and lithiated T_d' (d) phase, respectively. The angle is defined as the angle between the vertical white dashed line and the polarization direction of the incident/scattered beam in (a). b,e) Angle-resolved Raman spectral maps of the T_d (b) and lithiated T_d' (e) phases, respectively. c,f) Ppole graphs of the Raman peak centered around 210 cm^{-1} in the T_d (c) and lithiated T_d' (f) phases, respectively.

accompanied with an irreversible sharp increase in resistance (purple shaded region).

For further characterization of the crystal structure and the electronic band structure of the lithiated T_d' phase, we performed in situ angle-resolved Raman spectroscopy and in situ magneto-transport measurements, which we discuss in the following sections.

2.2. In Situ Angle-Resolved Raman Spectroscopy of the Lithiated T_d' Phase

To characterize the crystal symmetry of the new phase, we performed in situ angle-resolved Raman spectroscopy, as presented in **Figure 3** (full spectra in Figure S5, Supporting Information). As a function of the angle θ between the polarization direction of the incident laser and the vertical dashed line shown in Figure 3a, we acquired the angle-dependent Raman spectra of the pristine T_d phase (Figure 3b) and the lithiated T_d' phase (Figure 3e). The lithiated T_d' phase has more Raman active modes, albeit with weaker intensities, than T_d in the range from 50 to 220 cm^{-1}, suggesting a lower crystal symmetry of the T_d' phase. Additionally, the symmetry of the prominent Raman modes is two-fold in the lithiated T_d' phase, such as the peaks centered at 80 and 210 cm^{-1}, while the symmetry of the Raman modes is mostly four-fold in the T_d phase, e.g., peaks at 75, 130, and 214 cm^{-1}. The pole graphs of the Raman modes near 210 cm^{-1} clearly show the four-lobed and two-lobed nature of the Raman modes in the T_d and lithiated T_d' phase, respectively (Figure 3c,f).

2.3. In Situ Magneto-Transport Measurements during Lithium Intercalation

The twenty-fold resistance increase of WTe_2 from the initial T_d phase to the lithiated T_d' phase suggests there may be a significant change in the electronic band structure of WTe_2 in the new T_d' phase. To answer this, we carried out in situ magneto-transport measurements of a WTe_2 flake as a function of Li intercalation.

Prior to intercalation, magneto-transport of a pristine WTe_2 flake was measured at 2 K, which showed clear Shubnikov–de Haas oscillations in high magnetic fields (Figures S6 and S7, Supporting Information), suggesting a high crystal quality of WTe_2. Fitting the R_{xx} and R_{xy} to a two-band transport model[16,17] showed that the pristine WTe_2 flake has an almost equally compensated electron and hole density at 2 K ($n_e = 2.11 \times 10^{20}$ cm^{-3}; $n_h = 1.97 \times 10^{20}$ cm^{-3}; Figure S6, Supporting Information). The nearly balanced electron and hole population indicates that the Fermi level (E_F) is close to zero in pristine WTe_2 intersecting the conduction band and valence band equally at 2 K, as predicted by DFT[16] and visualized in **Figure 4**a. At 300 K, transport data of the pristine WTe_2 flake suggests that electrons are populated more than holes (Figure S8f,g, Supporting Information) and thereby conduction is primarily carried out by electrons at room temperature.

During intercalation, both R_{xx} and R_{xy} were measured in the magnetic field of 3 T at 300 K as V_{EC} was swept from OCV to 0.8 V, as displayed in Figure 4c,d. In accordance with the Raman observation that new Raman modes from T_d' emerge when V_{EC}

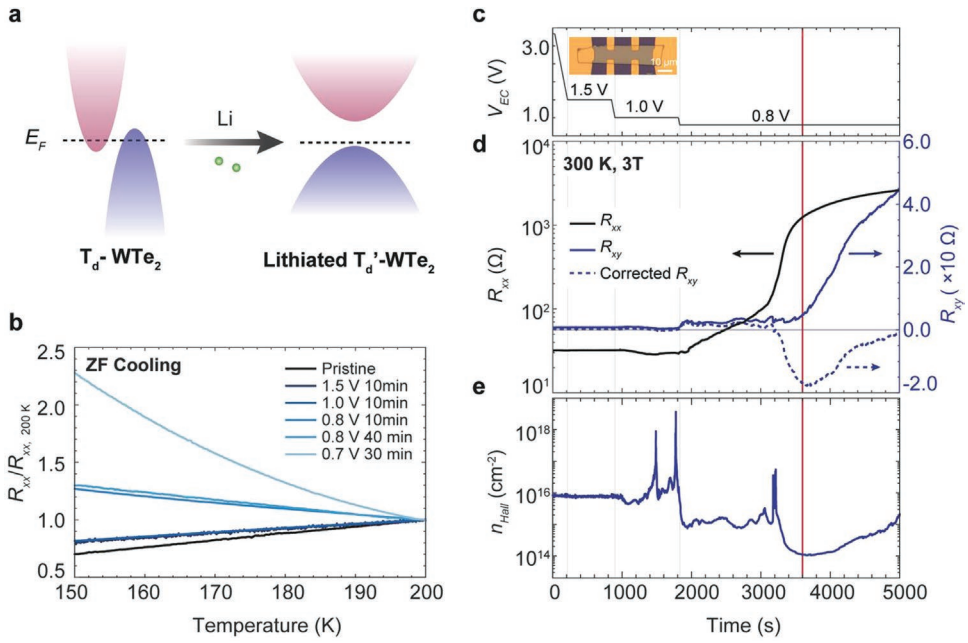

Figure 4. In situ Hall measurement of a WTe_2 device as a function of lithiation at 300 K. a) Schematic of electronic band structure changes during the phase transition from T_d-WTe_2 to lithiated T_d'-WTe_2. b). Zero-field (ZF) cooling curves of R_{xx} at the pristine state (black) and various stages of intercalation (blue). A limited temperature window from 200 to 150 K was due to the polymer electrolyte instability below 150 K. c). Profile of electrochemical intercalation voltage as a function of intercalation time. d) Raw data of R_{xx} (black) and R_{xy} (blue), and corrected R_{xy} (blue dashed line, see the Experimental Section) as a function of intercalation time at 3 T and 300 K. The gray horizontal line marks the position of zero for R_{xy}. The inset shows an optical image of a WTe_2 Hall bar device. e) Carrier density determined from corrected R_{xy} as a function of intercalation time. The light gray vertical lines in (c)–(e) mark the time of applying each new intercalation voltage. The dark red vertical line in (c)–(e) denotes the time when new Raman modes emerge.

stays at 0.8 V for 30 min, the red vertical line in Figure 4c,d marks the phase transition point from the T_d to the lithiated T_d' phase. When WTe_2 stays in T_d during OCV > V_{EC} > 0.8 V vs Li^+/Li, R_{xx} remains almost unchanged and decreases marginally at 1.0 V vs Li^+/Li from 32 to 28 Ω, likely due to electron doping from Li. At V_{EC} of 0.8 V vs Li^+/Li, R_{xx} rises immediately and saturates at 2620 Ω after 50 min at 0.8 V vs Li^+/Li, indicating a completion of phase transition from T_d to lithiated T_d' phase. The increase of R_{xx} measured with four probes agrees with the two-terminal measurement shown in Figure 2c.

Unlike the steady increase of R_{xx} at V_{EC} = 0.8 V vs Li^+/Li, the Hall resistance R_{xy} shows a plateau that lasts about 30 min before it starts to increase. According to the in situ Raman data, WTe_2 stays as T_d phase during the first 30 mins at V_{EC} = 0.8 V. Therefore, the plateau region of R_{xy} suggests a potential intermediate WTe_2 phase, which does not have drastic lattice rearrangements that can be detected by Raman spectroscopy but possesses a distinct electron band structure from that of T_d. After the plateau, R_{xy} increases and eventually saturates at 45 Ω in the new T_d' phase. After removing the contribution from R_{xx} due to the imperfect alignment of the Hall electrodes (see the Experimental Section), the plateau region persists in the corrected R_{xy}, but the sign changes from positive to negative in the new T_d' phase, suggesting a hole-dominated transport (Figure S9, Supporting Information). Figure 4e shows the Hall carrier density (n_{Hall}) determined from the corrected R_{xy}. When OCV > V_{EC} > 0.8 V vs Li^+/Li, n_{Hall} remains unchanged at 7.6 × 10^{15} cm^{-2} as WTe_2 is in the T_d phase. Assuming the thickness of the flake to be between 50 to 100 nm from the Raman characterization and the color of the flake (Figure S1, Supporting Information), the corresponding 3D carrier density falls in the range of 0.76–1.5 × 10^{21} cm^{-3}. The spikes seen in n_{Hall} correspond to the regions where the differences of R_{xy} values between 3 and 0 T are very small, and therefore are artifacts and not physically meaningful. At the onset of V_{EC} = 0.8 V, n_{Hall} falls considerably to 9.1 × 10^{14} cm^{-2} and remains at this density. After ≈30 min at V_{EC} = 0.8 V, WTe_2 is in the lithiated T_d' phase and n_{Hall} changes the sign with a further reduced hole carrier density of 1.9 × 10^{14} cm^{-2}.

The observed characteristics of R_{xx} and R_{xy} are reproduced in the second round of lithium intercalation (Figure S8a–c, Supporting Information) and in a different Hall bar device (Figure S10, Supporting Information), confirming the reversibility of the phase transition and ruling out the possibilities of electrical contact degradation for the observation. We also confirm that the electrical contacts remain unaffected by intercalation as the magneto-transport behaviors remain unchanged between pristine state and deintercalated state (Figure S8f,g, Supporting Information). Additionally, X-ray photoelectron spectroscopy (XPS) of the deintercalated device shows no significant change from the pristine state, except a slight electron doping effect from residual lithium as evidenced by a 0.4–1.0 eV downshift of the Te 3d binding energy (Figure S11, Supporting Information). Therefore, the increase of resistance and accompanying reduction of carrier density exclusively originate from the change in the electronic band

structure as WTe_2 changes to the new lithiated T_d' phase from the T_d phase.

The reduced carrier density and the change of the carrier type suggests a potential gap opening in initially semimetallic WTe_2. To test this hypothesis, temperature-dependent R_{xx} were acquired at pristine state (Figure S12, Supporting Information) as well as at various stages of intercalation by first halting the intercalation through rapid quenching to 200 K, as shown in Figure 4b. At OCV > V_{EC} > 0.8 V vs Li^+/Li, lithiated WTe_2 remains in the T_d phase and R_{xx} vs T curves show a metallic transport with decreasing resistance at lower temperatures. In contrast, at $V_{EC} \leq 0.8$ V vs Li^+/Li, the lithiated WTe_2 behaves like a semiconductor with resistance increasing with decreasing temperature. This suggests that the new lithiated T_d' phase has a bandgap, in contrast to the starting semimetallic T_d phase, as illustrated in Figure 4a. We note that the temperature range was limited to 150 K for transport measurements due to the sudden volume change of the polymer electrolyte at that temperature, which breaks the devices. The lithiated phase was measured down to 2 K using a poly(ethylene oxide) (PEO)–lithium bis(trifluoromethanesulfonyl)imide (LiTFSI) polymer electrolyte mixture, as shown in Figure S13 (Supporting Information).

We carried out DFT calculations of the electronic band structure of the T_d and T_d' phases (**Figure 5**a,b) to elucidate the origin of the dramatic differences in the electron transport of these phases. The lithiated T_d' phase has a simple monoclinic[13] conventional unit cell with twice the number of atoms of the orthorhombic T_d unit cell, as illustrated in Figure 5a,b. Detailed crystallographic information of T_d and lithiated T_d' is summarized in Tables S2 and S3 (Supporting Information). The computed band structure for pristine T_d phase in Figure 5c shows that the electron pocket is slightly larger than the hole pocket, consistent with our magneto-transport data of pristine T_d state. Moreover, the band structure of the lithiated T_d' phase in Figure 5d confirms that there is a gap opening in the lithiated T_d' phase with a direct gap of 0.66 eV and an indirect gap of 0.14 eV along the Γ–X direction. The proximity of the Fermi level to the valence band maximum further suggests a hole-dominant transport behavior in lithiated T_d' phase, which confirms the finding of electron to hole transport transition in our in situ magneto-transport measurements.

2.4. Mechanism of the Phase Transition

The crystal structure of the lithiated T_d' phase was recently discovered using single crystal X-ray crystallography by Muscher et al., characterized by a subgroup of four distinct in-plane W–W bond distances along crystal *a* axis, as shown in Figure S14 (Supporting Information).[13] Remarkably, a crystal structure with the same in-plane W–W chain distortion was theoretically predicted to be a 2×2 CDW in monolayer WTe_2

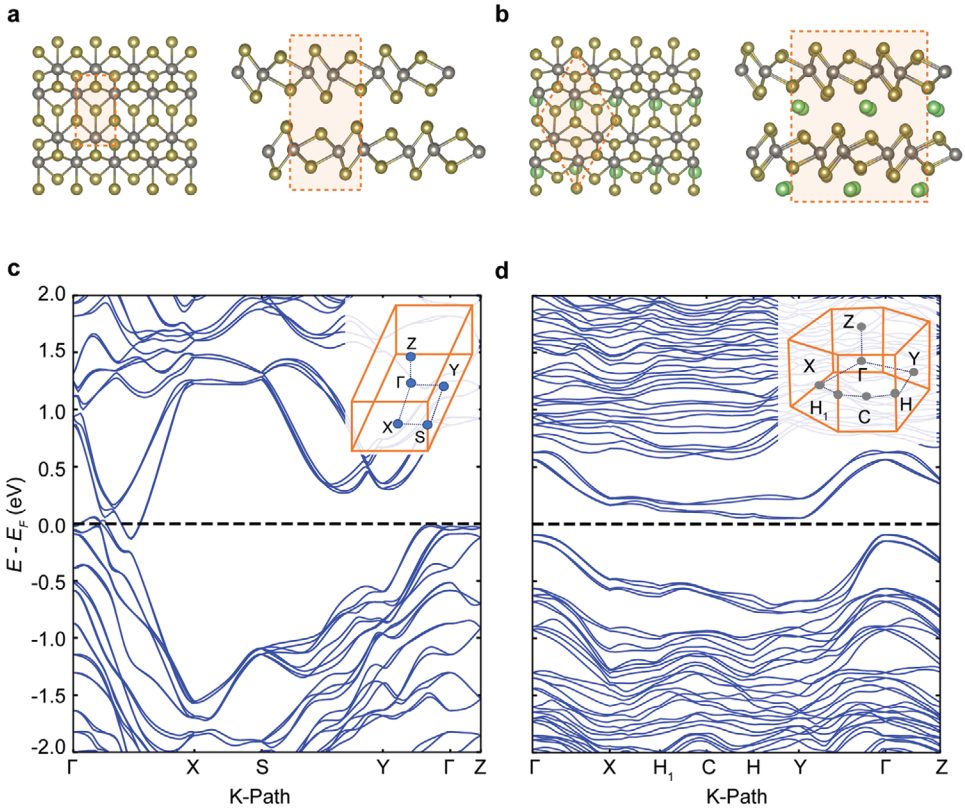

Figure 5. a,b) In-plane and cross-sectional atomic structures of T_d-WTe_2 (a) and lithiated T_d'-$Li_{0.5}WTe_2$ (b) with W atoms in gray, Te atoms in gold, and Li atoms in green. Unit cells are highlighted with orange dashed lines. c,d) DFT electronic band structures of T_d-WTe_2 (c) and lithiated T_d'-$Li_{0.5}WTe_2$ (d) along a high-symmetry K-path in Brillouin zone, as shown in the insets,[21] reveal their semimetallic and semiconducting nature, respectively. The horizontal black dashed lines in (c) and (d) mark the Fermi level for each phase.

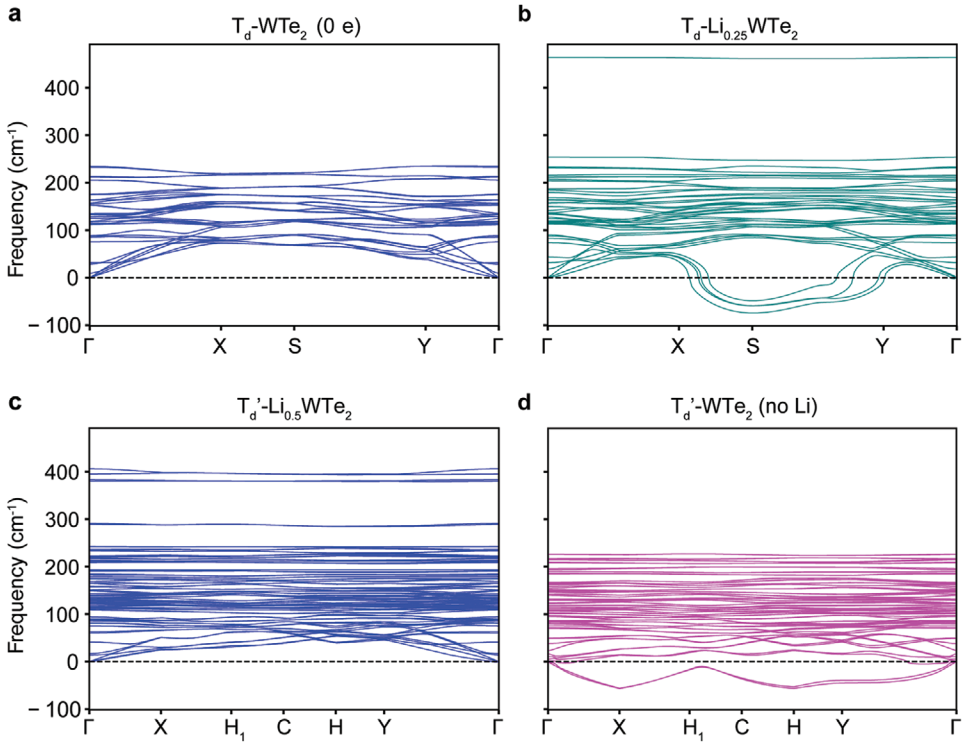

Figure 6. a–d) Phonon-dispersion of T_d-WTe_2 (a), lithiated T_d-$Li_{0.25}WTe_2$ (b), the lithiated T_d'-$Li_{0.5}WTe_2$ phase (c), and T_d'-WTe_2 without any Li atoms (d).

under electron doping at a level of 0.5 electrons per unit cell (9.04×10^{13} e cm^{-2}).[11,12] This strongly suggests that the new phase we observe coincides with the predicted 2×2 CDW and that the CDW formation is driven by the extremely high levels of electron doping from Li intercalants.

To confirm the nature of the new phase in bulk and explore the mechanism driving the phase transition, we computed the phonon dispersion of the lithiated T_d phase in bulk as shown in **Figure 6**. Our Bader charge[18] analysis suggests that each Li atom dopes ≈0.85 e to the Te atoms. Accordingly, we computed the phonon dispersion of the lithiated T_d phase for two concentrations of electronic doping: 1 Li atom/unit cell (T_d-$Li_{0.25}WTe_2$) in Figure 6b and implicit doping at a concentration equivalent to the level of doping by Li in the lithiated T_d' phase (T_d-$Li_{0.5}WTe_2$) in Figure S15 (Supporting Information). The phonon dispersion of the pristine T_d phase in Figure 6a shows a stable structure. Upon introduction of 1 Li atom per unit cell, the phonon branch along the X-S-Y path in the Brillouin zone becomes soft, suggesting the instability of the lattice and the possible formation of a CDW, similar to the picture of the CDW phase diagram predicted in monolayer WTe_2.[11] A similar softening is also observed in the case of the implicitly doped T_d in Figure S15 (Supporting Information), indicating that high level of electron doping alone leads to lattice instability. On the contrary, the lithiated T_d' phase (T_d'-$Li_{0.5}WTe_2$) shows a stable phonon dispersion in Figure 6c while the removal of Li atoms in the T_d' phase softens the phonon modes along the X–H_1–C–H–Y path in Figure 6d. Energetically, the phase transition from T_d to the T_d' is driven by the greater negative formation energy of T_d' phase than the lithiated T_d-WTe_2 at the same Li concentration. Based on our DFT calculations, the change in enthalpy in going from T_d-WTe_2 to lithiated T_d'-$Li_{0.5}WTe_2$ is –0.62 eV, whereas it is –0.36 eV going from T_d to lithiated T_d-$Li_{0.5}WTe_2$.

3. Conclusion

A new gapped phase is discovered in semimetallic T_d-WTe_2, stabilized by an exceptionally high level of electron doping from lithium intercalation. We identified the structure of the new phase to be a lithiated T_d' phase by in situ angle-resolved Raman spectroscopy. A bandgap opening in the new phase is suggested by in situ transport measurements that show an increasing resistance with decreasing temperature and a much-reduced carrier density. Our DFT calculations show that this new lithiated T_d' phase has an indirect gap of 0.14 eV and a direct bandgap of 0.66 eV. Furthermore, the structure of the lithiated T_d' phase is identical to the unit cell of the predicted 2×2 CDW in WTe_2 monolayer by electron doping,[11] and phonon dispersion calculations show that lithiation induces phonon softening in the T_d phase at various electron doping levels. Therefore, we identify this new lithiated T_d' phase to be a potential 2×2 CDW in WTe_2. A careful crystallographic study of a single WTe_2 device via in situ diffraction is necessary to directly verify the nature of CDW.

It is notable that the new lithiated T_d' phase lands at the high electron doping end in the electronic phase diagram of WTe_2, past the superconducting phase of WTe_2.[12] So far, superconductivity in WTe_2 has been observed in monolayers by gating[7] or in the bulk by pressure.[19] Since electron doping in bulk WTe_2 requires chemical doping rather than electrical field gating, lithium intercalation can be used to dope "bulk-like"

WTe_2 flakes to potentially induce superconductivity as lithium intercalants present in every van der Waals gap can dope every WTe_2 layer.

Lastly, we envision that the exceptional electron doping using lithium intercalation can also introduce CDW in other 2D transition metal dichalcogenide systems that are not known to host CDW in their intrinsic state, such as 1T′-$MoTe_2$. Thus, the greatly expanded electronic and structural phase diagram of 2D materials accessible using lithium intercalation will stimulate the research for novel quantum phases, such as topological superconductivity. Additionally, the sharp switch of electrical resistance of layered WTe_2 by controllable tuning of electrochemical intercalation voltage projects prospective applications in resistive memory.

4. Experimental Section

Device Fabrication: The WTe_2 flakes were mechanically exfoliated from bulk WTe_2 crystals purchased from 2D Semiconductors. WTe_2 flakes with desired lateral size and thickness were wet transferred onto SiO_2/Si wafer with the assistance of KOH.[22] The thickness of the flake was determined by a Cypher ES atomic force microscope from Asylum Research. For the device fabrication, electrodes were written by electron beam lithography (Nabity NPGS, Helios G4 FIB-SEM) at a voltage of 30 kV and a current of 1.6 nA with a dose of 410 μC cm^{-2}. The developed devices were deposited with 15 nm Cr and 200 nm Au using a thermal evaporator (MBraun EcoVap) at a pressure of 10^{-7} mbar. The devices were transferred into an argon glovebox with an O_2 and H_2O level below 1 ppm right after the liftoff to minimize the oxidation.

Electrochemical Intercalation Cell Fabrication: All the intercalation cells discussed in the main text adopted a planar cell configuration with both the WTe_2 electrode and lithium electrode on a piece of transparent glass slide or SiO_2/Si wafer. The detailed fabrication steps are described in our previous research papers.[22,23] For the liquid cells, the liquid electrolyte of 1 M $LiPF_6$ (EC/DEC, v:v = 50:50, battery-grade, Sigma-Aldrich) was injected into the cell to submerge the lithium and the device. For polymer cells, 0.227 g 1 M $LiPF_6$ solution was premixed with 0.475 g poly(ethylene glycol) methyl ether methacrylate (PEGMA) and 1.145 g bisphenol A ethoxylate dimethacrylate (BEMA) in a tarnished glass vial stirred overnight inside the glovebox. Then, 46 mg of photoinitiator, 2-hydroxy-2-methyl-1-phenyl-1-propanone, was added to the well-mixed electrolyte and stirred for an additional hour in dark prior to the actual use. The mixed polymer electrolyte was drop-cast onto the target device using a micropipette covering both Li/copper foil and the WTe_2 device, then cured under UV light for 10 min to form a gel-like electrolyte. For the low-temperature transport measurements down to 2 K, a solution of 0.3 g of PEO and 0.05 g of LiTFSI in 3.7 ml of anhydrous acetonitrile was used for lithium intercalation. The PEO–LiTFSI mixture solution was drop-cast onto the device and then dried in vacuum for 1 hour before in situ measurements. The assembled intercalation cells have a cover slip with an air-tight seal that protects the cell from air and moisture.

In Situ Raman Characterization: The assembled cell was taken out from the glovebox and quickly mounted to the Raman sample stage within 10 min. Intercalation of lithium ions was driven by applying voltage between the Li and WTe_2 electrode potentiostatically with a Biological SP300 potentiostat/galvanostat. In situ Raman spectra were collected during lithium intercalation using a Horiba LabRAM HR Evolution Spectrometer (grating: 1800 lines mm^{-1}) with an excitation wavelength of 633 nm at 10% power (3.5 mW).

In Situ Low-Frequency Raman and Angle-Resolved Raman Measurements: The low-frequency and angle-dependent Raman spectra were acquired using a frequency-stabilized 785 nm laser (Toptica) as the excitation source with an incident power adjusted to 5.6 mW by a neutral-density filter. A set of five narrow-linewidth, reflective volume Bragg grating notch filters (OptiGrate) was used to reject the laser and allow for measurements of Raman signals down to about 5 cm^{-1}. The polarization of the incident beam was controlled by a zero-order half-waveplate, and the polarization of scattered Raman signal was first set by a broadband linear polarizer, and then rotated by a broadband half waveplate to maintain a fixed polarization of the Raman light sent into the spectrometer. The Raman signal was spatially filtered by a pair of 75 mm focal-length achromatic lens and a 50 μm pinhole, before sent into the spectrograph (Andor Kymera 328i) and captured by a Si EMCCD (Andor iXon Life 888). A superlong-working distance objective lens (10×, numerical aperture (NA) = 0.28) was used in the measurements.

In Situ Two-Terminal Electrical Transport Measurements: In situ two-terminal electrical transport data were collected using a semiconductor device analyzer (Agilent Technologies B1500A) during the potentiostatic lithium intercalation. The drain–source voltage applied was 50 mV, and the resistance was extracted from the slope of the *I*–*V* curve using a linear regression method.

Low-Temperature Magneto-transport Measurements: Magneto-transport measurements of pristine T_d-WTe_2 at 2 K were carried out with Quantum Design's DynaCool PPMS system at AC mode (17.777 Hz). The system was first cooled to 2 K at 0 T with a cooling rate of 5 K min^{-1}. Then the magneto-transport measurement of the pristine state was carried out with magnetic field sweeping between −14 to 14 T at a sweeping rate of 100 Oe s^{-1}. A two-channel fitting model ($\rho_{xy} = \frac{(n_h\mu_h^2 - n_e\mu_e^2)B + \mu_h^2\mu_e^2(n_h - n_e)B^3}{e[(n_h\mu_h + n_e\mu_e)^2 + (n_h - n_e)^2\mu_h^2\mu_e^2B^2]}$; $\rho_{xx} = \frac{(n_h\mu_h + n_e\mu_e) + (n_h\mu_h\mu_e^2 + n_e\mu_e\mu_h^2)B^2}{e[(n_h\mu_h + n_e\mu_e)^2 + (n_h - n_e)^2\mu_h^2\mu_e^2B^2]}$) was applied to fit the magnetic field dependent R_{xx} and R_{xy} to extract the mobility (μ) and carrier density (n) of electrons (e) and holes (h).[17]

In Situ Magneto-Transport Measurements: In situ Hall transport measurements were carried out using the DynaCool PPMS system. After the assembly of the polymer cell and wire bonding between the gold pads of the PPMS puck and the copper foil of the polymer cell, the puck was quickly transferred into the chamber of the PPMS system. Intercalation was carried out at 300 K and 3 T, and R_{xx} and R_{xy} were recorded during the intercalation. The carrier density was determined by equations $n_H = B/(eR_{xy})$, $e = 1.602 \times 10^{-19}$ C.[24] The correction of R_{xy} is obtained by subtracting the contribution of R_{xx} from raw R_{xy} using the equation $R_{xy,\text{corrected, 3T}} = R_{xy,\text{raw, 3T}} - \alpha \cdot R_{xx,3T}$, where α is a geometric factor determined by the ratio of raw R_{xy} over R_{xx} at zero field using $\alpha = R_{xy,0T}/R_{xx,0T}$. Temperature-dependent resistance measurements were carried out by first freezing the electrochemical intercalation through a rapid cooling to 200 K at a rate of 10 K min^{-1}, at which point the intercalation current running through the cell gradually goes to zero. Then the system was gradually cooled to 150 K at a rate of 2 K min^{-1}.

Post-Mortem Characterizations: Intercalation devices were disassembled by physically removing the liquid or polymer electrolyte by a razor blade. Then the device was immersed in isopropanol to further remove the residual electrolyte. The cleaned device was characterized by Raman spectroscopy (Horiba LabRAM HR Evolution Spectrometer; 633 nm) and SEM (Helios G4 FIB-SEM) with a stage tilting angle of 50° at a voltage of 5 kV and a current of 25 pA. XPS of deintercalated device and exfoliated flake was performed on a PHI VersaProbe II Scanning XPS Microprobe with an Al K_α monochromatic X-ray source. A beam spot with the diameter of 20 μm was used to obtain XPS data only from the device, assisted by scanning X-ray induced secondary electron imaging. All of the XPS spectra were calibrated using a carbon 1s peak located at 284.50 eV.

Ab Initio Calculations: Density functional theory (DFT) calculations were carried out in a plane-wave basis set within the projector augmented wave (PAW) approach[25] as implemented in the Quantum Espresso software package.[26] The exchange-correlation was treated at the generalized gradient approximation (GGA) level of Perdew, Burke, and Ernzehof (PBE).[27] The van der Waals interactions were accounted for using Grimme's D3 correction with Becke–Johnson damping.[28] A kinetic energy cut-off of 1040 eV was used for the expansion of the plane-wave basis in all the calculations, and the Brillouin zone was sampled using Gamma-centered Monkhorst–Pack[29] k-point meshes of $32 \times 18 \times 8$

and 16 × 18 × 8 for the T_d (12 atoms) and T_d' (24 atoms) unit cells respectively. The unit cells were relaxed until the total energy and the force on each atom converged to within 0.02 meV atom^{-1} and 0.03 eV Å^{-1}, respectively. The lithiated T_d phase was relaxed with the volume fixed to that of the pristine T_d phase to prevent a doping-induced phase transition. Spin–orbit coupling with noncolinear magnetization was used for all the band structure calculations. Phonopy[30] was used for the calculation of phonon bands, with supercell sizes of 2 × 2 × 2 and 2 × 2 × 1 for T_d- and T_d'- WTe_2 phases, and *q*-meshes of 8 × 4 × 2 and 4 × 4 × 4 were used respectively. For implicitly doped T_d, a 2 × 2 × 1 supercell with a *q*-mesh of 4×4×4 was used.

Supporting Information

Supporting Information is available from the Wiley Online Library or from the author.

Acknowledgements

The authors gratefully acknowledge discussions with Dr. Evan Reed, Dr. Aaron Lindenberg, Dr. Jun-Ho Lee, and Dr. Young-Woo Son. M.W. and J.J.C. gratefully acknowledge the support from the Moore Foundation under the EPiQS Synthesis Investigator Award program. The electrochemical cell was developed with the support from the NSF CAREER 1749742. J.M.W. acknowledges the support from the NASA graduate student fellowship (80NSSC17K0146) and D.J.H. acknowledges the support from the NASA graduate student fellowship (80NSSC19K1331). J.V.P. was supported by the National Defense Science and Engineering Graduate (NDSEG) Fellowship Program, sponsored by the Air Force Research Laboratory (AFRL), the Office of Naval Research (ONR), and the Army Research Office (ARO). D.Y.Q. and A.K. were supported by the U.S. Department of Energy (DOE), Office of Science, Office of Basic Energy Sciences Early Career Research Program under Award Number DE-SC0021965. The calculations used resources of the National Energy Research Scientific Computing (NERSC), a DOE Office of Science User Facility operated under contract no. DE-AC02-05CH11231; the Extreme Science and Engineering Discovery Environment (XSEDE), which is supported by National Science Foundation grant number ACI-1548562; and the Oak Ridge Leadership Computing Facility at the Oak Ridge National Laboratory, which is supported by the Office of Science of the U.S. DOE under Contract No. DE-AC05-00OR22725. The authors also thank the Yale Center for Research Computing for the calculations carried out on the Grace supercomputer.

Conflict of Interest

The authors declare no conflict of interest.

Data Availability Statement

The data that support the findings of this study are available from the corresponding author upon reasonable request.

Keywords

charge density waves, electron doping, lithium intercalation, phase transitions, tungsten ditelluride

Received: January 26, 2022
Revised: April 20, 2022
Published online: May 12, 2022

[1] a) S. Wu, V. Fatemi, Q. D. Gibson, K. Watanabe, T. Taniguchi, R. J. Cava, P. Jarillo-Herrero, *Science* **2018**, *359*, 76; b) S. Tang, C. Zhang, D. Wong, Z. Pedramrazi, H.-Z. Tsai, C. Jia, B. Moritz, M. Claassen, H. Ryu, S. Kahn, *Nat. Phys.* **2017**, *13*, 683.
[2] Z. Fei, W. Zhao, T. A. Palomaki, B. Sun, M. K. Miller, Z. Zhao, J. Yan, X. Xu, D. H. Cobden, *Nature* **2018**, *560*, 336.
[3] a) B. Sun, W. Zhao, T. Palomaki, Z. Fei, E. Runburg, P. Malinowski, X. Huang, J. Cenker, Y.-T. Cui, J.-H. Chu, *Nat. Phys.* **2022**, *18*, 94; b) Y. Jia, P. Wang, C.-L. Chiu, Z. Song, G. Yu, B. Jäck, S. Lei, S. Klemenz, F. A. Cevallos, M. Onyszczak, *Nat. Phys.* **2022**, *18*, 94.
[4] B. Zhao, B. Karpiak, D. Khokhriakov, A. Johansson, A. M. Hoque, X. Xu, Y. Jiang, I. Mertig, S. P. Dash, *Adv. Mater.* **2020**, *32*, 2000818.
[5] D. MacNeill, G. Stiehl, M. Guimaraes, R. Buhrman, J. Park, D. Ralph, *Nat. Phys.* **2017**, *13*, 300.
[6] V. Fatemi, S. Wu, Y. Cao, L. Bretheau, Q. D. Gibson, K. Watanabe, T. Taniguchi, R. J. Cava, P. Jarillo-Herrero, *Science* **2018**, *362*, 926.
[7] E. Sajadi, T. Palomaki, Z. Fei, W. Zhao, P. Bement, C. Olsen, S. Luescher, X. Xu, J. A. Folk, D. H. Cobden, *Science* **2018**, *362*, 922.
[8] a) S. Tang, C. Zhang, D. Wong, Z. Pedramrazi, H.-Z. Tsai, C. Jia, B. Moritz, M. Claassen, H. Ryu, S. Kahn, J. Jiang, H. Yan, M. Hashimoto, D. Lu, R. G. Moore, C.-C. Hwang, C. Hwang, Z. Hussain, Y. Chen, M. M. Ugeda, Z. Liu, X. Xie, T. P. Devereaux, M. F. Crommie, S.-K. Mo, Z.-X. Shen, *Nat. Phys.* **2017**, *13*, 683; b) M. Ono, T. Noji, M. Harada, K. Sato, T. Kawamata, M. Kato, *J. Phys. Soc. Jpn.* **2020**, *90*, 014706.
[9] L. Zhu, Q.-Y. Li, Y.-Y. Lv, S. Li, X.-Y. Zhu, Z.-Y. Jia, Y. B. Chen, J. Wen, S.-C. Li, *Nano Lett.* **2018**, *18*, 6585.
[10] a) A. K. Nayak, A. Steinbok, Y. Roet, J. Koo, G. Margalit, I. Feldman, A. Almoalem, A. Kanigel, G. A. Fiete, B. Yan, Y. Oreg, N. Avraham, H. Beidenkopf, *Nat. Phys.* **2021**, *17*, 1413; b) B. Sipos, A. F. Kusmartseva, A. Akrap, H. Berger, L. Forró, E. Tutiš, *Nat. Mater.* **2008**, *7*, 960; c) Y. Yu, F. Yang, X. F. Lu, Y. J. Yan, Y.-H. Cho, L. Ma, X. Niu, S. Kim, Y.-W. Son, D. Feng, S. Li, S.-W. Cheong, X. H. Chen, Y. Zhang, *Nat. Nanotechnol.* **2015**, *10*, 270; d) J. T. Ye, Y. J. Zhang, R. Akashi, M. S. Bahramy, R. Arita, Y. Iwasa, *Science* **2012**, *338*, 1193.
[11] J.-H. Lee, Y.-W. Son, *Phys. Chem. Chem. Phys.* **2021**, *23*, 17279.
[12] W. Yang, C.-J. Mo, S.-B. Fu, Y. Yang, F.-W. Zheng, X.-H. Wang, Y.-A. Liu, N. Hao, P. Zhang, *Phys. Rev. Lett.* **2020**, *125*, 237006.
[13] P. K. Muscher, D. A. Rehn, A. Sood, K. Lim, D. Luo, X. Shen, M. Zajac, F. Lu, A. Mehta, Y. Li, X. Wang, E. J. Reed, W. C. Chueh, A. M. Lindenberg, *Adv. Mater.* **2021**, *33*, 2101875.
[14] M. Kim, S. Han, J. H. Kim, J.-U. Lee, Z. Lee, H. Cheong, *2D Mater.* **2016**, *3*, 034004.
[15] G. Eda, H. Yamaguchi, D. Voiry, T. Fujita, M. Chen, M. Chhowalla, *Nano Lett.* **2011**, *11*, 5111.
[16] M. N. Ali, J. Xiong, S. Flynn, J. Tao, Q. D. Gibson, L. M. Schoop, T. Liang, N. Haldolaarachchige, M. Hirschberger, N. P. Ong, R. J. Cava, *Nature* **2014**, *514*, 205.
[17] J. M. Woods, J. Shen, P. Kumaravadivel, Y. Pang, Y. Xie, G. A. Pan, M. Li, E. I. Altman, L. Lu, J. J. Cha, *ACS Appl. Mater. Interfaces* **2017**, *9*, 23175.
[18] W. Tang, E. Sanville, G. Henkelman, *J. Phys.: Condens. Matter* **2009**, *21*, 084204.
[19] D. Kang, Y. Zhou, W. Yi, C. Yang, J. Guo, Y. Shi, S. Zhang, Z. Wang, C. Zhang, S. Jiang, *Nat. Commun.* **2015**, *6*, 7804.
[20] M. Wang, S. Xu, J. J. Cha, *Adv. Energy Sustainability Res.* **2021**, *2*, 2100027.
[21] M. J. Mehl, D. Hicks, C. Toher, O. Levy, R. M. Hanson, G. Hart, S. Curtarolo, *Comput. Mater. Sci.* **2017**, *136*, S1.
[22] S. Yazdani, J. V. Pondick, A. Kumar, M. Yarali, J. M. Woods, D. J. Hynek, D. Y. Qiu, J. J. Cha, *ACS Appl. Mater. Interfaces* **2021**, *13*, 10603.

[23] J. V. Pondick, A. Kumar, M. Wang, S. Yazdani, J. M. Woods, D. Y. Qiu, J. J. Cha, *ACS Appl. Nano Mater.* **2021**, *4*, 14105.
[24] D. K. Bediako, M. Rezaee, H. Yoo, D. T. Larson, S. Y. F. Zhao, T. Taniguchi, K. Watanabe, T. L. Brower-Thomas, E. Kaxiras, P. Kim, *Nature* **2018**, *558*, 425.
[25] a) P. E. Blöchl, *Phys. Rev. B* **1994**, *50*, 17953; b) A. Dal Corso, *Comput. Mater. Sci.* **2014**, *95*, 337.
[26] P. Giannozzi, S. Baroni, N. Bonini, M. Calandra, R. Car, C. Cavazzoni, D. Ceresoli, G. L. Chiarotti, M. Cococcioni, I. Dabo, *J. Phys.: Condens. Matter* **2009**, *21*, 395502.
[27] J. P. Perdew, K. Burke, M. Ernzerhof, *Phys. Rev. Lett.* **1996**, *77*, 3865.
[28] A. D. Becke, E. R. Johnson, *J. Chem. Phys.* **2005**, *123*, 154101.
[29] H. J. Monkhorst, J. D. Pack, *Phys. Rev. B* **1976**, *13*, 5188.
[30] A. Togo, I. Tanaka, *Scr. Mater.* **2015**, *108*, 1.

ADVANCED MATERIALS
www.advmat.de

Tunable Strong Coupling in Transition Metal Dichalcogenide Nanowires

Jingang Li, Kan Yao, Yun Huang, Jie Fang, Pavana Siddhartha Kollipara, Donglei Emma Fan, and Yuebing Zheng**

Subwavelength optical resonators with spatiotemporal control of light are essential to the miniaturization of optical devices. In this work, chemically synthesized transition metal dichalcogenide (TMDC) nanowires are exploited as a new type of dielectric nanoresonators to simultaneously support pronounced excitonic and Mie resonances. Strong light–matter couplings and tunable exciton polaritons in individual nanowires are demonstrated. In addition, the excitonic responses can be reversibly modulated with excellent reproducibility, offering the potential for developing tunable optical nanodevices. Being in the mobile colloidal state with highly tunable optical properties, the TMDC nanoresonators will find promising applications in integrated active optical devices, including all-optical switches and sensors.

1. Introduction

Transition metal dichalcogenides (TMDCs) are an emerging class of materials with extraordinary physical properties,[1] including excitonic effects,[2] tunable bandgaps,[3] and valley polarization.[4] In particular, TMDC monolayers have attracted significant research attention due to their direct bandgaps at the visible and near-infrared wavelengths.[5,6] These properties make TMDCs attractive for a wide range of electronic, photonic, and optoelectronic applications,[7,8] such as transistors,[9,10] photodetection,[11,12] light-emission,[13] and lasing.[14] In addition, strong light-matter interactions between TMDCs and optical cavities, resonant plasmonic or dielectric structures have been demonstrated,[15–18] resulting in the formation of exciton polaritons with rich physics for quantum optics and polaritonic devices.[19,20]

While TMDCs have been extensively explored as an excitonic platform with novel optical and electronic functionalities, it is less appreciated that TMDCs also have a high refractive index.[21] Compared to the widely investigated plasmonic systems, high-index dielectric materials show low loss at visible frequencies, pronounced electric and magnetic optical resonances, and high compatibility with complementary metal-oxide-semiconductor fabrication.[22,23] Dielectric metamaterials based on silicon have rapidly emerged as a popular platform for a wealth of applications in integrated electronics and photonics.[24] Recently, multilayer TMDC nanostructures have been studied as high-index nanoresonators with strong Mie resonances.[25,26] The presence of excitons in TMDCs further enables the formation of unique self-hybridized exciton polaritons,[26,27] which remarkably enrich the capabilities of nanophotonic systems. Additionally, nanostructured TMDC photonic crystals and gratings have been demonstrated with enhanced control of light for advanced photonic applications.[28,29]

Here, we report strong coupling between excitons and Mie resonances in individual TMDC nanowires. Molybdenum disulfide (MoS_2) nanowires are chemically synthesized with tailorable dimensions to support tunable Mie-exciton polaritons in visible wavelengths. Compared to previously reported TMDC nanoresonators that are fabricated by lithographical methods (e.g., electron beam lithography),[25,26] colloidal MoS_2 nanowires provide additional possibilities in the design and fabrication of nanophotonic devices. Specifically, the chemical synthesis approach permits the scalable and high-throughput production of TMDC nanoresonators with tunable dimensions, which can be easily integrated with other techniques for on-demand dispersion, transfer, manipulation, and assembly. Moreover, we show that the MoS_2 excitonic properties and spectral splittings can be optothermally modulated under laser illumination, which offers a promising platform for the development of tunable photonic systems.

2. Results and Discussion

MoS_2 nanowires were synthesized from MoO_3 nanowire precursors via a two-step sulfurization process (see Experimental Section).[30] The first sulfurization reaction at 500 °C converted MoO_3 nanowires to more thermally stable MoS_2/MoO_2 hybrid nanowires, after which a second sulfurization process was carried out at 900 °C to produce pure MoS_2 nanowires (**Figure 1**a; Note S1, Supporting Information). Scanning electron microscopy (SEM), high-resolution transmission electron microscopy (TEM), and selected-area electron diffraction (SAED) were used for materials characterization. The synthesized MoS_2 nanowires have a typical length of 5–20 μm (Figure 1b,c). The symmetrical hexagonal diffraction patterns indicated a hexagonal

J. Li, K. Yao, Y. Huang, J. Fang, P. S. Kollipara, D. E. Fan, Y. Zheng
Walker Department of Mechanical Engineering
Materials Science & Engineering Program and Texas Materials Institute
University of Texas at Austin
Austin, TX 78712, USA
E-mail: dfan@austin.utexas.edu; zheng@austin.utexas.edu
The ORCID identification number(s) for the author(s) of this article can be found under https://doi.org/10.1002/adma.202200656.

DOI: 10.1002/adma.202200656

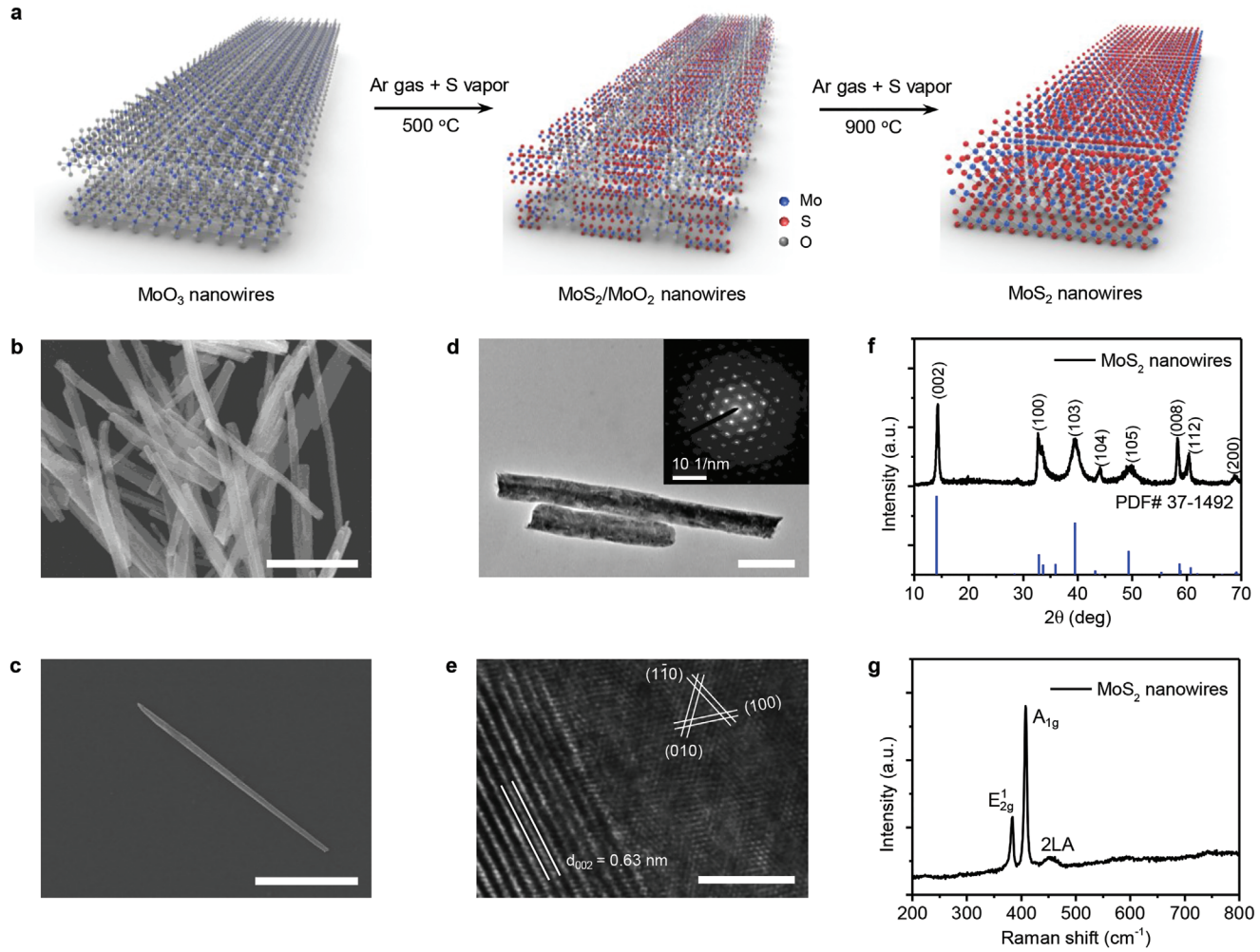

Figure 1. Colloidal MoS_2 nanowires. a) Schematic showing the synthesis of MoS_2 nanowires from MoO_3 nanowire precursors. b,c) SEM images of the as-synthesized MoS_2 nanowires. d,e) Phase-contrast TEM images of MoS_2 nanowires. The inset in (d) shows the SAED pattern. f,g) The corresponding XRD (f) and Raman spectra (g) of MoS_2 nanowires. Scale bars: b) 3 µm, c) 5 µm, d) 500 nm, e) 5 nm.

lattice structure (Figure 1d), and the sharp atomic images also showed a high crystalline quality (Figure 1e). In addition, the corresponding X-ray diffraction (XRD) and Raman spectra further confirmed the crystal structure and chemical purity of MoS_2 nanowires (Figure 1f,g). It should be noted that MoO_3 nanowires serve as both the precursor and the fabrication template, which enables the synthesis of MoS_2 nanowires with controllable dimensions by simply tuning the dimensions of MoO_3 nanowires. In this study, the thickness of MoS_2 nanowires is controlled at ≈65 nm (Figure S1, Supporting Information), while the width is varied to modulate the optical responses.

The optical responses of MoS_2 nanowires are illustrated in **Figure 2**a–c. In addition to intrinsic exciton resonances (Figure 2b), the high refractive index of MoS_2 gives rise to pronounced Mie resonances (Figure 2a). The strong coupling between exciton and Mie resonances leads to the peak splitting in the scattering spectra (Figure 2c). Leaky/guided modes are also allowed in dielectric nanowires, which nonetheless cannot be excited efficiently with plane waves unless using near grazing incidence.[31] We measured optical scattering from individual MoS_2 nanowires with a varying width using dark-field spectroscopy (see the Experimental Section) and correlated the spectra with the morphologies of nanowires via SEM imaging (Figure 2f). Figure 2d,e shows the experimental dark-field scattering spectra and the corresponding full-wave simulations for three MoS_2 nanowires with a thickness of 65 nm and a width of 100, 160, and 200 nm (see the Experimental Section). Considering the anisotropic morphology of nanowires, we studied the scattering responses under both transverse-electric (TE, Figure 2d) and transverse-magnetic (TM, Figure 2e) illumination, where the incident light was linearly polarized with the electric field either perpendicular (TE) or parallel (TM) to the nanowire axis.

The experimental and simulated spectra of MoS_2 nanowires are in good agreement for both polarizations. The most notable features of all scattering spectra are two dips at ≈665 and ≈612 nm, corresponding to the A and B excitons of MoS_2, respectively. The dips arise from the coupling between the excitons and Mie resonance, which leads to the formation of three Mie-exciton hybrid modes. Strong coupling is evidenced by dips at the same wavelengths in the absorption spectra (Figure S2, Supporting Information).[32] We also confirmed

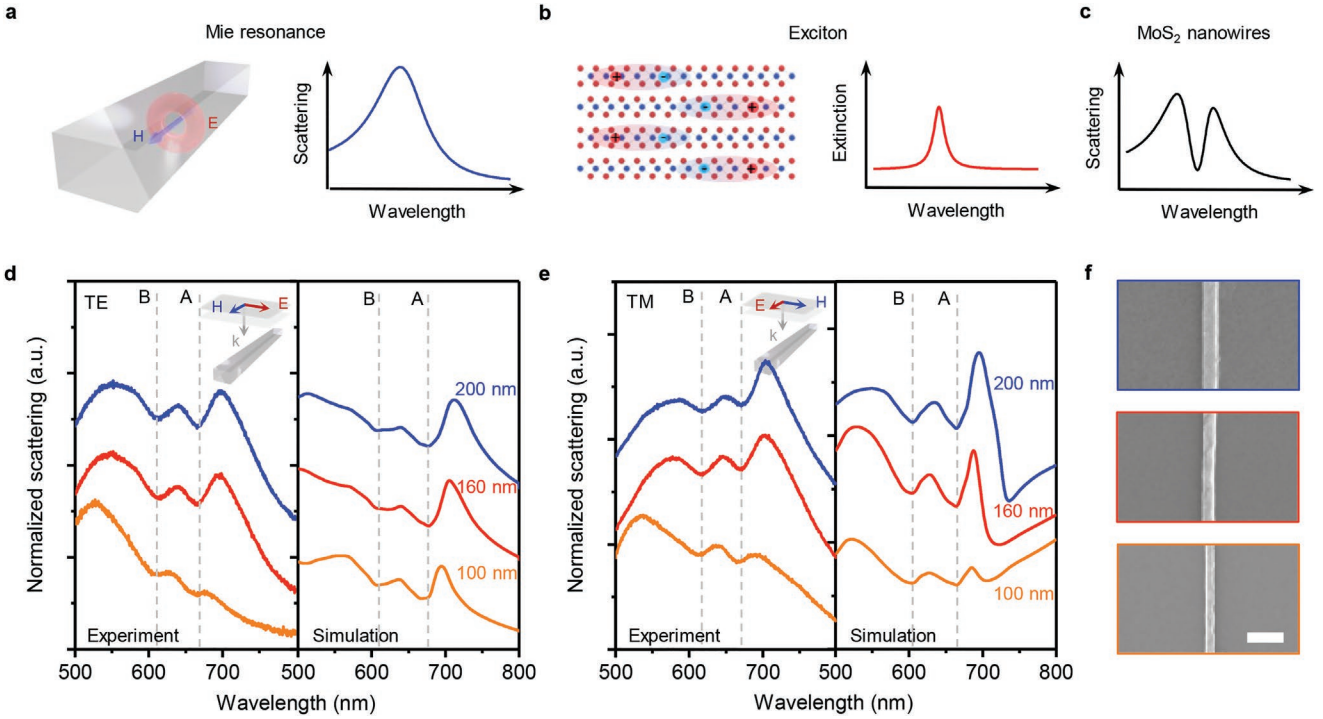

Figure 2. Optical scattering response of individual MoS_2 nanowires. a–c) Schematic illustration showing the optical properties and scattering responses of TMDC nanowires: a) Mie resonance, b) exciton resonance, and c) total scattering with the coupling between exciton and Mie resonances. d,e) Optical scattering spectra of MoS_2 nanowires with a width of 100, 160, and 200 nm under TE-polarized (d) and TM-polarized (e) plane wave excitation (the insets show the schematics of the corresponding experimental geometries). f) Corresponding SEM images of the measured MoS_2 nanowires in (d) and (e). Scale bar: 500 nm.

that the spectral dips still remain at the same positions with the varying thickness of nanowires (Figure S3, Supporting Information). In addition, the whole scattering profile shows a gradual redshift with the increasing width of MoS_2 nanowires, which is consistent with the size-dependent behavior of Mie resonances. The scattering spectra under TE and TM excitation exhibit peaks in similar positions, while the peak at the longer wavelength is stronger under TM polarization. This quantitative difference can be attributed to the two-fold degeneracy of a higher-order mode compared to the nondegenerate TE01 mode (i.e., the magnetic dipole in this case), which can be seen in the Mie formulas for infinite cylinders[31] and is consistent with the previously reported observations.[33]

Figure 3a plots the experimental scattering map for MoS_2 nanowires with a varying width from 100 to 240 nm under TE-polarized excitation. The green dot lines highlight the three polariton branches, and the grey dot lines mark two fixed dips at exciton resonances. The simulated map agrees well with the experimental results (Figure 3b), where all excitonic and polaritonic features are reproduced. Similar results were also obtained under TM-polarized excitation (Figure S4, Supporting Information). Figure 3c shows the field distributions at the wavelength of 640 nm between A and B excitons for TE polarization, where a dominant magnetic dipole resonance is clearly recognized. To gain deeper understanding of the interactions between excitons and Mie resonances, we conducted multipole decomposition by retrieving the multipole moments of the nanowires from simulated field distributions. For an infinite nanowire aligned along the z-axis, the Mie coefficients can be expressed by

$$a_m = -\frac{\eta k}{4}\int \mathbf{J}_z e^{im\varphi} J_m(kr)ds \tag{1}$$

for TM polarization and

$$b_m = \frac{i}{4}\int \frac{e^{im\varphi}}{r}[kr\mathbf{J}_\varphi J_{m+1}(kr) + m(i\mathbf{J}_r - \mathbf{J}_\varphi)J_m(kr)]ds \tag{2}$$

for TE polarization.[34] Here, m takes integers, r and φ are the polar coordinates, η is the wave impedance of the host medium, k is the wave number, $J_m(\cdot)$ is the Bessel function of the first kind and order m, $\mathbf{J} = -i\omega\varepsilon_0(\varepsilon - \varepsilon_h)\mathbf{E}$ is the current induced by the total electric field $\mathbf{E}$ with ε and ε_h the relative permittivities of the nanowire and host medium, respectively. The scattering cross section of the nanowire C_s can be calculated from these coefficients by

$$C_s = \frac{4}{kE_0^2}\sum_{m=-\infty}^{m=\infty}(|a_m|^2 + \eta^2|b_m|^2) \tag{3}$$

where E_0 is the amplitude of the electric field of the incident plane wave. Figure 3d shows the simulated scattering cross section of a nanowire for TE polarization, along with the contributions from individual Mie resonances. Scattering is dominated by only three terms ($m = 0, \pm 1$), of which the positive and

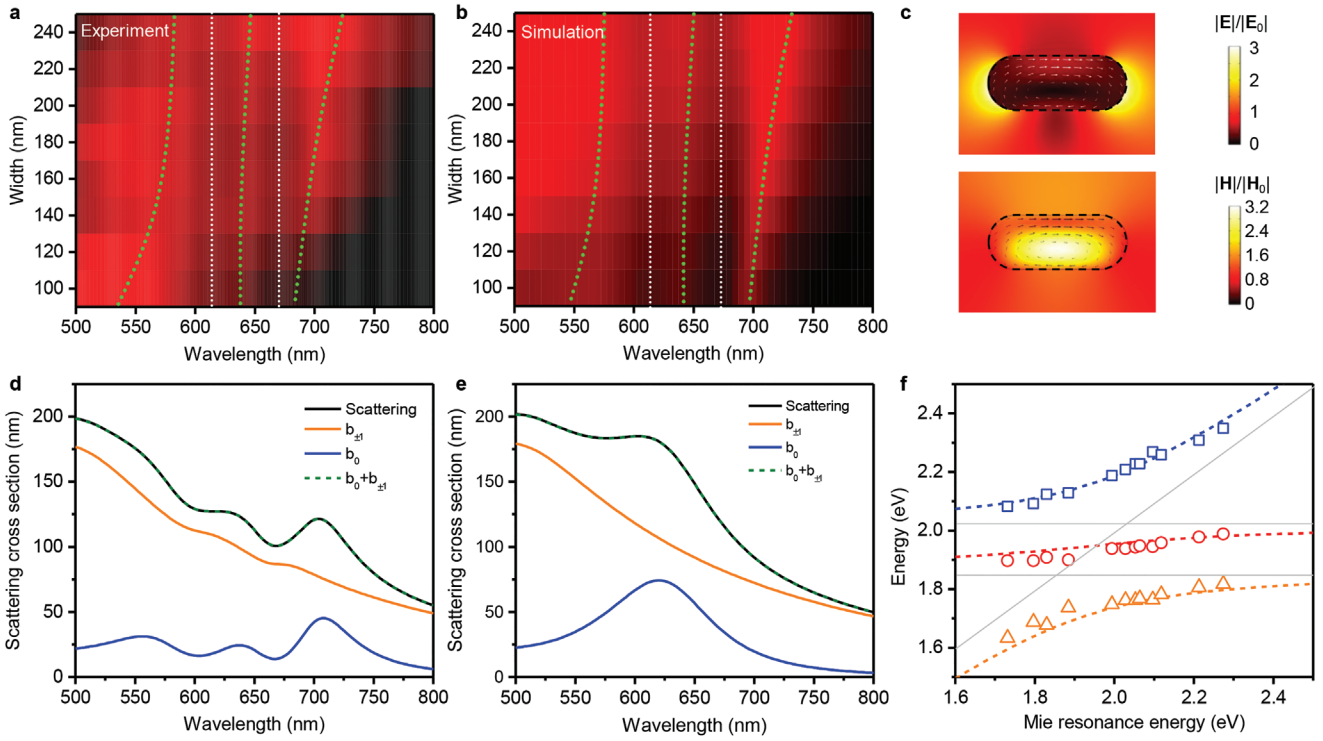

Figure 3. Strong coupling in individual MoS_2 nanowires under TE-polarized excitation. a) Experimental normalized dark-field scattering map for MoS_2 nanowires with a thickness of 65 nm and a varying width from 100 to 240 nm. b) The corresponding simulated scattering map of (a). The green dot lines depict three polariton branches. The grey dot lines show the positions of A and B excitons. c) Simulated electric and magnetic field intensity in the cross-section of a MoS_2 nanowire with a width of 160 nm at the wavelength of 640 nm, revealing the typical patterns of a magnetic dipole resonance. The arrows denote the electric field vectors inside the nanowire. d) Simulated scattering cross section (black solid curve) of a MoS_2 nanowire with a width of 150 nm in vacuum. Also shown are the contributions to total scattering by decomposed magnetic dipole mode (b_0, blue curve), electric dipole mode ($b_{\pm1}$, orange curve), and their sum (green dashed curve). e) Same as (d), except that the oscillator strengths of A and B excitons are set to 0 in the dielectric function. f) Anticrossing behaviors of three polariton branches. Colored dots represent experimental polariton eigen energies as a function of Mie resonance energy; colored dashed lines depict the eigen energies obtained from Hamiltonian analysis; and grey solid lines indicate the exciton (horizontal lines) and Mie (diagonal line) resonances.

negative orders are degenerate due to symmetry. Noticeably, excitons are predominantly coupled to the magnetic dipole resonance (b_0), as can be concluded by comparing the decomposed contributions to the scattering spectrum in Figure 3e, where the A and B excitons are artificially turned off in the dielectric function (see the Experimental Section; Figure S5, Supporting Information). Interestingly, the coupling to electric dipole (a_0) and magnetic dipole ($a_{\pm1}$) resonances is comparable for TM polarization (Figure S6, Supporting Information). We attribute the dominance of coupling to magnetic dipole mode under TE-polarized excitation to the characteristic mode profiles. When the incident field is polarized parallel to the cross-sectional plane, the formation of a magnetic dipole mode requires strong circulating electric fields inside the nanowire (Figure 3c), whereas the interior electric fields of an electric dipole mode are less intense as a consequence of the high refractive index and continuity requirement of the electric displacement. For TM polarization, this difference between electric and magnetic modes is not significant, and the interior electric fields are polarized in the unbounded direction along the nanowire axis. Thus, a more sophisticated model is needed to consider the simultaneous involvement of electric and magnetic modes, which is beyond this work.

The fact that only the magnetic dipole resonance is active in coupling under TE polarization allows us to investigate the coupled system with additional Hamiltonian analysis (see Note S2 in the Supporting Information for more details). The Hamiltonian matrix of the coupled system can be written as[35]

$$\hat{\mathcal{H}} = \hbar \begin{pmatrix} \omega_{MD} - i\frac{\gamma_{MD}}{2} & g_A & g_B \\ g_A & \omega_A - i\frac{\gamma_A}{2} & 0 \\ g_B & 0 & \omega_B - i\frac{\gamma_B}{2} \end{pmatrix} \quad (4)$$

where ω_{MD} (γ_{MD}), ω_A (γ_A), and ω_B (γ_B) are the frequencies (linewidths, i.e., full width at half maximum) of the magnetic dipole resonance, A exciton, and B exciton, respectively; and $g_{A/B}$ represents the coupling strength between A/B exciton and the magnetic dipole resonance. The parameters used to solve the polariton eigenfrequencies are summarized in **Table 1**. Figure 3f shows the anticrossing behaviors of three polariton branches in MoS_2 nanowire at room temperature (also see Figure S7 in the Supporting Information for the experimental spectra). The extracted Rabi splitting between the upper and

Table 1. Parameters used in the Hamilton analysis,.

g_A [meV]	g_B [meV]	γ_A [meV]	γ_B [meV]	γ_{MD} [meV]
160	140	120	160	310

lower polariton branches $\Omega_{UP\text{-}LP}$ is ≈450 meV, which fulfils the criteria of strong coupling $\Omega_{UP\text{-}LP} > \gamma_{MD}$. In addition, the Rabi splittings between the upper and middle polariton ($\Omega_{UP\text{-}MP}$) and middle and lower polariton ($\Omega_{MP\text{-}LP}$) can be extracted at the zero detuning between magnetic dipole mode and B exciton and magnetic dipole mode and A exciton, respectively, as $\Omega_{UP\text{-}MP} \approx$ 243 meV and $\Omega_{MP\text{-}LP} \approx$ 262 meV. Both meet the strong coupling condition as $\Omega_{UP\text{-}MP} > (\gamma_{MD} + \gamma_B)/2$ and $\Omega_{MP\text{-}LP} > (\gamma_{MD} + \gamma_A)$. We further fitted the measured scattering spectra via coupled-mode theory (CMT, see Note S3 in the Supporting Information for more details).[36,37] The CMT fitting results are in good agreement with the experimental spectra (Figure S8, Supporting Information) and the fitting parameters are consistent with the Hamilton analysis (Table S1, Supporting Information). From the CMT fitting results, the coupling strength $g_{A/B}$ fulfills the criteria of strong coupling,[37,38] $g_{A/B} > \sqrt{\left(\gamma_2^{MD} + \gamma_2^{A/B}\right)/8}$, which further confirmed the strong coupling regime. It should be noted that the coupling strength g is proportional to $\sqrt{N}$, where N is the number of excitons in the coupling region.[35] In our case, strong coupling is guaranteed with the effective spectral and spatial overlaps between Mie resonances and the large quantity of excitons in MoS_2 nanowires.

The capability of tuning excitonic properties and scattering responses is appealing for applications in photonic devices. Previously, exciton tuning has been demonstrated in TMDCs through ionic-liquid gating.[39] In this work, due to the high optical absorption of MoS_2 nanowires (Figure S9, Supporting Information),[40] the MoS_2 excitonic properties can be optothermally modulated by light illumination. Under low-power laser irradiation, the exciton dips in the scattering spectra gradually redshifted and became suppressed along with the increasing optical power (**Figure 4**a). The spectral splittings became not observable at a laser power of 1.1 mW. To further understand this tuning behavior, we extracted the temperature-dependent excitonic energy and linewidth from the CMT fitting (Figure S10 and Table S2, Supporting Information). The energy redshift and linewidth broadening can be clearly observed for both A and B excitons (Figure 4b; Figure S11, Supporting Information). The excitonic energy as a function of temperature can be described by the O'Donnell model[41]

$$E_{A/B}(T) = E_{A/B}(0) - S\langle\hbar\omega\rangle\left[\coth\left(\frac{\langle\hbar\omega\rangle}{2k_BT}\right) - 1\right] \quad (5)$$

where $E_{A/B}(T)$ and $E_{A/B}(0)$ are the energy of A/B excitons at the temperature of T and 0 K, respectively, S is a dimensionless coupling constant to phonons, $\langle\hbar\omega\rangle$ is the average phonon energy, and k_B is the Boltzmann constant. The excitonic linewidth broadening can be modeled by[42]

$$\gamma_{A/B}(T) = \gamma_{A/B}(0) - \gamma' T \quad (6)$$

where $\gamma_{A/B}(T)$ and $\gamma_{A/B}(0)$ are the linewidth of A/B excitons at the temperature of T and 0 K, respectively, γ' is the exciton–phonon coupling strength. The extracted temperature-dependent excitonic energy and linewidth were well fitted by the theoretical models in Equations 5 and 6 (Figure 4b; Figure S11, Supporting Information), indicating that the obtained temperature-dependent excitonic features are reliable. In addition, we noted that the coupling strength in the system slightly decreased along with the temperature rise (Table S3, Supporting Information), which is likely resulted from the lower exciton population coupled to the Mie resonance at high temperatures.[43] Furthermore, this optical exciton tuning in MoS_2 nanowires is estimated to happen at a timescale of several nanoseconds[44] in a fully reversible and highly repeatable way (Figure 4c), highlighting their potential applications in light modulation and tunable optical devices.

3. Conclusion

We report MoS_2 nanowires as subwavelength resonators that support strong light-matter coupling and Mie-exciton

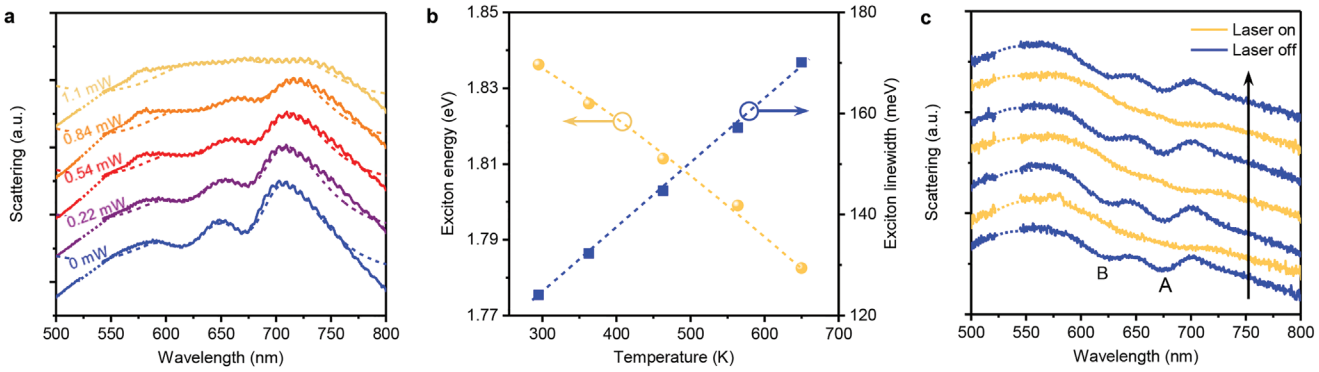

Figure 4. Optical modulation of excitons. a) Measured scattering spectra of a MoS_2 nanowire under 532 nm laser irradiation with an optical power of 0, 0.22, 0.54, 0.84, and 1.1 mW. The dashed lines show the CMT fitting curves. b) Temperature-dependent energy and linewidth of A exciton. The yellow and blue dashed lines show the corresponding fitting curves by the O'Donnell model and linear fitting, respectively. c) High reproducibility of the cycling (along the black arrow) of optical scattering spectra between laser on and off states.

polaritons at room temperature. The TMDC nanoresonators present a new class of dielectric materials for integrated photonics systems, such as waveguides, metamaterials, and optical modulators.[21] With the existence of Mie resonances and excitonic responses, they also provide a promising platform to be coupled to other active materials, such as quantum dots and monolayer TMDCs, to tailor their linear and/or nonlinear emission.[45–47] The MoS_2 excitonic properties can be further tuned due to the strong light-to-heat conversion, leading to all-optical modulation of scattering responses at the exciton wavelengths. This reversible and reproducible thermo-optic modulation makes MoS_2 nanowires promising as tunable optical components in integrated photonics, such as all-optical switch,[44] optical nanoantennas,[48] and metalenses.[49] In addition, the colloidal state of MoS_2 nanowires presented here offers extra flexibility for their implementation in photonic devices. For example, the easy integration of optical manipulation[50,51] and electric manipulation[30,52,53] techniques permits the controlled trapping, positioning, and assembly of multiple nanowires to more complex superstructures for enhanced functionalities.

4. Experimental Section

Synthesis of MoS_2 Nanowires: First, MoO_3 nanowires were synthesized as the precursor via a facile hydrothermal method. In a typical synthesis, 1 g ammonium heptamolybdate tetrahydrate ($(NH_4)_6Mo_7O_{24}{\cdot}4H_2O$) was dissolved into 20 mL deionized (DI) water under vigorous stirring, followed by the addition of 5 mL HNO_3. The as-prepared solution was then transferred to a 30 mL Teflon autoclave and heated at 180 °C for 20 h. After cooling, white precipitates were collected, washed, centrifuged, and dried overnight to obtain the powder of MoO_3 nanowires. Next, MoS_2/MoO_2 hybrid nanowires were synthesized by a chemical vapor deposition method in a vacuum tube furnace. In a typical process, two quartz boats filled with 0.1 g as-synthesized MoO_3 nanowires and 0.5 g sulfur powder, respectively, were inserted into a one-end-sealed quartz tube with a 20 cm distance. Ar gas (50 sccm) was used as the carrier gas. The tube pressure was reduced to 20 mTorr, and the heating temperature was set as 500 °C. At this temperature, sulfur vapor was carried downstream to react with MoO_3 nanowires for about 30 min, after which the white MoO_3 powder turned black as MoS_2/MoO_2 nanowires powder. Last, pure MoS_2 nanowires were synthesized by a further sulfurization of the as-obtained MoS_2/MoO_2 powder for 30 min. A similar setup as mentioned above was used, except the temperature was set at 900 °C, and the Ar gas flow was set at 50 sccm.

Structural and Compositional Characterizations: The morphology and crystal structure of MoS_2 nanowires were characterized using a Hitachi S-5500 SEM and a JEOL 2010 TEM. The composition of MoS_2 nanowires was characterized by Raman (Alpha 300, excited by 475 nm laser) and XRD (Rigaku MiniFlex 600).

Dark-Field Optical Spectroscopy: An inverted microscope (Nikon TiE) equipped with a 100× oil objective (Nikon, NA 0.5–1.3) was used. An oil-immersion dark-field condenser with a NA of 1.20–1.43 was used to focus the white illuminating light onto the MoS_2 nanowire from the top. A linear polarizer (Thorlabs) was used to filter unpolarized white light into linearly polarized light. The forward scattering signal from the MoS_2 nanowire was directed to an optical spectrometer (Andor) with a 500 nm grating. Background spectra were also recorded and subtracted to obtain the scattering signal of the MoS_2 nanowires. The scattering spectra were finally normalized to the intensity of the incident light. In the optical exciton tuning experiments, a 532 nm laser (Coherent, Genesis MX STM-1 W) was directed to the microscope to heat the MoS_2 nanowire. A notch filter (NF 533-17, Thorlabs) was used to block the laser signal from entering the spectrometer.

COMSOL Simulations: The dielectric function of MoS_2 was described using the Lorentz oscillator model. Three oscillators were included in the expression to account for the ground state transitions of A, B, and C excitons, respectively

$$\varepsilon = \varepsilon_b + \sum_{j=1}^{3} f_j \frac{\omega_{ex,j}^2}{\omega_{ex,j}^2 - \omega^2 - i\gamma_{ex,j}\omega} \tag{7}$$

where ε_b = 13.7 is the background permittivity from higher energy transitions, f_j, $\omega_{ex,j}$, and $\gamma_{ex,j}$ are the oscillator strengths, exciton energies, and exciton full widths of the three oscillators. All these ten parameters are determined by fitting, leading to reasonable agreement in line shape with the data from experiments, whereas better fits are viable if additional excited states of the excitons are included in the model.[54] In our current model, $f_1 = 0.7$, $\omega_{ex,1} = 1.84$ eV, and $\gamma_{ex,1} = 0.12$ eV for A exciton, $f_2 = 0.75$, $\omega_{ex,2} = 2.03$ eV, and $\gamma_{ex,16} = 0.16$ eV for B exciton, and $f_3 = 6.5$, $\omega_{ex,3} = 2.72$ eV, and $\gamma_{ex,3}$ = 0.57 eV for C exciton, respectively (Figure S5a, Supporting Information). The scattering and absorption properties of MoS_2 nanowires were simulated using the wave optics module of COMSOL Multiphysics 5.4. Because the lengths of the nanowires are much greater than the wavelengths of light, the nanowires were simply modeled on the cross-sectional plane as rectangles. To account for the real morphology from chemical synthesis, we rounded all the corners with a radius of 30 nm unless specified otherwise. The corner roundedness only slightly affects the magnitude of the simulated results with negligible effects on the spectral features (Figure S12, Supporting Information). The dielectric function of the MoS_2 nanowires was assumed to be the same as those in the bulky state.[55] For calculation of the forward scattering signal as collected in the experiments, the differential power flow was integrated in the forward direction over an arc that spans the angle corresponding to the numerical aperture of the objective. Laser-induced heating of MoS_2 nanowires is simulated using the heat transfer module. The system is modelled as a filleted block with dimensions 5 µm x 160 nm x 65 nm, with a fillet of 10 nm on all edges placed on a glass substrate. The heat capacity and thermal conductivity of MoS_2 NWs are functions of temperature.[56] The glass substrate has a heat capacity of 730 J kg^{-1} K^{-1} and thermal conductivity of 1.4 W m^{-1} K^{-1}. The heat source for the MoS_2 nanowire is modelled as a Gaussian profile with a beam radius of 500 nm and laser-beam power of 0.2–1.2 mW. The absorption at the laser wavelength (532 nm) is determined by using the method in ref. [57]. The heat flux through the MoS_2 nanowire surface boundaries and the top glass surface is set as convection with a net heat transfer coefficient of 10 W m^{-2} K^{-1} and a room temperature of 20 °C. All other glass domain boundaries (away from the MoS_2 nanowire) are set to be at room temperature.

Statistical Analysis: Scattering spectra are normalized to [0,1] before plotting the scattering map. The CMT fittings were performed using MagicPlot with the equations manually written into the software. The software used the iterative Levenberg–Marquardt nonlinear least squares curve fitting algorithm to find the minimum residual sum of squares.

Supporting Information

Supporting Information is available from the Wiley Online Library or from the author.

Acknowledgements

J.L., K.Y., and Y.H. contributed equally to this work. Y.Z., J.L., K.Y., J.F., and P.S.K. acknowledge the financial supports of the National Institute of General Medical Sciences of the National Institutes of Health (DP2GM128446) and the National Science Foundation (NSF-ECCS-2001650). D.F. and Y.H. would like to thank the support from Welch Foundation (F-1734), National Science Foundation (CMMI-1563382 and EECS-1710922, EECS-1930649 in part).

Conflict of Interest

The authors declare no conflict of interest.

Data Availability Statement

The data that support the findings of this study are available from the corresponding author upon reasonable request.

Keywords

exciton polaritons, nanowires, strong coupling, thermo-optic tunability, transition metal dichalcogenides

Received: January 20, 2022
Revised: May 31, 2022
Published online: July 22, 2022

[1] S. Manzeli, D. Ovchinnikov, D. Pasquier, O. V. Yazyev, A. Kis, *Nat. Rev. Mater.* **2017**, *2*, 17033.
[2] K. S. Novoselov, A. Mishchenko, A. Carvalho, A. H. C. Neto, *Science* **2016**, *353*, aac9439.
[3] F. Xia, H. Wang, D. Xiao, M. Dubey, A. Ramasubramaniam, *Nat. Photonics* **2014**, *8*, 899.
[4] K. F. Mak, D. Xiao, J. Shan, *Nat. Photonics* **2018**, *12*, 451.
[5] K. F. Mak, C. Lee, J. Hone, J. Shan, T. F. Heinz, *Phys. Rev. Lett.* **2010**, *105*, 136805.
[6] A. Splendiani, L. Sun, Y. Zhang, T. Li, J. Kim, C.-Y. Chim, G. Galli, F. Wang, *Nano Lett.* **2010**, *10*, 1271.
[7] Q. H. Wang, K. Kalantar-Zadeh, A. Kis, J. N. Coleman, M. S. Strano, *Nat. Nanotechnol.* **2012**, *7*, 699.
[8] K. F. Mak, J. Shan, *Nat. Photonics* **2016**, *10*, 216.
[9] B. Radisavljevic, A. Radenovic, J. Brivio, V. Giacometti, A. Kis, *Nat. Nanotechnol.* **2011**, *6*, 147.
[10] S. Kim, A. Konar, W.-S. Hwang, J. H. Lee, J. Lee, J. Yang, C. Jung, H. Kim, J.-B. Yoo, J.-Y. Choi, Y. W. Jin, S. Y. Lee, D. Jena, W. Choi, K. Kim, *Nat. Commun.* **2012**, *3*, 1011.
[11] F. H. L. Koppens, T. Mueller, P. Avouris, A. C. Ferrari, M. S. Vitiello, M. Polini, *Nat. Nanotechnol.* **2014**, *9*, 780.
[12] O. Lopez-Sanchez, D. Lembke, M. Kayci, A. Radenovic, A. Kis, *Nat. Nanotechnol.* **2013**, *8*, 497.
[13] J. Pu, T. Takenobu, *Adv. Mater.* **2018**, *30*, 1707627.
[14] S. Wu, S. Buckley, J. R. Schaibley, L. Feng, J. Yan, D. G. Mandrus, F. Hatami, W. Yao, J. Vučković, A. Majumdar, X. Xu, *Nature* **2015**, *520*, 69.
[15] X. Liu, T. Galfsky, Z. Sun, F. Xia, E.-c. Lin, Y.-H. Lee, S. Kéna-Cohen, V. M. Menon, *Nat. Photonics* **2015**, *9*, 30.
[16] W. Liu, B. Lee, C. H. Naylor, H.-S. Ee, J. Park, A. T. C. Johnson, R. Agarwal, *Nano Lett.* **2016**, *16*, 1262.
[17] S. Lepeshov, M. Wang, A. Krasnok, O. Kotov, T. Zhang, H. Liu, T. Jiang, B. Korgel, M. Terrones, Y. Zheng, A. Alu, *ACS Appl. Mater. Interfaces* **2018**, *10*, 16690.
[18] P. Kumar, J. Lynch, B. Song, H. Ling, F. Barrera, K. Kisslinger, H. Zhang, S. B. Anantharaman, J. Digani, H. Zhu, T. H. Choudhury, C. McAleese, X. Wang, B. R. Conran, O. Whear, M. J. Motala, M. Snure, C. Muratore, J. M. Redwing, N. R. Glavin, E. A. Stach, A. R. Davoyan, D. Jariwala, *Nat. Nanotechnol.* **2021**, *17*, 182.
[19] D. N. Basov, M. M. Fogler, F. J. García de Abajo, *Science* **2016**, *354*, aag1992.
[20] F. Hu, Y. Luan, M. E. Scott, J. Yan, D. G. Mandrus, X. Xu, Z. Fei, *Nat. Photonics* **2017**, *11*, 356.
[21] H. Ling, R. Li, A. R. Davoyan, *ACS Photonics* **2021**, *8*, 721.
[22] A. I. Kuznetsov, A. E. Miroshnichenko, M. L. Brongersma, Y. S. Kivshar, B. Luk'yanchuk, *Science* **2016**, *354*, aag2472.
[23] S. Jahani, Z. Jacob, *Nat. Nanotechnol.* **2016**, *11*, 23.
[24] I. Staude, J. Schilling, *Nat. Photonics* **2017**, *11*, 274.
[25] T. D. Green, D. G. Baranov, B. Munkhbat, R. Verre, T. Shegai, M. Käll, *Optica* **2020**, *7*, 680.
[26] R. Verre, D. G. Baranov, B. Munkhbat, J. Cuadra, M. Kall, T. Shegai, *Nat. Nanotechnol.* **2019**, *14*, 679.
[27] B. Munkhbat, D. G. Baranov, M. Stührenberg, M. Wersäll, A. Bisht, T. Shegai, *ACS Photonics* **2019**, *6*, 139.
[28] X. Zhang, C. De-Eknamkul, J. Gu, A. L. Boehmke, V. M. Menon, J. Khurgin, E. Cubukcu, *Nat. Nanotechnol.* **2019**, *14*, 844.
[29] H. Zhang, B. Abhiraman, Q. Zhang, J. Miao, K. Jo, S. Roccasecca, M. W. Knight, A. R. Davoyan, D. Jariwala, *Nat. Commun.* **2020**, *11*, 3552.
[30] Y. Huang, K. Yu, H. Li, K. Xu, Z. Liang, D. Walker, P. Ferreira, P. Fischer, D. Fan, *Adv. Mater.* **2020**, *32*, 2003439.
[31] D. R. Abujetas, R. Paniagua-Domínguez, J. A. Sánchez-Gil, *ACS Photonics* **2015**, *2*, 921.
[32] G. Zengin, G. Johansson, P. Johansson, T. J. Antosiewicz, M. Käll, T. Shegai, *Sci. Rep.* **2013**, *3*, 3074.
[33] L. Cao, J. S. White, J.-S. Park, J. A. Schuller, B. M. Clemens, M. L. Brongersma, *Nat. Mater.* **2009**, *8*, 643.
[34] S.-Q. Li, K. B. Crozier, *Phys. Rev. B* **2018**, *97*, 245423.
[35] J. Cuadra, D. G. Baranov, M. Wersall, R. Verre, T. J. Antosiewicz, T. Shegai, *Nano Lett.* **2018**, *18*, 1777.
[36] A. Bisht, J. Cuadra, M. Wersall, A. Canales, T. J. Antosiewicz, T. Shegai, *Nano Lett.* **2019**, *19*, 189.
[37] B. Munkhbat, D. G. Baranov, A. Bisht, M. A. Hoque, B. Karpiak, S. P. Dash, T. Shegai, *ACS Nano* **2020**, *14*, 1196.
[38] L. Zhang, R. Gogna, W. Burg, E. Tutuc, H. Deng, *Nat. Commun.* **2018**, *9*, 713.
[39] J. van de Groep, J.-H. Song, U. Celano, Q. Li, P. G. Kik, M. L. Brongersma, *Nat. Photonics* **2020**, *14*, 426.
[40] W. Choi, M. Y. Cho, A. Konar, J. H. Lee, G.-B. Cha, S. C. Hong, S. Kim, J. Kim, D. Jena, J. Joo, S. Kim, *Adv. Mater.* **2012**, *24*, 5832.
[41] K. P. O'Donnell, X. Chen, *Appl. Phys. Lett.* **1991**, *58*, 2924.
[42] G. Moody, C. Kavir Dass, K. Hao, C.-H. Chen, L.-J. Li, A. Singh, K. Tran, G. Clark, X. Xu, G. Berghäuser, E. Malic, A. Knorr, X. Li, *Nat. Commun.* **2015**, *6*, 8315.
[43] T. W. Lo, Q. Zhang, M. Qiu, X. Guo, Y. Meng, Y. Zhu, J. J. Xiao, W. Jin, C. W. Leung, D. Lei, *ACS Photonics* **2019**, *6*, 411.
[44] Y.-S. Duh, Y. Nagasaki, Y.-L. Tang, P.-H. Wu, H.-Y. Cheng, T.-H. Yen, H.-X. Ding, K. Nishida, I. Hotta, J.-H. Yang, Y.-P. Lo, K.-P. Chen, K. Fujita, C.-W. Chang, K.-H. Lin, J. Takahara, S.-W. Chu, *Nat. Commun.* **2020**, *11*, 4101.
[45] J. Fang, M. Wang, K. Yao, T. Zhang, A. Krasnok, T. Jiang, J. Choi, E. Kahn, B. A. Korgel, M. Terrones, X. Li, A. Alù, Y. Zheng, *Adv. Mater.* **2021**, *33*, 2007236.
[46] G. Hu, X. Hong, K. Wang, J. Wu, H.-X. Xu, W. Zhao, W. Liu, S. Zhang, F. Garcia-Vidal, B. Wang, P. Lu, C.-W. Qiu, *Nat. Photonics* **2019**, *13*, 467.
[47] X. Hong, G. Hu, W. Zhao, K. Wang, S. Sun, R. Zhu, J. Wu, W. Liu, K. P. Loh, A. T. S. Wee, B. Wang, A. Alù, C.-W. Qiu, P. Lu, *Research* **2020**, *2020*, 9085782.
[48] L. Ding, D. Morits, R. Bakker, S. Li, D. Eschimese, S. Zhu, Y. F. Yu, R. Paniagua-Dominguez, A. I. Kuznetsov, *ACS Photonics* **2020**, *7*, 1001.
[49] P. P. Iyer, R. A. DeCrescent, T. Lewi, N. Antonellis, J. A. Schuller, *Phys. Rev. Appl.* **2018**, *10*, 044029.

[50] J. Li, Y. Liu, L. Lin, M. Wang, T. Jiang, J. Guo, H. Ding, P. S. Kollipara, Y. Inoue, D. Fan, B. A. Korgel, Y. Zheng, *Nat. Commun.* **2019**, *10*, 5672.
[51] J. Li, Y. Zheng, *Acc. Mater. Res.* **2021**, *2*, 352.
[52] K. Kim, X. Xu, J. Guo, D. L. Fan, *Nat. Commun.* **2014**, *5*, 3632.
[53] D. L. Fan, F. Q. Zhu, R. C. Cammarata, C. L. Chien, *Nano Today* **2011**, *6*, 339.
[54] Y. Li, A. Chernikov, X. Zhang, A. Rigosi, H. M. Hill, A. M. van der Zande, D. A. Chenet, E.-M. Shih, J. Hone, T. F. Heinz, *Phys. Rev. B* **2014**, *90*, 205422.
[55] A. R. Beal, H. P. Hughes, *J. Phys. C: Solid State Phys.* **1979**, *12*, 881.
[56] X. Gu, B. Li, R. Yang, *J. Appl. Phys.* **2016**, *119*, 085106.
[57] M. Bernardi, M. Palummo, J. C. Grossman, *Nano Lett.* **2013**, *13*, 3664.

ADVANCED SCIENCE Open Access
www.advancedscience.com

Colloidal Quantum Dot Light Emitting Diodes at Telecom Wavelength with 18% Quantum Efficiency and Over 1 MHz Bandwidth

*Santanu Pradhan, Mariona Dalmases, Nima Taghipour, Biswajit Kundu, and Gerasimos Konstantatos**

Developing high performance, low-cost solid-state light emitters in the telecom wavelength bandwidth is of paramount importance for infrared light-based communications. Colloidal quantum dot (CQD) based light emitting diodes (LEDs) have shown tremendous advances in recent times through improvement in synthesis chemistry, surface property, and device structures. Despite the tremendous advancements of CQD based LEDs in the visible range with efficiency reaching theoretical limits, their short-wave infrared (SWIR) counterparts mainly based on lead chalcogenide CQDs, have shown lower performance (≈8%). Here the authors report on highly efficient SWIR CQD LEDs with a recorded EQE of 11.8% enabled by the use of a binary CQD matrix comprising QD populations of different bandgaps at the emission wavelength of 1550 nm. By further optimizing the optical out-coupling via the use of a hemispherical lens to reduce optical waveguide loss, the EQE of the LED increased to 18.6%. The CQD LED has an electrical bandwidth of 2 MHz, which motivated them to demonstrate its use in the first SWIR free-space optical transmission link based entirely on CQD technology (photodetector and light emitter) opening a new window of applications for CQD optoelectronics.

1. Introduction

Infrared light-based communication in the eye-safe window ≈1500 nm is sought to revolutionize diverse fields of applications—namely, remote control, LiFi, robotics, machine vision, inter- and intra- machine communications, Internet of things (IoT), medical and biological applications, etc.[1–5] To accommodate the requirements for consumer electronics, the underlying optoelectronic components need to offer low-cost, high-volume manufacturing, and complementary metal-oxide semiconductor (CMOS) compatibility. To date, such applications are served by III-V InGaAs based light emitting diodes (LEDs) and photodetectors that are characterized by high cost, limited production capacity, and lack of monolithic integration to silicon.[6] To this end, efforts on developing solution processed optoelectronics for free-space data transfer and IoT applications have been intensified using organic or perovskite semiconductors, yet those operate in the visible or near-infrared imposing constraints on optical ambient light interference and eye-safety regulations.[7–9] Colloidal quantum dots (CQD)-based optoelectronics recently emerged as one of the most promising technologies to address the market needs in the eye-safe short-wave infrared (SWIR) region, thanks to their low-cost solution processability, large area manufacturing, band gap tunability, and complementary metal-oxide semiconductor (CMOS) compatibility.[1,10,11]

The optical source is of paramount importance for the deployment of such technology and despite compelling performance of CQD-LEDs in the visible with EQEs over 20%,[12–15] infrared CQD LEDs, particularly based on lead sulfide (PbS) CQDs have remained under performing with a reported EQE of ≈8% at an emission wavelength of ≈1300–1400 nm.[16,17] Recently, CQD LEDs based on Ag_2S (silver sulfide) have been reported to reach an EQE as high as 17% with proper shelling and perovskite matrix incorporation techniques. Although the performance was high at the 1200–1400 nm region, the efficiency drops below 8% for emission wavelength at ≈1500 nm.[18] Albeit these were record EQE for CQD LEDs, it remains below the EQE performance of single crystalline III-V LEDs. Moreover, the use of light at 1550 nm is favorable in terms of eye-safety yet to date efficient solution-processed LEDs at this wavelength have remained elusive.

S. Pradhan[+], M. Dalmases, N. Taghipour, B. Kundu, G. Konstantatos
ICFO-Institut de Ciències Fotòniques
The Barcelona Institute of Science and Technology
Castelldefels, Barcelona 08860, Spain
E-mail: gerasimos.konstantatos@icfo.es
G. Konstantatos
ICREA—Institució Catalana de Recerca i Estudis Avançats
Passeig Lluís Companys 23, Barcelona 08010, Spain

The ORCID identification number(s) for the author(s) of this article can be found under https://doi.org/10.1002/advs.202200637

[+]Present address: Centre of Nanotechnology, Indian Institute of Technology Roorkee, Roorkee 247667, India

DOI: 10.1002/advs.202200637

Previously highly efficient SWIR CQD LEDs have relied on the use of perovskite[18–20] or CQD matrix comprising PbS CQDs with a larger bandgap than of the emitter CQDs.[16,17,21] The EQE performance recorded in those prior reports reached ≈8% and was achieved at 1300–1400 nm. Here, we demonstrate highly efficient CQD LEDs emitting at 1550 nm with an EQE of 18%. We report a modified technique that uses two matrix QDs of slightly different bandgaps instead of one matrix QD to form a heterojunction with emitter QDs with a much lower bandgap. The use of a two different bandgap QDs based matrix improved the performance of the device through balanced charge injection, improved light emission, and overall injection efficiency. Utilizing an optimized mixing of 1.75 and 1.35 eV bandgap QD based matrix forming heterojunction with 0.79 eV (excitonic peak ≈1550 nm) bandgap QD based emitters showed an EQE as high as 11.8% while emitting ≈1550 nm. The EQE was further improved to 18.6% utilizing a hemispherical lens attached to the glass substrate of the device to reduce the optical waveguide loss.

2. Results and Discussion

Figures 1a,b show the schematic of a single matrix-based blend and blended matrix-based devices. The single matrix devices comprise a matrix of QDs with higher bandgap and emitter QDs with lower bandgap. On the other hand, for the blended matrix, the matrix comprised a blend of two size populations of QDs (i.e., possessing different bandgaps) with defined mixing ratios. The emitter QDs bandgap for blended matrix devices are significantly lower than either of the matrix QDs bandgap so that charge transfer can be effectively facilitated from matrix to emitter. Previously, we had reported that binary devices with high bandgap PbS QDs as matrix and lower bandgap PbS as emitter show significantly higher photoluminescence quantum yield (PLQY) and EQE compared to emitter only devices.[16] A higher bandgap matrix showed better performance and a lower efficiency droop in the high radiance region due to a balanced charge carrier injection.[17] We have extended this idea to the emission of 0.79 eV emitter-based devices, though the difference in conduction and valence band offset in this case leads to a decrement in device performance. As a consequence, we have utilized blended matrix-based device to tune the charge injection and hence the device performance. Figure 1c shows the effect of different matrixes on the EQE of the binary and blended matrix-based devices. 1.75 eV matrix-based binary devices showed peak EQE of 7.9% with significantly high efficiency droop in the high injection regime. On the other hand, 1.35 eV matrix-based devices showed a peak EQE of 6.6% with a reduced EQE droop in the high current injection regime (although these devices showed a significantly high efficiency droop in the lower current injection regime). These differences in efficiency droop resulted from the charge imbalance of injected hole and electrons in different regions associated with the difference of conduction and valence band offset between emitter and matrix QDs. Putting emitters in the blended matrix comprised of 1.75 and 1.35 eV QDs significantly improves the EQE as well as the efficiency droop both in lower and higher current injection regimes as shown in Figure 1c. The controlled blended matrix (comprised of 10% 1.35 eV QDs and 90% 1.75 eV QDs) based device showed an EQE as high as 11.8% (10.4±0.7)% (Figure S1, Supporting Information). The effect of different matrices mixing with different ratios is shown in Figures S2 and S3, Supporting Information. A combination of balanced charge injection and improved injection efficiency give rise to the improvement of EQE for blended matrix-based devices. As a result, the blended matrix-based devices showed higher EQE compared to 1.35 eV matrix based binary devices in the low radiance regime and with respect to 1.75 eV matrix based binary devices in the higher radiance regime (Figure 1d). The electroluminescence (EL) spectra as a function of applied bias are shown in Figure 1e. Inset shows the infrared emission of these devices as captured with an InGaAs camera (Iberoptics Sistemas Ópticos). In this class of devices, a significant portion of generated light in the active layer is waveguided through the substrate to the edge of the structure leading to increased optical losses. The optical loss due to waveguide through substrates and other layers is estimated at ≈60% as shown in Figure S4, Supporting Information. Thus, LED light outcoupling can be drastically improved by reducing waveguiding loss. Previously, improvement of device EQE by reducing waveguide loss has been demonstrated for various types of visible LEDs.[22–24] Here, we have addressed this problem by attaching a hemispherical lens with a refractive index matching that of the substrate as shown in Figure 1f (Figure S5a, Supporting Information). By doing so we note a significant improvement of EQE to ≈18.6% setting a new record for SWIR CQD LEDs. The implementation of a lens does not alter the spectral emission of the LED (Figure S5b, Supporting Information).

To understand the underlying mechanism of such an elevated performance, we have performed photoluminescence (PL) characterizations of the binary and different blended matrix-based films. Figure S6a, Supporting Information, shows the PL spectra of the binary and blended matrix-based films. Both binary as well as blended matrix devices showed a strong emission corresponding to the emitter QD bandgap. No matrix emission observed for either of these devices suggests efficient charge transfer from matrix to emitters. The PLQY of different devices is summarized in **Figure 2**a. 1.75 eV matrix based binary devices showed a PLQY as high as 68% compared to 52% for 1.35 eV matrix based binary devices. We posit that these differences arise from the difference of conduction and valence band offsets between emitter and matrix for a 1.75 and 1.35 eV-based matrix. A relatively deeper well formed by the adjacent matrix and emitter QDs in 1.75 eV matrix based binary mix gives rise to better confinement of charge carriers and subsequently higher radiative recombination. The blended matrix-based devices showed systematic PLQY in between the values obtained with single matrix QD based blends. A 10% matrix mix (10% 1.35 eV QDs in the blend) and 30% matrix mix (30% 1.35eV QDs in the blend) showed PLQY ≈66% and ≈59%, respectively. The most significant observation from this result is that the PLQY can be tuned by controlling the ratio of matrices in the mix. The PL decay curves as shown in Figure S6b, Supporting Information, also support this with a similar trend. PL decay curves are fitted with double exponential decay times. The faster component corresponds to the emitter recombination whereas the slower one indicates the matrix to emitter charge transfer.[16] All the curves showed a similar fast decay component but significantly different slow decay component (the time decay parameters are summarized in Table S1, Supporting Information). Figure 2b shows the

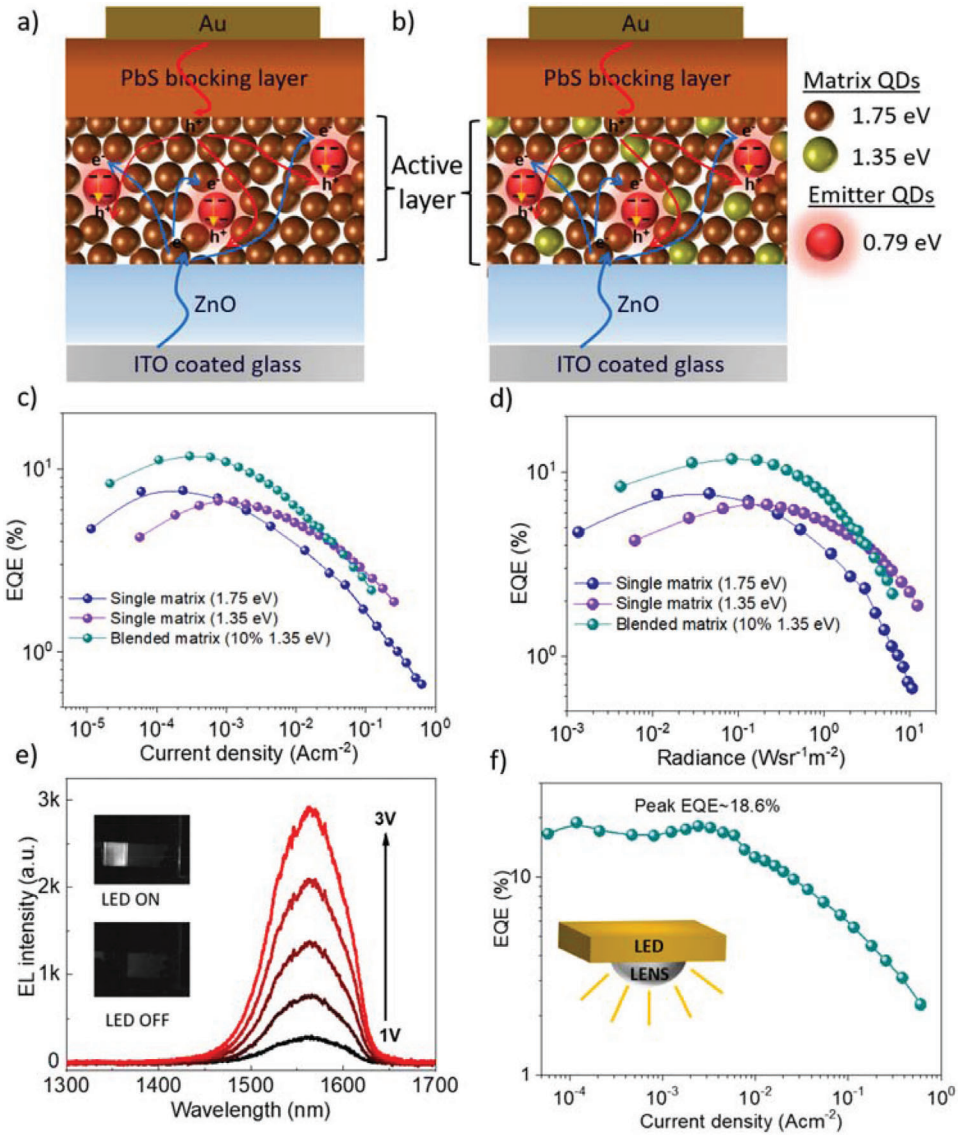

Figure 1. Performance of LED devices: a,b) schematic of binary and blended matrix CQD LED devices. Binary devices comprised of high bandgap matrix and low bandgap emitter QDs. The charges are transferred from matrix to emitter to get the light emission from the emitter sites in the blend (a). Blended matrix-based devices were formed with matrix QDs of two different bandgaps along with the emitter QDs. The matrix of mixed nature controls the charge injection and charge transfer to the emitter sites and hence improve the device performance (b). c) EQE of the devices as a function of injection current density. Blended matrix-based devices showed better performance over binary (single matrix QD) devices. d) EQE as a function of radiance. Blended matrix-based devices showed better performance for most of the range of device radiance. e) Light emission from the LED devices as a function of applied voltage. Inset shows the picture of LED devices with and without applied voltage captured with infrared camera. f) EQE of the lens attached LED devices as a function of applied current. Inset shows the schematic of the hemispherical lens attached to the substrate of the LED device to reduce the substrate induced optical waveguide loss.

injection current density plot as a function of applied voltage with the variation of matrix composition. The blended matrix-based devices showed a lower injection current compared to the single matrix based binary devices. The injection current in the blended matrix-based devices can be tuned as a function of blend ratio. The energy band scenarios of the active material ensembles for both single matrix or blended matrix-based devices are depicted in Figure S7, Supporting Information. Within the blended matrix, the charge injection procedure is complicated compared to the single matrix-based device as there are a higher number of injection paths available compared to the single matrix-based devices. Once the charges reach matrix QDs, they will be transferred to the emitter sites irrespective of their band position as described in Section S8, Supporting Information. Moreover, we have computed the injection efficiency of the blended matrix-based device with SCAPS (Section S9, Supporting Information). The injection efficiency determines the fraction of charge carriers that are injected in the active material, participating in the recombination procedure. The simulation shows the variation of injection efficiency as a function of 1.35 eV QD loading in the blended matrix.

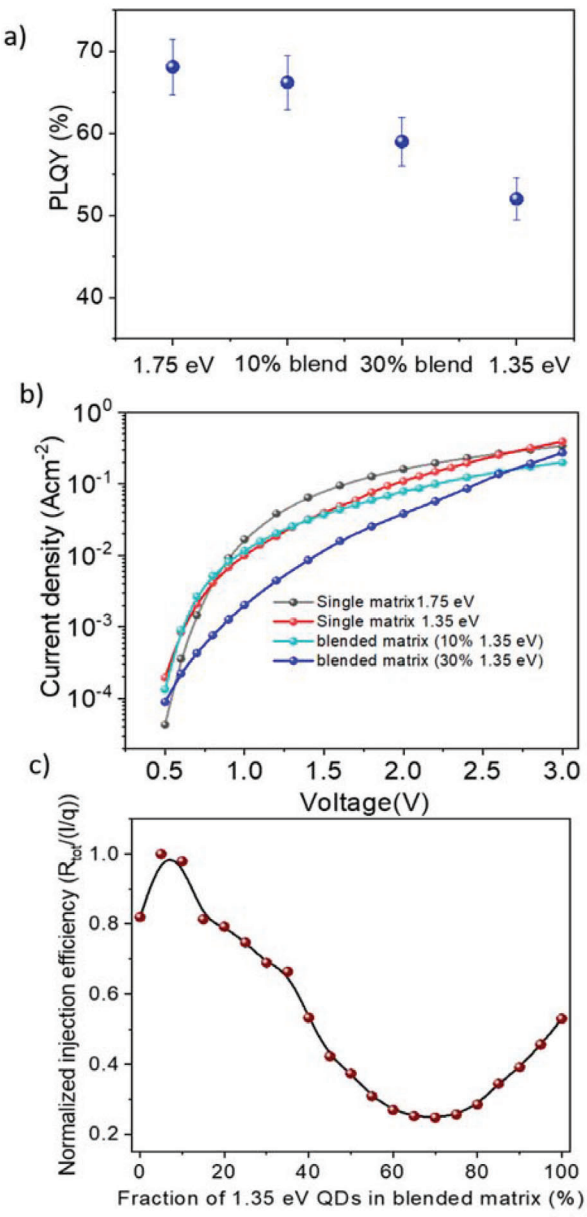

Figure 2. Variation of optical properties and charge injection as a function of blend ratio: a) the PLQY of the binary devices with single matrix and blended matrix. The 1.75 eV matrix-based devices showed PLQY as high as 68% whereas the 1.35 eV matrix-based devices showed a PLQY of 52%. PLQY of the blended matrix-based devices varies systematically in-between with QD mixing ratio. b) The variation of injection current density as a function of applied voltage with single and blended matrix-based devices. Blended matrix-based devices showed lower current injection indicating the control over charge injection through the variation of blend ratio. c) Injection efficiency as simulated with SCAPS, varies as a function of 1.35 eV QD loading in the matrix. Injection efficiency showed a similar trend as observed with device performance.

The efficiency improves at a very low loading (0–10%) and decreases significantly with higher loading as shown in Figure 2c. Although the simulation conditions used in this case were much simpler than the actual problem, it showed a trend similar to the device performance variation as a function of matrix QD variation. The blended matrix can tune the PLQY as well as control the charge injection efficiency. EQE of an LED depends on the PLQY, injection efficiency, charge balance, etc.[17,19] The tuning of these parameters through blended matrix QDs leads to a higher EQE compared to their single matrix-based counterparts. The strong variation of PLQY and injection efficiency as a function of matrix QD loading ratio suggests their strong influence in determining the device performance.

To further assess the potential of this class of LEDs for free-space optical transmission applications, besides efficiency modulation bandwidth is another critical figure of merit. **Figure 3**a shows the schematic of the experimental setup we used to determine the frequency response and modulation bandwidth of the LEDs (details of the setup is described in the Experimental Section). The effect of applied bias frequency on the electroluminescence signal is depicted in Figure 3b. It shows that the amplitude of the EL signal remains similar for 1 and 500 kHz applied frequencies. To find the modulation frequency, we have scanned the EL amplitude of the LEDs as a function of applied frequency. The modulation bandwidth [corresponding to the 3 dB frequency (frequency at which the amplitude reduces to 70%)] as a function of applied bias voltage is shown in Figure 3c. The modulation bandwidth increases from 0.62 MHz for 1 V bias to 2.45 MHz for 2.5 V bias due to a faster time of flights of the charge carriers. The variation of EL signal as a function of applied bias is shown in Figure S11, Supporting Information. To our understanding, this is the first time such a high modulation width is reported for CQD based infrared LEDs considering slower PL decay time of these materials. To understand the origin of such an improved modulation bandwidth, we have studied the EL decay time. Like the PL, EL also showed two component decays as shown in Figure 3d. The fast component is corresponding to emitter radiative emission and slower component is related to charge transport in the active materials. A closer look at the EL decay curve showed that the faster component comprises more than 80% of the decay curve (Figure 3d). Thus, the faster decay (in sub-microseconds) of these materials contributed to the improved modulation bandwidth. Figure 3e shows the variation of the faster component of the rise and decay time of EL signal as a function of applied voltage bias. Faster rise and decay time correspond to the increased charge time-of-flight in the active materials. The improvement of rise and decay time contributes to the improvement of the modulation bandwidth.[25]

To create an optical link, besides the light source, a photodetector is needed on the receiver side. Recently, PbS QDs with an excitonic peak in SWIR region-based photodiodes have shown high quantum efficiency.[26] Here, we have utilized PbS QDs with an excitonic peak ≈1550 nm (similar to the emission wavelength of the LED devices) to form depleted heterojunction photodiodes following the success of similar structure in PbS QD based solar cells. **Figure 4**a shows the responsivity of the photodiode over visible to SWIR region. A clear excitonic peak ≈1560 nm with a reasonable responsivity of 0.21 A W^{-1} was observed. The EL emission from the LED devices showed a similar peak position making it an ideal combination for an integrated signal transmitter and receiver-based communication devices. Further, the current–voltage (I–V) response curve showed the photo-response of the devices with incident light intensity (λ = 1560 nm) as low as 0.26 μW cm^{-2} confirming the effectiveness of the

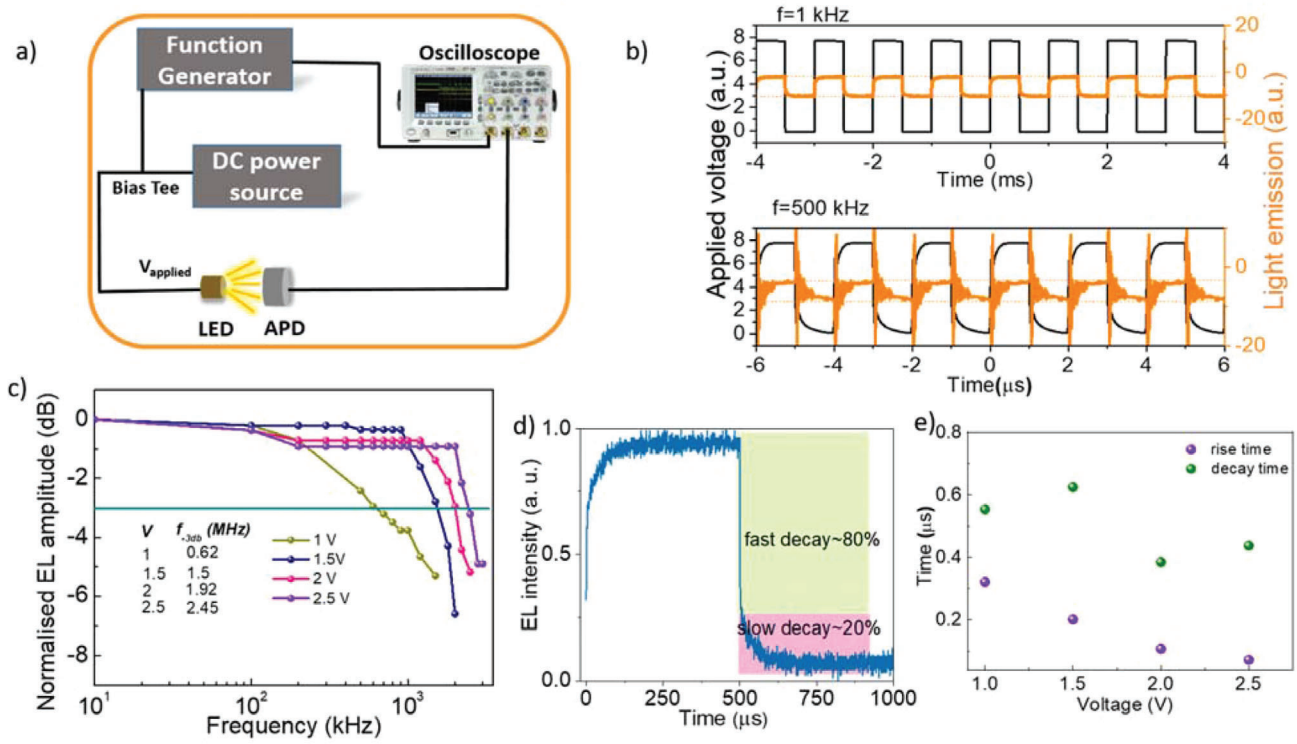

Figure 3. Modulation properties of CQD LED devices: a) schematic of the frequency modulation characterization setup for CQD LED devices. b) Applied voltage bias (black) and related light emission from the LED device (orange) for an applied frequency of 1 and 500 kHz as captured with the oscilloscope. c) Normalized EL amplitude of the LED devices as a function of applied voltage bias. Inset shows the corresponding modulation bandwidth. Modulation bandwidth improves with higher applied bias as a consequence of improved time of flights of the charge carriers. d) EL decay curve of the LED devices comprises of fast decay component (more than 80% weightage) and a slow decay component. Such a faster decay component contributes to the high modulation bandwidth. e) The variation of the faster component of rise and decay time of the EL signal as a function of applied bias. The data were taken for an input signal frequency of 500 kHz. The variation of EL signals as a function of applied bias is shown in Figure S11, Supporting Information. The faster time constants were observed with increased voltage bias due to increased charge carrier time of flights.

photodiodes in detecting low optical signal as shown in Figure 4b. The rise and decay time of the photodiode is of utmost importance to determine its efficiency as the signal receiver. The transient photo-current behavior of the photodiode with an incident light of wavelength 1560 nm is shown in Figure 4c. It shows the decay time of the photodiode is ≈0.7 μs limited by the mobility and the trap density in the active materials. These response times are in the same order of the LED EL and PL decay times making it an ideal component for being a signal receiver for the integrated devices. Figure 4d shows the schematic of a CQD thin film based integrated short-ranged signal communication system comprising the blended matrix-based LED devices as signal transmitter and PbS QD based photodiode as signal receiver. The distance between transmitter and receiver was fixed at 5 cm. The response signals as received by the photodiodes with input signals of frequency 1 and 100 kHz, respectively, are shown in Figure 4e. The amplitude of the received is preserved for 100 kHz applied frequency. Figure 4d shows the change of amplitude of the received signal as a function of applied frequency. The 3 dB frequency (modulation bandwidth) was determined as 415 kHz. To our knowledge, this is the first realization of an infrared short-range communication system based entirely on solution-processed optoelectronic devices.

3. Conclusion

In summary, we have reported a novel technique of blending QDs with controlled mixing of two different matrix QDs to achieve a record high EQE for 1550 nm based CQD LEDs and further improved it by reducing waveguiding optical loss through the utilization of hemispherical lens. The device efficiency competes favorably with commercially available LEDs emitting at 1550 nm (Table S3, Supporting Information) based on III-V InGaAs. Moreover, we have studied the potential of these devices for the application in short-range infrared communications. We have reported modulation bandwidth in the megahertz range and demonstrated an all-CQD-based integrated system comprising a LED and a photodiode, for short-range infrared communications.

4. Experimental Section

Synthesis of PbS QDs: 1.75, and 1.35 eV excitonic peak based PbS QDs, used as the matrix materials for the devices, were synthesized using standard Schlenk technique. In brief, 0.446 g lead oxide (PbO), 1.6 mL oleic acid, and 18 mL 1-octadecene (ODE) were pumped for 1 h at 100 °C. For 1.75 eV PbS QDs, the temperature was set to 80 °C and 1 mmol hexamethyldisilathiane (HMS) mixed with 5 mL ODE was injected

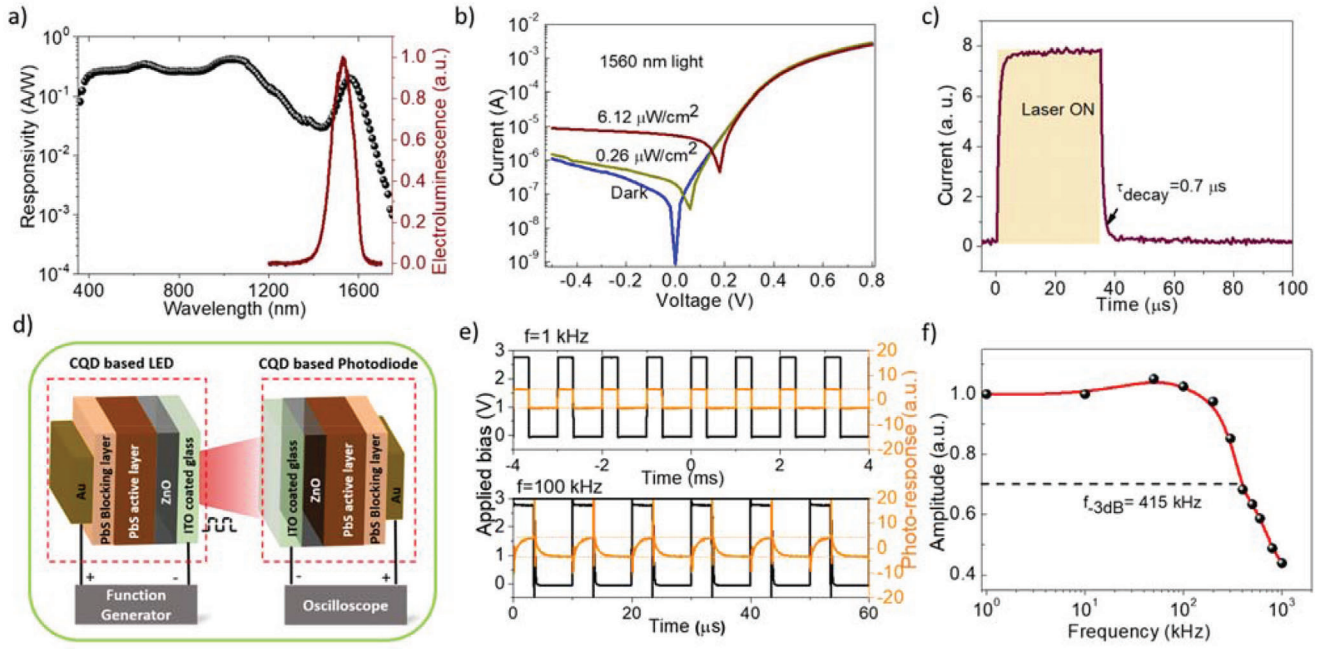

Figure 4. All PbS CQD based integrated device performance for short-range communications: a) the responsivity of the photodiode based on 1560 nm excitonic peak PbS CQD. The responsivity shows reasonable response throughout the wavelength region of 400 to 1650 nm. The responsivity peak corresponding to the QD excitonic peak matches well with the electroluminescence peak of the LED device. b) Dark and light current–voltage characteristics of the photodiode. Change of photocurrent in the reverse bias observed with the 1560 nm incident light was observed. c) Fast photocurrent decay observed in 1560 nm PbS QD based photodiodes. d) Schematic of all PbS CQD based integrated device designed for short-range communications. The blended CQD matrix-based LED was used as the signal transmitter and PbS QD based photodiode was used as the signal receiver. The distance between the transmitter and receiver was 5 cm. e) Frequency response of the receiver photodiode with frequencies 1 and 100 kHz, respectively. The applied voltage bias signal to the LED (black) and signal received with the photodiode (orange) were captured with the oscilloscope. f) Amplitude of the received signal as a function of applied frequency. The modulation bandwidth observed as 415 kHz.

immediately. The reaction was quenched with cold acetone after 20 s and the QDs were isolated by precipitation. The QDs were further purified by dispersion/precipitation with toluene/acetone 3 times. For 1.35 eV QDs, the temperature was set at 80 °C and right after the injection, the heating was stopped (without removing the heating mantle) and the solution was allowed to cool down gradually (≈1 h).

0.79 eV excitonic peak based PbS QDs were synthesized by a previously reported multi-injection method with modification.[27] Typically, 0.446 g PbO, 3.8 mL oleic acid, and 50 mL ODE were mixed together at 100 °C under vacuum for 1 h. Once under argon, a solution of 65 µL HMS in 3 mL ODE was quickly injected. After 6 min, a second injection of 80 µL of HMS in 9 mL of ODE was dropwise injected and then, the heating was stopped immediately and the solution was cooled down gradually to room temperature. The QDs were purified three times with a mixture of acetone/ethanol, redispersing in toluene. The final concentration of all the PbS QDs solutions was adjusted to 30 mg mL^{-1} before the LED device preparation.

ZnO NC Synthesis: ZnO NCs were synthesized following standard method as described in the authors' previous report.[17] 2.95 g zinc acetate dihydrate was dissolved in 125 mL methanol solvent and the temperature of the reaction bath was set to 60 °C. In a separate vial, 1.48 g potassium hydroxide (KOH) (85%) flakes were dissolved in 65 mL methanol. Under continuous stirring, the KOH solution was then added dropwise to the zinc acetate solution for a time span of 4–5 min while the reaction temperature was fixed at 60 °C. After 2.5 h, the heating source was removed, and the reaction bath was allowed to cool down to room temperature. The solution was then transferred to centrifuge tubes and centrifuged at 5000 rpm for 5 min. The supernatants were then discarded and remnants were washed again with methanol following the similar procedure and finally dried in nitrogen flow to get ZnO NCs. For electron injection layer, ZnO NCs were dispersed in a solution of 2% butylamine in chloroform with a concentration of 80 mg mL^{-1}.

LED Device Preparation: LEDs were prepared on pre-cleaned ITO coated glass as described in the authors' previous report.[16] ZnO NCs in chloroform (80 mg mL^{-1}) was spun on top of the substrate with a spin speed of 4000 rpm to form the electron injection layer of ≈80 nm. The active layer was deposited on top of the ZnO layer. For blended devices, all QDs (1.75, 1.35, and 0.79 eV excitonic peak based PbS) were prepared in separate vials with the same concentration (30 mg mL^{-1}) before mixing. For binary blends, emitter PbS QDs were mixed to matrix PbS QDs as 7.5% mixing ratio. For blended matrix devices, 1.35 and 1.75 eV exciton peak based QDs were mixed with different mixing ratios. Then, the blended matrix QDs were added to emitter QDs so that in the final solution 7.5% emitter QDs were present. Zinc iodide (ZnI_2) and 3-mercaptopropionic acid (MPA) were mixed to use as ligand for solid state QD film formation as described elsewhere.[28] The thickness of the active layer was adjusted as ≈60 nm by repeating the ligand treatment procedure three times. The hole-transporting layer of ≈50 nm was formed using the PbS QDs (1.35 eV PbS QD) treated with 0.02% 1,2-ethanedithiol (EDT) in acetonitrile solution. The top electrode was formed by thermally evaporated Au deposition through a pre-patterned shadow mask (Nano 36 Kurt J. Lesker) at a base pressure of 10^{-6} mbar. The active area of each device was 3.14 mm^2.

LED Performance Characterization: All the devices were fabricated and characterized in ambient air conditions. Current density–voltage (*J–V*) characteristics were recorded using a computer-controlled Keithley 2400 source measurement unit. EQE of the devices was calculated by detecting the radiance from the device with a calibrated Newport 918D-IR-OD3 germanium photodetector connected to Newport 1918-C power meter in

parallel to the *J–V* measurements and further confirmed with a Newport 818 IG InGaAs photodetector. Lambertian emission was assumed during radiance calculation. The thickness of the glass substrate was considered during the solid angle calculation. For half-ball lens attached devices, the lenses (NBK-7 from Edmund Optics) were attached to the glass side of the LED devices. Norland UV curing optical adhesive was used to attach the lens with the glass substrate. The emitted power of lens attached LEDs was measured with a calibrated integrating sphere (IS210C from Thorlab).

Photodiodes Preparation: The photodiodes were prepared on top of ITO coated glass. ZnO layer was formed on top of ITO using already prepared ZnO NCs in chloroform (40 mg mL^{-1}) spun with 4000 rpm for 30 s and subsequently baked for 30 min on top of hot plate at 250 °C. The active layer was prepared with 0.79 eV excitonic peak based QDs treated with ZnI_2/MPA based mixed ligands. The active layer thickness was adjusted ≈300 nm. Finally, a 30 nm hole transporting layer was formed with 1.75 eV excitonic peak based QDs treated with EDT with aforementioned procedure. Thermally evaporated Au with active area of 3.14 mm^2 was used as the top electrodes.

Photodiode Characterizations: Current density–voltage (*J–V*) characteristics were performed with Keithley 2400 source measurement unit. A supercontinuum laser (NKT Photonics) with varying intensity was used as the light source ($\lambda = 1560$ nm) for light response measurements. The EQE of the device was measured using an in-house built integrated system. A chopped monochromatic illumination was used as the light source (chopping frequency 220 Hz). The source wavelength was scanned over 350 to 1700 nm range. The device photocurrent response of the chopped signal was measured using a Stanford Research system lock-in amplifier (SR830). A Stanford Research system low noise current preamplifier (SR570) was used in between the sample and the lock-in-amplifier to amplify the signal.

Modulation Measurements and Integrated Device Characterizations: To characterize the modulation bandwidth, the LEDs were driven with a DC power source connected with a function generator through bias-tee. The frequency of the signal was varied according to the experimental needs. The sample response was measured with an InGaAs avalanche photodetector (APD430C/M from Thorlab). The frequency modulation of the integrated devices was measured following the aforementioned method using PbS QD photodiode as signal receiver.

Photoluminescence and Electroluminescence Measurements: Photoluminescence (PL) and quantum yield (PLQY) measurements were performed utilizing a Horiba Jobin Yvon iHR550 Fluorolog system coupled with a Hamamatsu RS5509-73 liquid-nitrogen cooled photomultiplier tube and a calibrated Spectralon-coated Quanta-phi integrating sphere. A Vortran Stradus 637 nm continuous wave laser was used as the excitation source for all the steady state measurements. The PL spectra were corrected taking into account the system response function. The detail of the PLQY measurements was described elaborately in the authors' previous report.[16] Electroluminescence spectra were collected using an ANDOR InGaAs array CCD camera. The voltage bias to the device for electroluminescence measurement was applied with a Keithley 2400 source meter. For imaging surface of the devices, a SWIR lens was attached to NIT-WiDy-SenS-320V-ST InGaAs camera (Iberoptics Sistemas Ópticos), where the pictures and videos were recorded ≈20 cm away from the sample surface.

Supporting Information

Supporting Information is available from the Wiley Online Library or from the author.

Acknowledgements

G.K. acknowledges financial support from the European Research Council (ERC) under the European Union's Horizon 2020 research and innovation programme (grant agreement no. 725165), the State Research Agency (AEI)/PID2020-112591RB-I00/10.13039/501100011033 and PDC2021-120733-I00 funded by MCIN/AEI/10.13039/501100011033 by the "European Union Next Generation EU/PRTR. Additionally, this project has received funding from the Spanish State Research Agency, through the CEX2019-000910-S [MCIN/AEI/10.13039/501100011033], the CERCA Programme/Generalitat de Catalunya and Fundació Mir-Puig. N.T. acknowledges the funding received from the European Union's Horizon 2020 research and innovation programme under the Marie Skłodowska-Curie grant agreement No. 754558.

Conflict of Interest

The authors declare no conflict of interest.

Author Contributions

G.K. co-developed the concept designed the experiments and directed the study. S.P. co-developed the concept, fabricated, and characterized the devices, and analyzed the data. M.D. synthesized the QDs. B.K. helped in photodiode characterizations. N.T. has performed the optical simulations and captured the photo/video of LED emission with infrared camera. S.P. and G.K. wrote the manuscript with input from co-authors.

Data Availability Statement

The data that support the findings of this study are available from the corresponding author upon reasonable request.

Keywords

colloidal quantum dots, free-space optical communications, infrared light emitting diodes, LiFi

Received: March 4, 2022
Revised: April 5, 2022
Published online: May 4, 2022

[1] F. P. García de Arquer, D. V. Talapin, V. I. Klimov, Y. Arakawa, M. Bayer, E. H. Sargent, *Science* **2021**, *373*, eaaz8541.
[2] J. Huang, J. Lee, J. Vollbrecht, V. V. Brus, A. L. Dixon, D. X. Cao, Z. Zhu, Z. Du, H. Wang, K. Cho, G. C. Bazan, T. Nguyen, *Adv. Mater.* **2020**, *32*, 1906027.
[3] X. Tang, M. M. Ackerman, P. Guyot-Sionnest, *Laser Photonics Rev.* **2019**, *13*, 1900165.
[4] S. Yakunin, B. M. Benin, Y. Shynkarenko, O. Nazarenko, M. I. Bodnarchuk, D. N. Dirin, C. Hofer, S. Cattaneo, M. V. Kovalenko, *Nat. Mater.* **2019**, *18*, 846.
[5] L. Pérez, Í. Rodríguez, N. Rodríguez, R. Usamentiaga, D. F. García, *Sensors* **2016**, *16*, 335.
[6] S. J. Sweeney, A. F. Phillips, A. R. Adams, E. P. O'Reilly, P. J. A. Thijs, *IEEE Photonics Technol. Lett.* **1998**, *10*, 1076.
[7] C. Bao, W. Xu, J. Yang, S. Bai, P. Teng, Y. Yang, J. Wang, N. Zhao, W. Zhang, W. Huang, F. Gao, *Nat. Electron.* **2020**, *3*, 156.
[8] K. Yoshida, P. P. Manousiadis, R. Bian, Z. Chen, C. Murawski, M. C. Gather, H. Haas, G. A. Turnbull, I. D. W. Samuel, *Nat. Commun.* **2020**, *11*, 1171.
[9] A. Ren, H. Wang, W. Zhang, J. Wu, Z. Wang, R. V. Penty, I. H. White, *Nat. Electron.* **2021**, *4*, 559.
[10] M. Liu, N. Yazdani, M. Yarema, M. Jansen, V. Wood, E. H. Sargent, *Nat. Electron.* **2021**, *4*, 548.
[11] A. P. Litvin, I. V. Martynenko, F. Purcell-Milton, A. V. Baranov, A. V. Fedorov, Y. K. Gun'ko, *J. Mater. Chem. A* **2017**, *5*, 13252.

[12] X. Dai, Z. Zhang, Y. Jin, Y. Niu, H. Cao, X. Liang, L. Chen, J. Wang, X. Peng, *Nature* **2014**, *515*, 96.
[13] Y.-H. Won, O. Cho, T. Kim, D.-Y. Chung, T. Kim, H. Chung, H. Jang, J. Lee, D. Kim, E. Jang, *Nature* **2019**, *575*, 634.
[14] H. Shen, Q. Gao, Y. Zhang, Y. Lin, Q. Lin, Z. Li, L. Chen, Z. Zeng, X. Li, Y. Jia, S. Wang, Z. Du, L. S. Li, Z. Zhang, *Nat. Photonics* **2019**, *13*, 192.
[15] Q. Su, H. Zhang, S. Chen, *npj Flexible Electron.* **2021**, *5*, 8.
[16] S. Pradhan, F. Di Stasio, Y. Bi, S. Gupta, S. Christodoulou, A. Stavrinadis, G. Konstantatos, *Nat. Nanotechnol.* **2019**, *14*, 72.
[17] S. Pradhan, M. Dalmases, A. Baspinar, G. Konstantatos, *Adv. Funct. Mater.* **2020**, *30*, 2004445.
[18] M. Vasilopoulou, H. P. Kim, B. S. Kim, M. Papadakis, A. E. Ximim Gavim, A. G. Macedo, W. Jose da Silva, F. K. Schneider, M. A. Mat Teridi, A. G. Coutsolelos, A. R. bin Mohd Yusoff, *Nat. Photonics* **2020**, *14*, 50.
[19] X. Gong, Z. Yang, G. Walters, R. Comin, Z. Ning, E. Beauregard, V. Adinolfi, O. Voznyy, E. H. Sargent, *Nat. Photonics* **2016**, *10*, 253.
[20] L. Gao, L. N. Quan, F. P. García de Arquer, Y. Zhao, R. Munir, A. Proppe, R. Quintero-Bermudez, C. Zou, Z. Yang, M. I. Saidaminov, O. Voznyy, S. Kinge, Z. Lu, S. O. Kelley, A. Amassian, J. Tang, E. H. Sargent, *Nat. Photonics* **2020**, *14*, 227.
[21] S. Pradhan, M. Dalmases, G. Konstantatos, *Adv. Mater.* **2020**, *32*, 2003830.
[22] K. Tuong Ly, R.-W. Chen-Cheng, H.-W. Lin, Y.-J. Shiau, S.-H. Liu, P.-T. Chou, C.-S. Tsao, Y.-C. Huang, Y. Chi, *Nat. Photonics* **2017**, *11*, 63.
[23] R. Yu, F. Yin, X. Huang, W. Ji, *J. Mater. Chem. C* **2017**, *5*, 6682.
[24] Q. Zhang, X. Gu, Z. Chen, J. Jiang, Z. Zhang, J. Wei, F. Li, X. Jin, Y. Song, Q. Li, *Opt. Express* **2017**, *25*, 17683.
[25] H.-Y. Lan, I.-C. Tseng, H.-Y. Kao, Y.-H. Lin, G.-R. Lin, C.-H. Wu, *IEEE J. Quantum Electron.* **2018**, *54*, 1.
[26] M. Vafaie, J. Z. Fan, A. M. Najarian, O. Ouellette, L. K. Sagar, K. Bertens, B. Sun, F. P. G. de Arquer, E. H. Sargent, *Matter* **2021**, *4*, 1042.
[27] J. W. Lee, D. Y. Kim, S. Baek, H. Yu, F. So, *Small* **2016**, *12*, 1328.
[28] S. Pradhan, A. Stavrinadis, S. Gupta, Y. Bi, F. Di Stasio, G. Konstantatos, *Small* **2017**, *13*, 1700598.

ADVANCED FUNCTIONAL MATERIALS
www.afm-journal.de

Ultra-Thin Infrared Optical Gain Medium and Optically-Pumped Stimulated Emission in PbS Colloidal Quantum Dot LEDs

*Nima Taghipour, Ibrahim Tanriover, Mariona Dalmases, Guy L. Whitworth, Christina Graham, Avijit Saha, Onur Özdemir, Biswajit Kundu, Valerio Pruneri, Koray Aydin, and Gerasimos Konstantatos**

Colloidal semiconductor quantum dots (QDs) can be considered a promising material platform for solution-processed laser diodes. However, due to some fundamental challenges, the realization of electrically pumped lasing based on QDs remains unresolved. Here, a binary blend of QDs and ZnO nanocrystals is employed, which serve as nano-sized scatterers to facilitate waveguide gain in ultra-thin films. By carefully engineering the electric field in these films, an infrared amplified spontaneous emission in a record thin colloidal gain medium is observed, with a thickness of 16 nm, at a wavelength of 1675 nm. Employing these binary blends as a gain medium, an optically pumped infrared stimulated emission in a full-stacked light-emitting diode (LED) device is demonstrated. The functional LED device, which comprises a single layer of graphene as an anode electrode, shows strong electroluminescence under electrical injection. This study suggests a promising device for realizing infrared QD-based laser diodes.

1. Introduction

Short-wave infrared lasers have a broad range of applications, including fiber optic telecommunication,[1,2] complementary metal-oxide-semiconductor (CMOS) photonics,[3,4] and eye-safe light detection and ranging (LiDAR) applications.[5,6] The existing technologies for short-wave infrared lasers are based on epitaxially grown III–V semiconductors[7–9] and Erbium-doped optical fibers.[10,11] The aforementioned technologies can neither be integrated into silicon technology nor do they cover the full optical telecommunication window. Colloidal semiconductor quantum dots (QDs) emerged as an alternative and promising gain medium thanks to their favorable optical and electrical properties, including spectral tunability,[12,13] compatibility with diverse matrices,[14,15] and high photoluminescence quantum efficiency.[13,16] Most recently, tunable room-temperature, near-infrared stimulated emission and lasing have been successfully demonstrated using PbS QDs as a gain medium.[17–19] However, stimulated emission under electrical or continuous-wave pumping using PbS-based QDs has yet to be demonstrated. Due to the multiexcitonic nature of light amplification in PbS, it is essential to suppress undesired non-radiative Auger recombination, whereby the energy of an exciton recombination is delivered to a third carrier.[20] In order to eventually realize electrically-driven infrared stimulated emission and lasing in QDs, the following challenges should be addressed: 1) to demonstrate optical gain in a full-light-emitting diode (LED) device stack, including conductive layers and contacts, 2) to obtain net gain and stimulated emission in ultra-thin film gain medium in order to facilitate efficient electrical injection, and 3) to increase the robustness of the device upon high current density needed to achieve population inversion.[21,22]

In the present study, we address the first two challenges and demonstrate a functional infrared EL device in an all colloidal LED device, which exhibits stimulated emission characteristics under optical pumping. In previous studies, we have demonstrated that by blending ZnO nanocrystals (NCs) with PbS QDs the electronic properties of the gain material can be improved to achieve low-threshold amplified spontaneous emission (ASE).[17] Herein, we demonstrate an electroluminescence (EL) device architecture with a PbS/ZnO blend acting as the thin film active media of an LED device. Additional to improving ASE performance, the ZnO NCs are also observed to form nanoclusters that act as scattering sites that facilitate ASE propagation below the waveguide

N. Taghipour, M. Dalmases, G. L. Whitworth, C. Graham, A. Saha, O. Özdemir, B. Kundu, V. Pruneri, G. Konstantatos
ICFO
Institut de Ciències Fotòniques
The Barcelona Institute of Science and Technology
Barcelona 08860, Spain
E-mail: gerasimos.konstantatos@icfo.eu
I. Tanriover, K. Aydin
Department of Electrical and Computer Engineering
Northwestern University
Evanston, IL 60208, USA
V. Pruneri, G. Konstantatos
ICREA
Institució Catalana de Recerca i Estudis Avançats
Barcelona 08010, Spain

The ORCID identification number(s) for the author(s) of this article can be found under https://doi.org/10.1002/adfm.202200832.

DOI: 10.1002/adfm.202200832

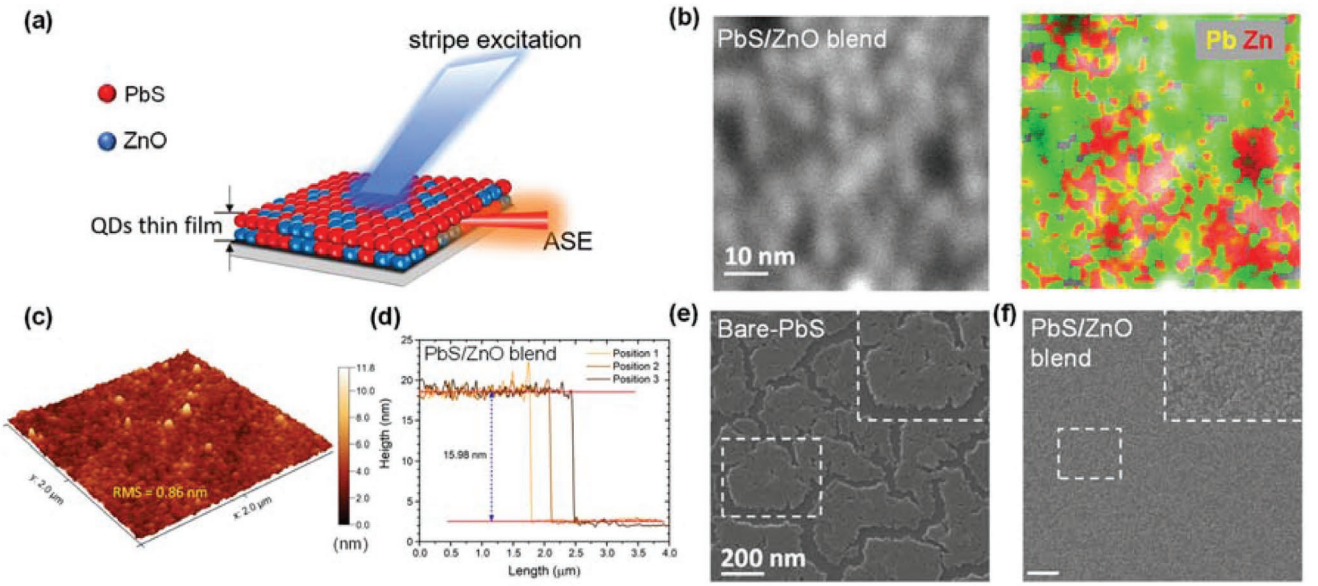

Figure 1. Characterization of bare-PbS and PbS/ZnO blend samples. a) Schematic illustration of ASE measurement. b) STEM-EDS elemental mapping PbS/ZnO blend, where Pb:ZnO is 68:32%. c) AFM image showing morphology of PbS/ZnO blend thin film having a thickness of 16 nm. d) height profile of PbS/ZnO blend thin film. SEM image of a single layer of e) bare-PbS and f) PbS/ZnO blend on silicon substrate. Inset shows the zoom-in image of the indicated region.

cut-off thickness. By carefully adjusting the loading amount of ZnO in PbS/ZnO blend, we are able to attain stimulated emission at a record subwavelength gain medium thickness of 16 nm (i.e., $\lambda/100$). Importantly, stimulated emission is also realized in a complete LED device structure including an anode electrode that is made of a single layer of graphene. It is noteworthy that although lasing action has been previously shown in LED-like structure in the visible,[22] none of those devices included the anode electrode which is crucial for a real EL device, and the lasing emission was observed to disappear in the vicinity of a conventional metal electrode, due to optical losses.[22]

2. Results and Discussion

The standard architecture for demonstrating ASE in a thin film is a slab waveguide where the stimulated emission is confined in a high refractive index gain medium. A homogenous thin film asymmetric waveguide has a minimum thickness for which it can still support a guiding mode for a given wavelength. We posited that the presence of low refractive index ZnO NCs blended with PbS QDs active medium at the nanoscale would allow us to overcome this critical thickness threshold by assisted scattering. **Figure 1**a illustrates the configuration for ASE measurements of the thin films, showing how spontaneous emission is propagated in-plane, and then amplified along the pump stripe. The resultant ASE signal is then collected at the edge of the film, perpendicular to the excitation beam. Using our proposed architecture, we would be able to achieve ASE in the thicknesses that are required for high current injection in LED structures. Using scanning transmission electron microscopy (STEM)-energy dispersive X-ray spectrometry (EDS) elemental mapping, shown in Figure 1b superposed on a dark field image, the ratio of Pb to Zn was measured to be 68:32%. From transmission electron microscopy (TEM) images, we extracted the diameter of PbS QDs and ZnO NCs as ≈5.8 and 6 nm respectively, and as shown in Figure 1b, ZnO NCs tended to form nano-clusters. We employed atomic force microscopy (AFM) to assess the thickness and surface morphology of our samples, the results of which are illustrated in Figure 1c,d, where the thickness of the film is measured to be ≈16 nm with an r.m.s. value of 0.86 nm. The AFM images of thin films with different thickness are shown in Figures S1 and S2 (Supporting Information). Furthermore, the scanning electron microscopy (SEM) images of bare-PbS and PbS/ZnO blends are displayed in Figure 1e,f, respectively. As can be seen, introducing ZnO NCs improved the uniformity of the thin film formation which can be attributed to better nucleation of PbS QDs during the spin-coating process.[23] This results in a smooth thin film gain medium with the PbS/ZnO blend, in which the surface coverage reaches near unity for a single layer deposition, with no noticeable cracks or voids.

To investigate the optical gain performance of our devices, we spin-coated the PbS/ZnO blend, with a ratio of 7:3, on a glass substrate. We controlled the thickness of the samples via repeated spin-coating and ligand exchange procedures (see Experimental Section). ASE spectra from a sample as thin as ≈16 nm $\left(<\frac{\lambda}{100}\right)$ are plotted in **Figure 2**a as a function of pump fluence. Figure 2b depicts the integrated intensity of the ASE spectra against pump fluence along with the corresponding full-width at half-maximum (FWHM) of each spectrum. The photoluminescence (PL) intensity increases linearly with pump intensity at low fluences and then exhibits a super-linear behavior above the threshold of 2.9 mJ cm^{-2}, a clear signature of light amplification above the ASE threshold,

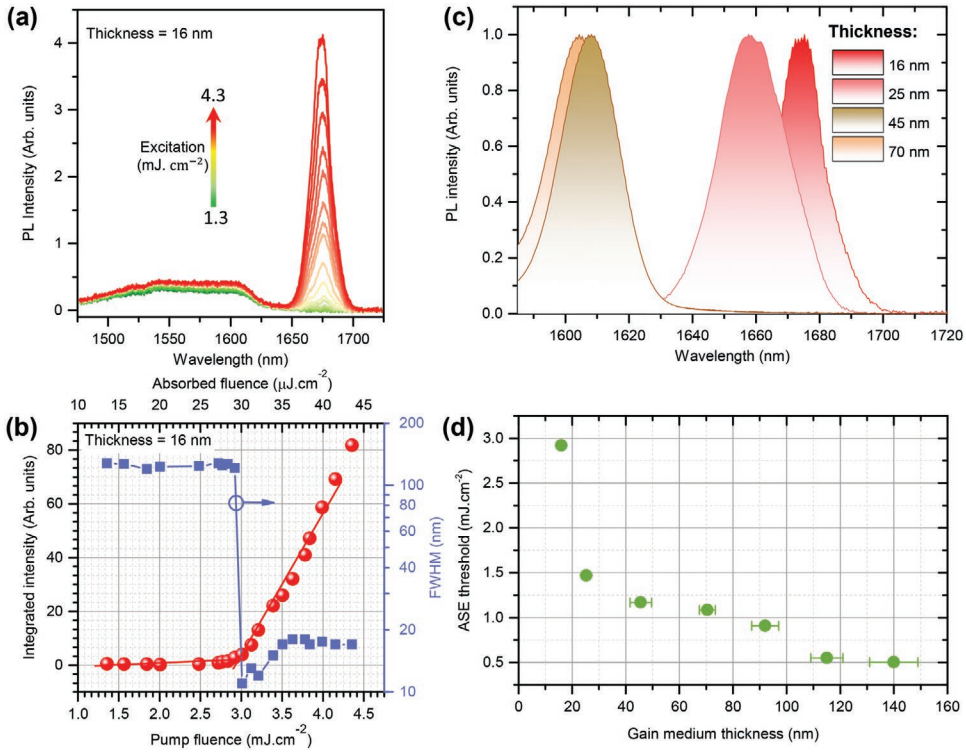

Figure 2. ASE characterization of PbS/ZnO blend sample. a) ASE spectra from a blend of PbS/ZnO (30%), having a thickness of 16 nm, as a function of fluence. b) Normalized integrated intensity of the spectra as a function of pump fluence, with corresponding FWHM. c) Emission spectra of PbS/ZnO (30%) blend sample with different thicknesses of 16, 25, 45 and 70 nm. d) Evolution of ASE threshold with increasing thickness of thin films.

the FWHM of the spectra drastically drops from ≈125 nm to ≈17 nm. To the best of our knowledge, this is the thinnest attained thickness for ASE using a colloidal gain medium with a thickness of ≈16 nm and an ASE peak wavelength of ≈1675 nm. Note that 16 nm is below the theoretical waveguide cut-off thickness or a homogenous medium at this wavelength (56 nm).

As discussed above, for electrically pumped QD lasers, it is essential to achieve an optical gain in ultra-thin films in order to facilitate charge injection into the active medium for achieving population inversion;[21,22] as thin active media results in a balanced carrier supply to the QDs.[16] Furthermore, as shown in Figure 2c, by increasing the thickness of the PbS/ZnO films, the ASE peak is gradually blue-shifted. For instance, the ASE peak for a 70 nm thick film appears at ≈1604 nm. This blue-shifting of the ASE peak can be attributed to the increased scattering in thicker films. The ASE thresholds for films with varying thicknesses are summarized in Figure 2d, decreasing from 2.9 to 0.5 mJ cm^{-2} having a film thicknesses of 16 and 140 nm respectively. We measured net optical gain (G) and waveguide loss coefficients (α) for bare-PbS and PbS/ZnO blend with varying thickness via the variable stripe length (VSL) and moving-edge loss methods (see Supplementary Note 1). These results are depicted in Figures S3 and S4 (Supporting Information). At similar pump fluences, G is lower in the PbS/ZnO blend compared to bare-PbS films due to the reduced amount of gain material in the blend. Similarly, thanks to the reduction of re-absorption losses in blends, α dropped to 9 cm^{-1} in PbS/ZnO blend sample within a thickness of ≈25 nm, while it is 23 cm^{-1} for bare-PbS samples having a thickness of ≈110 nm. (Figure S5, Supporting Information).

To gain further insights into our experimental ASE observation of the QD ultra-thin films, we employed a full-field electromagnetic numerical model. In principle, our structure can be modeled as an asymmetric slab waveguide, in which the gain medium is sandwiched between semi-infinite fused silica and air layers. **Figure 3**a,b depict the asymmetric planar waveguide enabling electromagnetic modes to propagate along the waveguide, while fundamental transverse electric field (TE) and transverse magnetic field (TM) modes require a minimum thickness to be confined inside the active region. The critical thicknesses for TE and TM can be calculated from the following expressions:[24]

$$t_{TE} = \frac{\lambda}{2\pi\sqrt{n_2^2 - n_3^2}}\left[m\pi + \arctan\left(\sqrt{\frac{n_3^2 - n_1^2}{n_2^2 - n_3^2}}\right)\right] \quad (1)$$

$$t_{TM} = \frac{\lambda}{2\pi\sqrt{n_2^2 - n_3^2}}\left[m\pi + \arctan\left(\frac{n_2^2}{n_1^2}\left(\sqrt{\frac{n_3^2 - n_1^2}{n_2^2 - n_3^2}}\right)\right)\right] \quad (2)$$

Using Equation 1, the waveguide cut-off thickness is plotted against wavelength in Figure 3c for the fundamental TE and TM modes (m = 0). For λ = 1675 nm, the minimum thicknesses for propagation of TE_0 and TM_0 in PbS solid film are 56 and 158 nm, respectively. However, for PbS/ZnO blends, t_{TE_0}

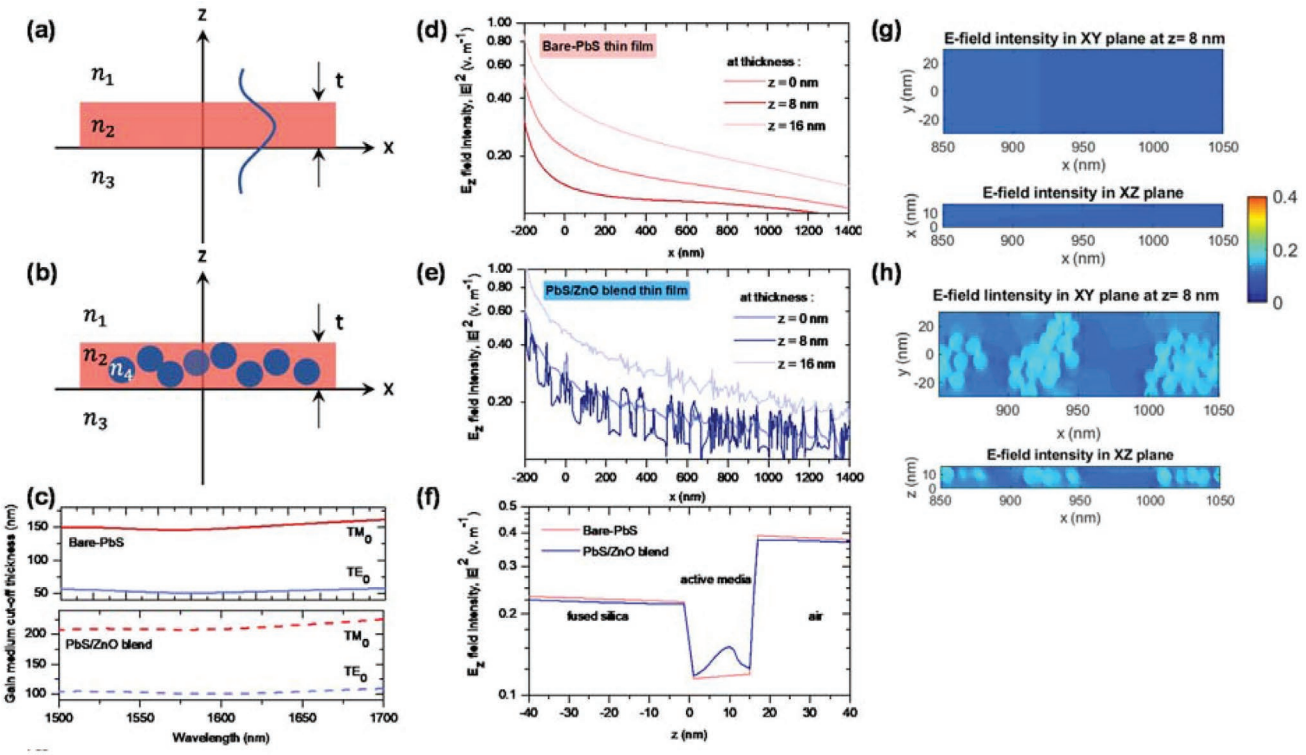

Figure 3. Full numerical electromagnetic model. a,b) Schematic drawing of an asymmetric slab-waveguide made of bare-PbS (a) and a PbS/ZnO blend (b). c) Calculated gain medium cut-off thickness for supporting fundamental TE and TM in bare-PbS (top panel) and PbS/ZnO blend (bottom panel) devices as a function of wavelength. d,e) Electric field intensity ($|E|^2$) variation along the lateral side of samples at different heights for bare-PbS (d) and PbS/ZnO blend (e). f) Electric field intensity ($|E|^2$) variation along vertical direction of the samples for bare-PbS and PbS/ZnO blend. Note, the thin film extends from 0 to 16 nm. g,h) Electric field distribution along *xy*-plane and *xz*-plane for bare-PbS (g) and PbS/ZnO (h). Note, all E-fields are recorded at ASE wavelength of 1675 nm.

and t_{TM_0} are 106 and 220 nm. Note, we extracted the refractive indices of films using spectroscopic ellipsometry (Figure S7, Supporting Information). In PbS/ZnO blends, the onset experimental thickness for observing ASE signal in thin film configuration is ≈16 nm. Therefore, the mode confinement in our architecture does not obey the rules of a conventional slab waveguide. We modeled our thin film devices using an FDTD solver (see Experimental Section). In the case of bare-PbS, the thin film of QDs is approximated as a homogenous medium, while for PbS/ZnO blend, the ZnO NCs are located inside the homogenous medium of PbS thin film as shown in Figure 3b. Note, the loading of ZnO NCs is 30% of the whole volume, which was extracted from STEM-EDS mapping images (see Figure 1b). In our model, the semi-infinite SiO_2 substrate extends from $z = -\infty$ to $z = 0$, the active medium spreads from $z = 0$ to $z = 16$ nm, and above the structure is air. Figure 3d plots the electric field (E-field) intensity distribution in *z*-direction ($|E_z|^2$) along the lateral direction of the sample at different *z* positions within a bare-PbS film, where the majority of E-field propagates in the substrate and air. However, in the PbS/ZnO blended thin film, the E-field is enhanced at the position of ZnO nano-clusters owing to the strong scattering of light as can be seen in Figure 3e (dark blue line, $z = 8$ nm which is the middle of the gain medium). Although similar behavior is also observed at the interfaces, the intensity of scattering is significantly larger at the center of the gain medium ($z = 8$ nm). At approximately one wavelength distance from the source injection, the E-field intensity is integrated over the *xy*-plane at corresponding heights (*z*'s). Another notable observation is the emergence of a propagation mode in PbS/ZnO blend sample, where the E-field intensity exhibits a maximum in the gain medium, while there is no variation of E-field intensity in the bare-PbS case as depicted in Figure 3f. Figure 3g displays the E-field distribution over the *xy*-plane (in the middle of the gain medium, $z = 8$ nm) and *xz*-plane for bare-PbS thin film, where there is no abrupt change in the E-field intensity. However, as shown in Figure 3h, the E-field intensity is significantly enhanced at the surface of ZnO NCs where due to the cluster formation of ZnO NCs, the electromagnetic wave propagates between these nano-clusters. It is worth mentioning that the scattering from ZnO nano-clusters allowed us to observe random lasing behavior in our thin film device with a thickness of 68 ± 6 nm on a glass substrate, which is plotted in Figure S6 (Supporting Information), showing a narrow lasing mode, that outcompetes other modes, within a linewidth of 4 nm (1.86 meV) at ≈1630 nm, and exhibits a lasing threshold of 4.60 mJ cm^{-2}.

Finally, we fabricated a complete LED device stack comprising of engineered indium tin oxide (E-ITO) as a cathode electrode, a layer of ZnO NCs acting as electron transport layer (ETL), the PbS/ZnO blend as active medium (0.8 eV bandgap PbS QDs), a hole transport layer (HTL) made from large-bandgap PbS QDs

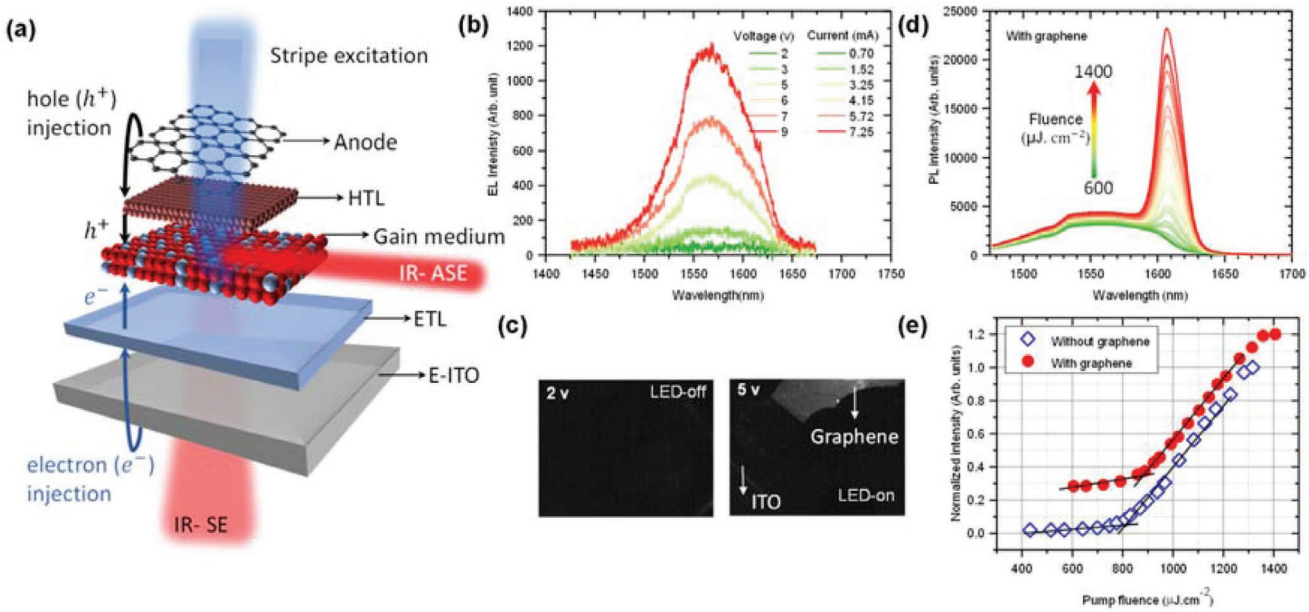

Figure 4. A full-LED device stack as both optically-pumped infrared-ASE and electrically-driven infrared-SE device. a) Schematic illustration of a complete LED structure. b) SE spectra of electrically excited LED as a function of bias voltages. c) Infrared images taken from the surface of the LED structure under 2 V and 5 V where LED is -off and -on, correspondingly, with the graphene layer indicated. d) ASE spectra as a function of excitation fluence under femtosecond laser pumping in full-LED device, where the anode layer is made of a single layer of graphene. e) Normalized integrated intensity of ASE spectra against pump fluence for the devices with and without anode electrode.

(1.77 eV), and a single layer of graphene serving as the anode electrode. We engineered the optical constant of as-deposited ITO, to achieve a transmission of above 85% across our operating wavelength window (Figure S8, Supporting Information), allowing us to observe stimulated emission on E-ITO substrates. Un-engineered ITO, in contrast, has transmission values down to as low as 60%, adding to much optical loss for an ASE signal to propagate along the sample. Note, the thickness of the ETL, gain medium and HTL are around 40, 80 and 20 nm, respectively. **Figure 4**a is a schematic illustration of the tested LED structure exhibiting electrically injected infrared SE, as well as showing infrared ASE under optical laser excitation. The bias-dependent LED device exhibits infrared SE at a wavelength of 1563 nm as shown in Figure 4b. Moreover, the infrared images of the LED device taken from the surface of the structure are depicted in Figure 4c. At 2 V the LED is in the off-state, while at 5 V it is in the on-state. By applying sufficient bias to the electrodes, bright infrared emission is clearly visible from the graphene-covered portion of the device. By pumping our LED device under stripe excitation of a femtosecond laser (fs-laser), we observed an infrared stimulated emission peak at ≈1607 nm as depicted in Figure 4d. The corresponding integrated intensity of ASE spectra versus excitation fluence is shown in Figure 4e for both with and without top electrode (i.e., graphene layer). The ASE threshold for the case of without graphene is ≈820 μJ cm^{-2} which then increases slightly to 840 μJ cm^{-2} when the graphene was placed on top. This can be attributed to the graphene transfer procedure (see Experimental Section). It is worth mentioning that our proposed PbS/ZnO blend even allows us to achieve a net optical gain in a full LED stack device.

3. Conclusion

In conclusion, we report near-infrared stimulated emission in a record thin colloidal gain medium. Our novel PbS/ZnO blends strongly interact with photons due to nano-cluster scatterers, resulting in propagation of generated stimulated emission along the surface of the devices below the fundamental cut-off thickness for an asymmetric slab waveguide. Moreover, we show ASE in full-stack LED structure made of QDs as the gain medium under optical excitation. In our LED device, we employed a single layer of graphene as an anode electrode instead of the conventional metals which results in quenching of ASE mode in the gain media. Our results will pave the way to realize a true electrically-driven laser made of QDs as the gain medium.

4. Experimental Section

PbS QDs Synthesis: 0.8 eV excitonic peak PbS QDs were synthesized under inert atmosphere by hot injection method. Briefly, 0.446 g PbO, 50 mL 1-octadecene (ODE) and 3.8 mL oleic acid were heated at 100 °C under vacuum for 1 h to form the lead precursor (lead oleate). Once under argon, a solution of 65 μL hexamethyldisilathiane (HMS) in 3 mL ODE was quickly injected. After 6 min of reaction, a second solution of 75 μL HMS in 9 mL ODE was injected dropwise. Subsequently, the solution was cooled down naturally to room temperature. PbS QDs were precipitated with the addition of a mixture of acetone/ethanol and re-dispersed in anhydrous toluene. This purification process was repeated two more times. Finally, the concentration of PbS QDs was adjusted to 30 mg mL^{-1}. The last step of purification and the adjustment of the concentration were done inside the glovebox in order to avoid oxidation.

1.77 eV excitonic peak PbS QDs were synthesized following the standard recipe. 0.446 g PbO, 18 mL ODE and 1.6 mL oleic acid were degassed for 1 h under vacuum at 100 °C. Once under argon, the temperature was set at 80 °C and 210 µL HMS in 5 mL ODE was quickly injected. After 25 s the reaction was quenched with cold acetone and QDs were collected by precipitation. The PbS QDs were purified by dispersion/precipitation with anhydrous toluene/acetone three times. Finally, the concentration was adjusted to 30 mg mL^{-1} and the sample was stored at low temperature to avoid Ostwald ripening.

ZnO NCs Synthesis: ZnO NCs were synthesized based on the method shown previously.[25] Briefly, 2.95 g of Zinc acetate dihydrate was dissolved in 125 mL of methanol under continuous stirring, while the temperature of the heater was set at 60 °C. Separately, 1.48 g of KOH was dissolved in 65 mL of methanol. When the temperature of Zinc acetate dihydrate solution reached to ≈60 °C, the solution of KOH was slowly added to it in roughly 4 min, and the reaction was left for 2.5 h. After finishing the reaction, the heater was removed, and the solution was slowly cooled down to room temperature under continuous stirring. Then, the synthesized ZnO NCs solution was centrifuged at 3500 r.p.m. for 5 min. The supernatant was removed and the remaining NCs were dispersed in methanol, the centrifuge step was repeated three times. Finally, the ZnO NCs were dispersed in a solution of 5% (v/v) butylamine in toluene for making the binary blend solutions, and in 2% (v/v) butylamine in chloroform for formation of the electron transport layer.

Active Layer Deposition: The active layer was deposited on the desired substrate using spin coating method. First, 50 µL of QDs solution was poured on the pre-cleaned substrate, spin coating started after 5 s, with a spin speed of 2500 r.p.m. for 15 s. The then formed surface of PbS QDs was covered with a prepared inorganic ligand solution of ZnI_2/MPA (mixing of 8 mg ml^{-1} zinc iodide (ZnI_2) in methanol and 0.015% (v/v) 3-mercaptopropionic acid (MPA) in methanol). After 7 s of ligand exchange time, the spin coating was restarted at a spin speed of 2500 r.p.m. for 40 s. During this time the excess organics ligands were cleaned with a few drops of methanol. The above-mentioned steps were repeated until reaching the desired thickness. Before mixing, the ZnO NCs were prepared in separate vials with the same concentration as PbS QDs. For the PbS/ZnO binary blend solution, the PbS QDs solution was mixed with the ZnO solution at 30% loading content. The film thicknesses were measured via an AFM and a profilometer.

ASE Characterization: The devices were optically pumped by a femtosecond Yt:YAG ORAGAMI laser (NKT Photonics) operating at 1030 nm within a pulse width of 300 fs at a repetition rate of 10 kHz. The excitation fluence was adjusted using a variable neutral density. The laser beam was focused as a stripe excitation on the sample using a cylindrical lens with a focal length of 20 cm. Using a lens with a focal length of 50 mm and a diameter of 2 inches, the ASE spectra were collected perpendicular to the excitation beam. Utilizing free-space optics, the collected ASE signal was coupled into Kymera 328i spectrograph (Oxford Instruments. Andor) equipped with a InGaAs camera through a 100 µm slit via a lens with $f = 20$ cm.

Lumerical FDTD Simulation: Commercial software, Ansys Lumerical Finite Difference Time Domain (FDTD), is used for full electromagnetic simulations. A thin (16 nm) PbS layer is placed on top of a semi-infinite SiO_2 substrate ($z \leq 0$). Clusters of spherical ZnO particles are randomly distributed inside the PbS layer. The fundamental mode is calculated and injected toward x direction by the built-in mode source. The fields are recorded by frequency-domain field and power monitors. Perfectly matched layers (PML) boundary conditions are used at $\pm x$ and $\pm z$ boundaries, and periodic boundary conditions are used at $\pm y$ boundaries.

Engineered-Indium Tin Oxide (E-ITO)-Coated Glass Substrate Preparation: The E-ITO is made by low-temperature annealing (LTA) of as-deposited ITO based on the method explained in our previous work.[26] ITO films of 100 nm were deposited by the University of Stuttgart on fused silica substrates via sputtering at room temperature. In the LTA process, the as-deposited ITO is annealed on a hotplate at 350 °C for 3 h, in the ambient atmosphere.

Graphene Layer Transfer: CVD-grown monolayer graphene on copper with polymethyl methacrylate (PMMA) on top (purchased from Graphenea S.A) was cut to match the sample dimensions. The copper was etched in an ammonium persulfate solution in deionized water (3 g ml^{-1}) for 3 h. The remaining PMMA/graphene sheet is further cleaned in deionized water and transferred onto the sample. The sample with the graphene/PMMA layer is dried overnight in vacuum. PMMA is removed with acetone and isopropanol to obtain the graphene layer on top of our devices.

LED Device Fabrication: The LED device was fabricated on a pre-cleaned E-ITO substrate. The electron transport layer was made of ZnO NCs by spin-casting ZnO NCs in chloroform at a spin speed of 4000 r.p.m. for 60 s. The active medium was spun on top of the ZnO layer as described in the active layer deposition section. The hole transport layer was formed using PbS QDs of smaller diameter which was treated by a solution of 0.02% ethanedithiol in acetonitrile. The graphene layer was transferred in a way mentioned above. To prevent from scratching the graphene layer, we deposited approximately 50 nm Au through a pre-patterned mask in thermal evaporator (Nano 36 Kurt J. Lesker).

Supporting Information

Supporting Information is available from the Wiley Online Library or from the author.

Acknowledgements

The authors acknowledge support from the State Research Agency (AEI)/PID2020-112591RB-I00/10.13039/501100011033 and PDC2021-120733-I00 funded by MCIN/AEI/10.13039/501100011033 by the European Union Next GenerationEU/PRTR. Additionally, this project has received funding from the Spanish State Research Agency, through the CEX2019-000910-S [MCIN/AEI/10.13039/501100011033], the CERCA Programme/Generalitat de Catalunya and Fundació Mir-Puig. This project has received funding from the European Union's Horizon 2020 research and innovation programme under the Marie Skłodowska-Curie grant agreement numbers 754558 and 713729. V.P. acknowledges financial support from the Spanish Ministry of Economy and Competitiveness through the "Severo Ochoa" Programme for Centres of Excellence in R&D (CEX2019-000910-S) and project TUNA-SURF (PID2019-106892RB-I00), Fundació Mir-Puig, and from Generalitat de Catalunya through the CERCA program, from AGAUR 2017 SGR 1634. K.A. acknowledges support from the Air Force Office of Scientific Research under Award Number FA9550-17-1-0348.

Conflict of Interest

The authors declare no conflict of interest.

Author Contributions

G.K. co-conceived the idea and supervised the study at all stages. N.T. co-conceived the concept and fabricated, characterized the laser and LED devices, and analyzed data. N.T. and G.K. designed the experiments. I.T., N.T., and K.A. performed FDTD simulations. M.D. synthesized PbS QDs. G.L.W. contributed to discussions and ASE measurements. V.P. developed and G.C. provided E-ITO-coated glass substrates. A.S. carried out TEM imaging. N.T. conducted SEM characterizations. N.T. and O.Ö. conducted graphene layer transfer. B.K. performed AFM measurements. N.T. and G.K. wrote the manuscript with contributions from all authors.

Data Availability Statement

The data that support the findings of this study are available from the corresponding author upon reasonable request.

Keywords

amplified spontaneous emissions, colloidal quantum dots, diode lasers, graphene, light emitting diodes, optical gain

Received: January 20, 2022
Revised: March 9, 2022
Published online: April 8, 2022

[1] A. Castillo-Guzman, J. E. Antonio-Lopez, R. Selvas-Aguilar, D. A. May-Arrioja, J. Estudillo-Ayala, *Opt. Express* **2010**, *18*, 591.
[2] S. A. Babin, S. I. Kablukov, A. A. Vlasov, *Laser Phys.* **2007**, *17*, 1323.
[3] E. Marchena, T. Creazzo, S. B. Krasulick, P. K. L. Yu, D. Van Orden, J. Y. Spann, C. C. Blivin, J. M. Dallesasse, P. Varangis, R. J. Stone, A. Mizrahi, Optical Fiber Communication Conference 2013, OSA Technical Digest (Online).
[4] N. Li, D. Vermeulen, Z. Su, E. S. Magden, M. Xin, N. Singh, A. Ruocco, J. Notaros, C. V. Poulton, E. Timurdogan, C. Baiocco, M. R. Watts, *Opt. Express* **2018**, *26*, 16200.
[5] L. Cheng, S. Chen, X. Liu, H. Xu, Y. Wu, M. Li, Y. Chen, *Sensors* **2018**, *18*, 1641.
[6] M. Yoshida, M. De Zoysa, K. Ishizaki, W. Kunishi, T. Inoue, K. Izumi, R. Hatsuda, S. Noda, *J. Phys Photonics* **2021**, *3*, 022006.
[7] M. P. Mikhailova, K. D. Moiseev, Y. P. Yakovlev, *Semiconductors* **2019**, *53*, 273.
[8] Y. Wang, S. Chen, Y. Yu, L. Zhou, L. Liu, C. Yang, M. Liao, M. Tang, Z. Liu, J. Wu, W. Li, I. Ross, A. J. Seeds, H. Liu, S. Yu, *Optica* **2018**, *5*, 528.
[9] A. F. Phillips, S. J. Sweeney, A. R. Adams, P. J. A. Thijs, *IEEE J. Sel. Top. Quantum Electron.* **1999**, *5*, 401.
[10] M. E. Fermann, I. Hartl, *IEEE J. Sel. Top. Quantum Electron.* **2009**, *15*, 191.
[11] Y. Chang, L. Pei, T. Ning, J. Zheng, *Opt. Laser Technol.* **2019**, *124*, 105985.
[12] P. O. Anikeeva, J. E. Halpert, M. G. Bawendi, V. Bulović, *Nano Lett.* **2009**, *9*, 2532.
[13] I. Moreels, Y. Justo, B. De Geyter, K. Haustraete, J. C. Martins, Z. Hens, *ACS Nano* **2012**, *5*, 2004.
[14] M. V. Kovalenko, L. Manna, A. Cabot, Z. Hens, D. V. Talapin, C. R. Kagan, V. I. Klimov, A. L. Rogach, P. Reiss, D. J. Milliron, P. Guyot-Sionnnest, G. Konstantatos, W. J. Parak, T. Hyeon, B. A. Korgel, C. B. Murray, W. Heiss, *ACS Nano* **2015**, *9*, 1012.
[15] D. V. Talapin, J. S. Lee, M. V. Kovalenko, E. V. Shevchenko, *Chem. Rev.* **2010**, *110*, 389.
[16] S. Pradhan, F. Di Stasio, Y. Bi, S. Gupta, S. Christodoulou, A. Stavrinadis, G. Konstantatos, *Nat. Nanotechnol.* **2019**, *14*, 72.
[17] N. Taghipour, G. L. Whitworth, A. Othonos, M. Dalmases, S. Pradhan, Y. Wang, G. Kumar, G. Konstantatos, *Adv. Mater.* **2021**, *34*, 2107532.
[18] G. L. Withworth, M. Dalmases, N. Taghipour, G. Konstantatos, *Nat. Photonics* **2021**, *15*, 738.
[19] S. Christodoulou, I. Ramiro, A. Othonos, A. Figueroba, M. Dalmases, O. Özdemir, S. Pradhan, G. Itskos, G. Konstantatos, *Nano Lett.* **2020**, *20*, 5909.
[20] V. I. Klimov, A. A. Mikhailovsky, D. W. McBranch, C. A. Leatherdale, M. G. Bawendi, *Science* **2000**, *287*, 1011.
[21] H. Jung, N. Ahn, V. I. Klimov, *Nat. Photonics* **2021**, *15*, 643.
[22] J. Roh, Y. S. Park, J. Lim, V. I. Klimov, *Nat. Commun.* **2020**, *11*, 271.
[23] C. Li, Z. Zang, C. Han, Z. Hu, X. Tang, J. Du, Y. Leng, K. Sun, *Nano Energy* **2017**, *40*, 195.
[24] A. Yariv, P. Yeh, *Photonics: Optical Electronics in Modern Communications*, Oxford University Press, New York **2007**.
[25] A. K. Rath, F. Pelayo Garcia De Arquer, A. Stavrinadis, T. Lasanta, M. Bernechea, S. L. Diedenhofen, G. Konstantatos, *Adv. Mater.* **2014**, *26*, 4741.
[26] R. A. Maniyara, C. Graham, B. Paulillo, Y. Bi, Y. Chen, G. Herranz, D. E. Baker, P. Mazumder, G. Konstantatos, V. Pruneri, *APL Mater.* **2021**, *9*, https://doi.org/10.1063/5.0040864.

ADVANCED ELECTRONIC MATERIALS
www.advelectronicmat.de

Heterostructure from PbS Quantum Dot and Carbon Nanotube Inks for High-Efficiency Near-Infrared Light-Emitting Field-Effect Transistors

*Dmytro Bederak, Artem Shulga, Simon Kahmann, Wytse Talsma, Jokūbas Pelanskis, Dmitry N. Dirin, Maksym V. Kovalenko, and Maria A. Loi**

Light-emitting field-effect transistors (LEFETs) are emerging optoelectronic devices able to display simultaneously electrical switching as transistors and electroluminescence emission as light emitting diodes. Lead chalcogenide colloidal quantum dots (CQDs) allow achieving light emission in a very broad spectral range, covering the near-infrared (NIR) and the short-wavelength infrared (SWIR) regions, which cannot be reached with other solution-processable materials. Therefore, the use of lead chalcogenide CQDs as active layer in LEFETs opens the possibility for very narrow and switchable light sources in the NIR and SWIR range. The recently reported, first fully solid-state lead chalcogenide (PbS) CQD based LEFET shows an electroluminescence (EL) quantum efficiency of 1.3×10^{-5} at room temperature and of about 1% below 100 K. To overcome the limits of a previous report, an active material comprising two sequentially deposited layers is designed, the first of PbS CQDs displaying n-type transport and the second of polymer-wrapped semiconducting carbon nanotubes displaying p-type dominated transport. With this double layer system, LEFETs displaying a well-balanced ambipolar transport, charge carrier mobility of about 0.2 $cm^2 V^{-1} s^{-1}$ for both electrons and holes, and EL external quantum efficiency reaching 1.2×10^{-4} at room temperature are obtained.

1. Introduction

Colloidal quantum dots (CQDs) are solution-processable nanomaterials which have great potential for many applications in optoelectronics. Among the most desired properties are the large spectral tunability by size, the outstanding monodispersity and therefore color purity as well as the solution processability.[1–3] Due to the quantum confinement effect, the energetic position of the emission can be easily adjusted by tuning the size of the particles,[4] and their monodispersity give rise to a single narrow emission peak, which is at the base of their application in display technology (vide infra). Interestingly, the emission of CQDs can readily be extended to the near-infrared region (750–2500 nm) by using, for example, semiconductors display very narrow band gap in bulk, such as metal chalcogenides such as PbS and PbSe.[5] Near-infrared light has many important applications

D. Bederak,[+] A. Shulga,[+] S. Kahmann,[++] W. Talsma, J. Pelanskis, M. A. Loi
Zernike Institute for Advanced Materials
University of Groningen
Nijenborgh 4, Groningen 9747AG, The Netherlands
E-mail: m.a.loi@rug.nl

The ORCID identification number(s) for the author(s) of this article can be found under https://doi.org/10.1002/aelm.202101126.

[+]Present address: QDI Systems BV, L.J. Zielstraweg 1, Groningen 9713 GX, The Netherlands
[++]Present address: Cavendish Laboratory, University of Cambridge, Cambridge CB3 0HE, UK

DOI: 10.1002/aelm.202101126

D. N. Dirin, M. V. Kovalenko
Department of Chemistry and Applied Biosciences
ETH Zürich
Vladimir Prelog Weg 1, Zürich 8093, Switzerland
D. N. Dirin, M. V. Kovalenko
Empa-Swiss Federal Laboratories for Materials Science and Technology
Uberlandstrasse 129, Dübendorf 8600, Switzerland

such as navigation, night vision, and telecommunication.[6] However, the near-infrared (NIR) region is not readily and cost-effectively covered by traditional inorganic semiconductors; and the organic semiconductor contenders in this spectral region remain rather elusive.[7]

NIR light-emitting devices are therefore an important avenue for applications of CQDs. Typically, electroluminescent devices use the light-emitting diode (LED) configuration, which have shown great improvement in the last years.[8] However, in the context of downscaling the pixels, a different device geometry emerges as an attractive alternative, namely light-emitting field-effect transistors (LEFETs), which offer the possibility to combine electroluminescence generation and electrical switching function within one device.[6]

The first NIR-emitting LEFET based on CQDs (CQD LEFET) was based on PbS.[9] This device employed a film of PbS CQDs capped with 3-mercaptopropionic acid (MPA) and was gated with an ion gel. The maximum external quantum efficiency (EQE) was reported to be 2×10^{-5}, which was comparable with the one of LEDs fabricated with the same material at the time of publication. The next notable step was an ambipolar CQD LEFET based on PbS CQDs capped with tetrabutylammonium iodide (TBAI), which used a solid gate dielectric.[10] Iodide ligands provide better passivation of the CQD surface than MPA, leading to an improvement of the electroluminescence EQE up to 1.3×10^{-5} at room temperature and of 1% below 100K. Importantly, these results were obtained using a device structure with a solid-state gate dielectric having a lower capacitance than the ion gel used in the above-mentioned pioneering work (vide infra).

However, two common issues are limiting the device performance in both above-mentioned PbS CQD LEFETs: i) the layer-by-layer approach used for the CQD film deposition and ii) the unbalanced ambipolar charge transport of the active layer.

The layer-by-layer deposition has been a widely employed method for the formation of conductive CQD films by replacing the long insulating native ligands with shorter ones using a solid-state reaction.[11] Besides being a time-intensive and wasteful process, this method leads to defects in the film and the formation of trap states at the CQD surface, which deteriorate both the light-emission properties and the charge transport in the active layer.[12] Recently, a new method has been developed to substitute the long insulating native ligands, the so-called phase-transfer ligand exchange (PTLE), which allows to make a stable colloidal dispersion (an ink) of QDs decorated by short ligands.[13,14] This ink can then be used for a single-step deposition of conductive CQD films by various techniques and thus is much more attractive for the development of CQD-based technologies.[15,16]

The second problem is much more fundamental. The majority of PbS CQDs synthetic methods result in nonstoichiometric, Pb-rich particles,[17–19] which give rise to n-type behavior of the films.[20] It has been demonstrated that tuning the size of the CQDs and changing the nature of the capping ligands the degree of the n-doping can be adjusted,[21] but obtaining PbS CQD films with highly balanced ambipolar transport from an ink is still an open challenge.

Here we demonstrated the first PbS CQD LEFET fabricated from colloidally ligand-exchanged inks, consisting of PbS CQDs capped with the widely used methylammonium lead iodide-like coating. We utilized a bilayer structure where on top of the n-type CQD film we deposited a network of polymer wrapped single-walled semiconducting carbon nanotubes (CNTs).[22,23] The heterostructure shows a well-balanced ambipolar transport and almost identical hole and electron linear mobilities (0.2 $cm^2\ V^{-1}\ s^{-1}$). The EQE of the resulting device was found to be 1.2×10^{-4}, which is almost an order of magnitude higher compared to the previously reported PbS CQD LEFETs.

2. Results and Discussion

The CQD LEFETs were fabricated on borosilicate glass substrates where gold source/drain electrodes were lithographically defined and the gate dielectric (PMMA/Al_2O_3) and electrode were deposited on top of the active layer, defining a bottom contact/top gate FET configuration (see schematic in **Figure 1**A). The CQD active layer was deposited by spin-coating an ink of methylammonium lead iodide ($MAPbI_3$) coated PbS CQDs in 2,6-difluoropyridine (DFP). This is, to our knowledge, the first example of CQD LEFETs fabricated using a CQD ink, namely without using the layer-by-layer coating method. $MAPbI_3$ coating provides efficient electronic passivation of PbS CQDs and photoluminescence quantum yield of PbS-$MAPbI_3$ inks is 20–30%, comparable with the quantum yields of CQDs capped with oleic acid before the ligand exchange.[24–26] The TEM image of the PbS-$MAPbI_3$ CQDs is shown in Figure S1 (Supporting Information).

DFP is chosen as a solvent because it allows high colloidal stability of the PbS-$MAPbI_3$ CQDs ink.[27] As mentioned, the gate dielectric is deposited onto the CQD film and consists of 10 nm of poly(methyl methacrylate) (PMMA) deposited by spin coating and 80 nm of Al_2O_3, grown by atomic layer deposition (ALD). The PMMA interlayer is necessary to prevent chemical degradation of the CQDs upon exposure to the highly reactive trimethylaluminum during the ALD of Al_2O_3.[10] Also, the thin PMMA layer serves as an adhesion layer between the CNTs network and the oxide layer and ensures a low density of trap states at the semiconductor-dielectric interface.[28] Finally, the device is finished by evaporating the gate electrode through a shadow mask (see Figure S2, Supporting Information, for the optical images of devices). The fabrication of CQD-CNTs LEFETs differed only in the deposition by blade-coating of a CNTs network onto the CQD film. Excellent compatibility of CQDs and CNTs as a complementary pair of semiconducting materials was previously shown during the fabrication of high-performance ambipolar inverters.[29] The CNTs ink consists of poly(3-dodecylthiophene-2,5-diyl)-wrapped (P3DDT) semiconducting CNTs, prepared by using our previously published method.[30] P3DDT-wrapped semiconducting CNTs exhibit strong p-type electronic transport properties but depending in the preparation method they can still show a substantial electron mobility.[23,31] More details on CQD ink preparation and device fabrication can be found in the Experimental section.

The output characteristics of LEFETs fabricated using solely PbS-$MAPbI_3$ as active layer reveal ambipolar transport with the dominance of negative charge carriers (Figure 1B). The transfer curves (Figure 1C) show more clearly the strongly electron-dominated ambipolar transport, with a linear electron mobility of about 5.2×10^{-3} $cm^2\ V^{-1}\ s^{-1}$ which is in a good agreement with literature reports.[27,32] The meaningful values of hole

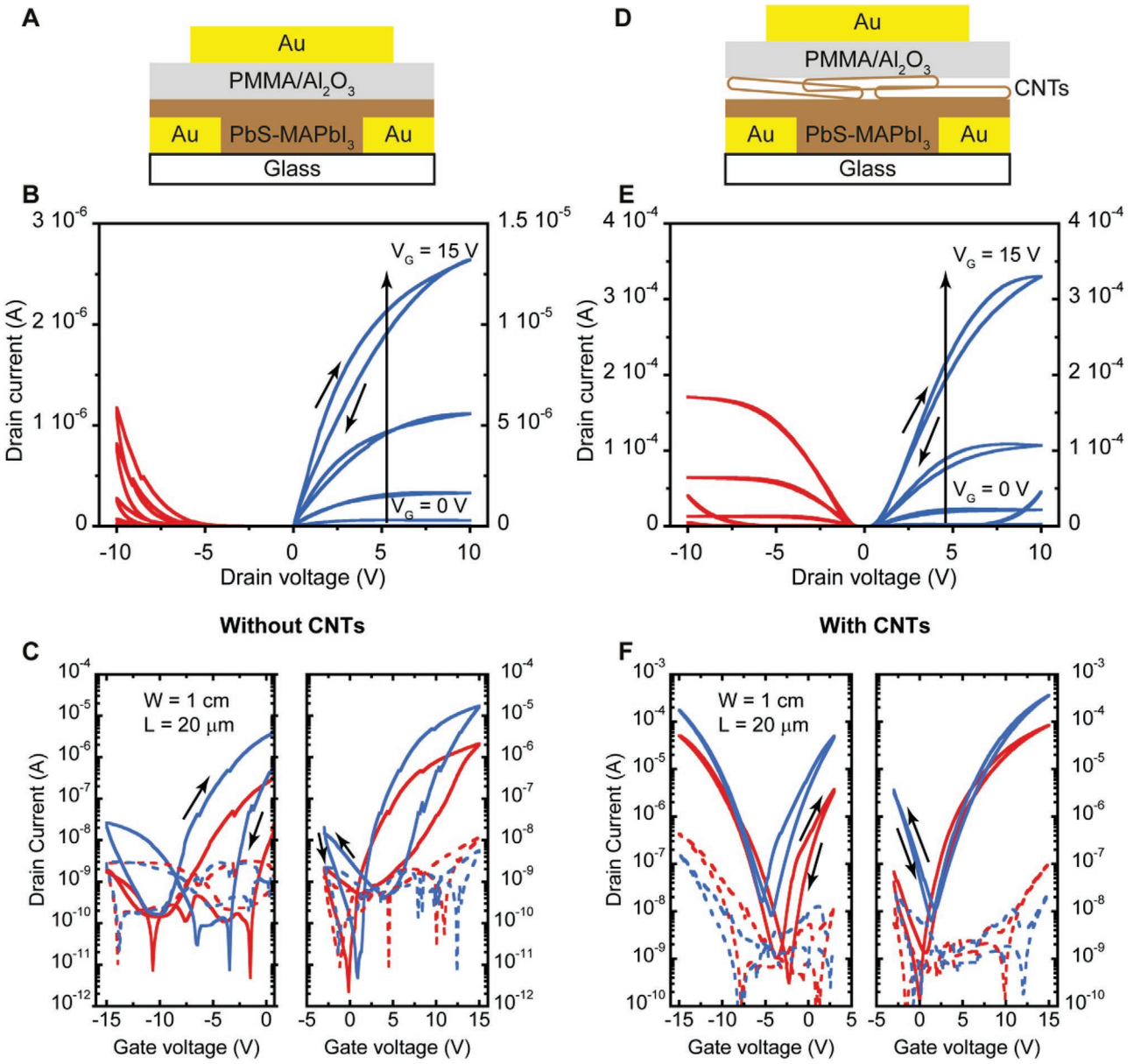

Figure 1. A) Schematic of CQD LEFET and B) resulting output characteristics. C) Transfer characteristics of CQD LEFETs, the sweeps are measured at drain voltage equal to 2 V (red) and 5 V (blue). Dashed lines represent the gate current D) schematic of CQD-CNTs LEFET and E) resulting output characteristics. F) Transfer characteristics of CQD-CNTs LEFETs, the sweeps are measured at drain voltage equal to 2 V (red) and 5 V (blue). Dashed lines represent the gate current.

mobility could not be extracted because the drain current and gate leakage current were comparable. The fabrication of LEFETs with an active layer with such imbalanced electron and hole transport will hamper the possibility to achieve high electroluminescence quantum efficiency. It has been demonstrated in the case of organic semiconductors, that more balanced mobilities and therefore better LEFETs could be achieved when blending hole and electron transport materials[33,34] or when a heterostructure of the two is fabricated.[35]

We therefore adopted a similar strategy by fabricating a heterostructure using the electron transporting PbS-$MAPbI_3$ and the hole transporting polymer-wrapped CNTs.

The schematic structure of the CQD-CNTs LEFETs is shown in Figure 1D. A network of polymer-wrapped semiconducting nanotubes is deposited on top of the CQD layer before the gate dielectric. This is possible due to the orthogonality of the solvents employed for the deposition of the two semiconductors (DFP and *o*-xylene for the CQDs and the CNTs, respectively).

When the gate voltage is applied, the conductive channel is created nearby the gate dielectric. As the CNT layer has a thickness of few nanometers, the channel is formed at the interface between the two materials, involving both of them in the transport (vide infra).[36] This results in almost ideally balanced ambipolar output characteristics (Figure 1E). The

hole channel's saturation current becomes almost equal to the one of the electron channel for the same absolute value of the gate voltage. This is important because the working principle of LEFETs is based on the creation of an ambipolar regime, when one electrode injects holes and the other electrons into the channel.[6] Recombination of electrons and holes with subsequent light emission occurs at the meeting point of two subchannels (recombination zone). Even taking into account the unavoidable diffusion, the recombination zone of LEFETs is typically much narrower than the width of the transistor channel.[10] The position of the recombination zone in the channel can be moved by tuning the applied drain and gate voltages. This confirms the "truly ambipolar" nature of a device with coexisting electron and hole channels which is essential for light-emission efficiency.[37] Positioning the recombination zone further away from the electrodes helps to suppress electrode-induced exciton recombination as well as carrier extraction at the electrodes.[6,37,38]

Figure 1F shows the transfer characteristics of the CQD-CNT LEFETs representing a typical V-shape transfer curve for ambipolar transistors and confirming the well-balanced transport of the device. The inclusion of the CNTs resulted in more balanced characteristics, higher drain current and similar on/off current ratio for both charge carriers. Furthermore, the position of the off state in the CQD-CNT LEFETs is almost equal for forward and reverse scanning directions, which is not the case for CQD devices that are affected by large hysteresis. Noteworthy, the hysteresis in the CQD-CNT device is much less pronounced, especially for holes. Such a small hysteresis for holes is atypical for PbS CQD films, which usually display

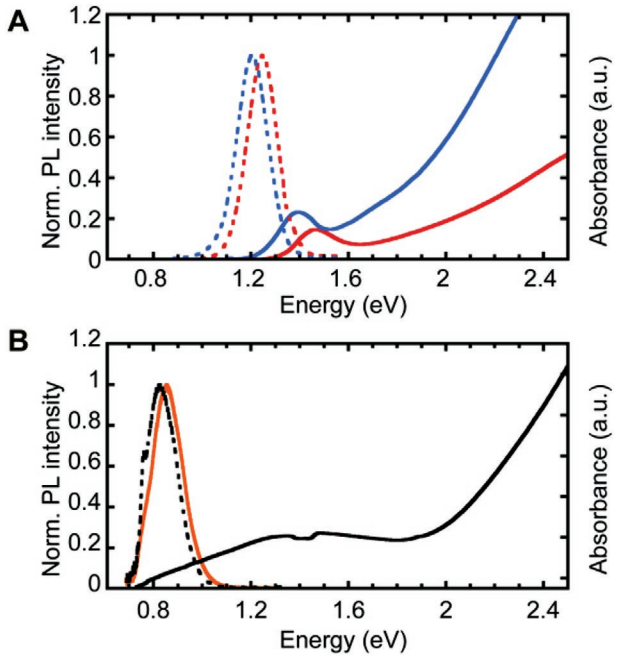

Figure 2. A) Absorption and photoluminescence spectra of oleate-capped PbS CQDs in hexane (red solid and dashed lines) and capped with $MAPbI_3$ in DFP (blue solid and dashed lines). B) Absorption and photoluminescence spectra of CQD-CNT heterostructure (black solid and dashed lines) as well as electroluminescence spectrum of CQD-CNT LEFETs (orange).

pronounced hole trapping. This is a further indication that the hole transport in our heterostructure is occurring through the CNT network. The extracted values of the linear mobility for holes and electrons are about 0.2 $cm^2\ V^{-1}\ s^{-1}$, which shows 2 orders of magnitude enhancement of the electron mobility compared to those obtained for PbS CQD only LEFET. The increase of the electron mobility should also be assign to the beneficial role of the CNTs, transistors made with similar CNT inks display hole mobility of 1 $cm^2\ V^{-1}\ s^{-1}$ and electron mobility of 0.4 $cm^2\ V^{-1}\ s^{-1}$.[30]

When considering electroluminescent devices, the optical properties of the emitting material need special attention. The summary of the optical properties of the employed PbS CQDs is shown in **Figure 2**A. The starting dispersion of PbS CQDs capped with native oleic acid (OA) ligands in hexane has the first excitonic peak position at 1.47 eV. Upon ligand-exchange with $MAPbI_3$ and redispersion in DFP, this peak shifts to 1.4 eV, which is typically explained by the difference in dielectric permittivity of the solvents (1.9 for hexane and 107.8 for DFP) and lowering of the quantum confinement of the CQDs after the ligand exchange.[27,39] The same trend is observed with the emission spectra.

The emission spectrum of the CQD-CNT heterostructure shows a single peak originating from the CQD layer (Figure 2B), while the emission of the CNTs is not detectable (see Figure S3, Supporting Information; the emission spectrum of CNTs has a series of distinct sharp peaks due to the presence of CNTs with different diameter and thus different bandgap). This is due to the very small amount of CNTs present in the ≈3–6 nm layer and their limited quantum yield, which is much lower than the one of the CQD layer.[40,41]

The CQD-CNT film exhibits the maximum photoluminescence at 0.83 eV (Figure 2B). The origin of such a pronounced red-shift of the emission in films compared to the one from the ink is attributed to the further loss of quantum confinement of CQDs at the elevated temperature of the deposition process.[42,43] The absorption spectrum of the CQD-CNT film is shown in Figure 2B. The spectrum shows a large broadening in the low energy region, most probably attributable to the weakening of the quantum confinement.[10,42]

The CQD film is subjected to elevated temperature during the blade-coating deposition of the CNTs (70 °C), the ALD dielectric growth ($T = 100$ °C) and the post-annealing of the device, which is performed at 140 °C. The feature at 0.75 eV in the emission spectrum is an artifact originated by the drop of the sensitivity of the detectors for low energy photons. It is useful to note that PbS-$MAPbI_3$ ink in DFP and the corresponding CQD film show almost identical full width at half-maximum of the emission peaks (0.22 eV).

The EL maximum for the CQD-CNT LEFET is at 0.86 eV (Figure 2B). The small discrepancy between the peak positions of the electro- and photoluminescence can likely be explained by the state filling of the transport levels at higher carried densities.[10] We note that in line with their inferior electrical properties, LEFETs solely comprising CQDs in the active layer only offer faint EL.

The dependence of the drain current versus the gate voltage is shown in **Figure 3**A. The light-emission measurements were performed inside a dark chamber, where the LEFET was placed right onto the calibrated photodiode and was electrically

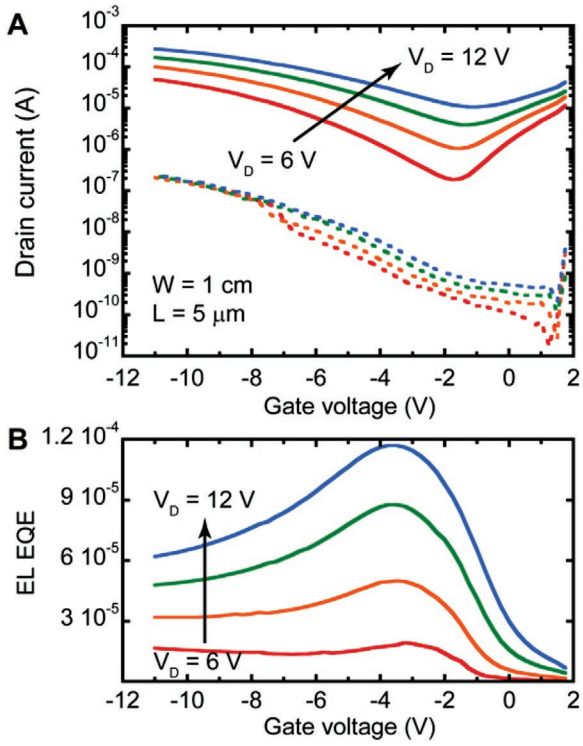

Figure 3. A) Drain current of the CQD-CNT LEFET versus the gate voltage (solid lines) and gate leakage current (dashed lines). B) EQE of electroluminescence of the same device as a function of the applied electrode potentials.

connected via probes to the semiconducting analyzer.[9] This measurement configuration obviously underestimates the EQE due to impossibility to collect all the emitted light in the used geometry. The maximum light emission in the device was measured by applying a positive drain voltage and negative gate bias (Figure 3B). The absolute value of the EQE increases with the applied drain voltage, fact previously attributed to the filing of the trap states in the channel.[10] The maximum value measured for the EQE is 1.2×10^{-4} which is almost an order of magnitude higher compared to the previous record in NIR-emitting CQD-based LEFETs at room temperature (see **Table 1**).

This improvement of the EL EQE is determined by the combination of two factors. First, the balanced ambipolar charge transport achieved combining the n-type CQD layer with the p-type dominated polymer-wrapped semiconducting CNTs layer. Second, the utilization of liquid phase-transfer ligand exchange instead of the layer-by-layer solid-state reaction, which exhibit improved surface passivation of CQDs.

3. Conclusions

By combining an n-type layer of PbS CQDs with a p-type layer of polymer-wrapped semiconducting CNTs we obtained a well-balanced ambipolar transport, which show to be key to improve the external quantum efficiency of the light-emitting device. Linear hole and electron mobilities up to 0.2 $cm^2\ V^{-1}\ s^{-1}$ are measured in the heterostructure using $PMMA/Al_2O_3$ as gate dielectric. These devices exhibited electroluminescence emission maximum at 0.86 eV (1440 nm), with maximum external quantum efficiency of the electroluminescence is 1.2×10^{-4}, that is almost an order of magnitude higher compared to previous reports on PbS CQD LEFETs. Interestingly, while the CNTs appear very important for the electrical performance of the device, we did not find measurable signature of their EL.

Future work should focus on optimization of CQD LEFET structure to favor light extraction and to apply strategies to reduce trapping states.

4. Experimental Section

PbS CQDs Synthesis: All the solvents and reagents were analytically pure and were used without further purification. Synthesis and isolation of PbS CQDs capped with oleic acid was performed by using a hot-injection method as described except for the amount of OA (56 mL instead of 70 mL) and injection at a lower temperature (80 °C).[44]

Preparation of the Inks: Solution-phase ligand exchange was performed by using a previously published method.[27] $MAPbI_3$ solution in *N*-methylformamide was prepared by mixing PbI_2 and MAI in 1:1 molar ratio. In a typical procedure, 10 mL of *N*-methylformamide solution of 50×10^{-3} M $MAPbI_3$ was combined with 10 mL of oleate-capped PbS CQDs in hexanes with a concentration of 5 mg mL^{-1}. The mixture was stirred by using a magnetic stirring bar until all the CQDs are transferred into a polar phase. Then the top phase was discarded and the bottom phase was washed thrice with hexanes. Ligand-exchanged CQDs were precipitated by addition of acetone, collected by centrifugation and finally re-dispersed in DFP to form an ink. For electron microcopy analyses, the diluted ink was dropcasted on a carbon-coated copper grid. The images were recorded with a double aberration corrected FEI Themis Z microscope operated at 300 kV using the previously reported parameters.[42]

Device Fabrication: 0.7 mm thick borosilicate glass substrates were cleaned with detergent and then consequently ultrasonicated in deionized water, acetone and isopropanol and dried in oven at 120 °C for at least 20 min. Then the source and drain electrodes consisting from 3 nm of Ti and 37 nm of Au were patterned by using UV lithography. The substrates were treated with O_2-plasma for 3 min before the CQD film deposition. CQD film was deposited by spin-coating PbS-$MAPbI_3$ ink in DFP inside the N_2-filled glove box at 1000 rpm resulting in about 50 nm film. A network of semiconducting CNTs was deposited by blade-coating two layers of CNT ink at 70 °C with 3 mm s^{-1} blade speed. The CNT ink consisted of poly(3-dodecylthiophene-2,5-diyl)-wrapped (P3DDT) semiconducting CNTs and was prepared using the method as described

Table 1. Overview of the performance and device structure of the NIR-emitting CQD-based LEFETs.

Active layer	EL max [nm]	EQE	Dielectric	Mobility [$cm^2\ V^{-1}\ s^{-1}$]	Reference
PbS-MPA	≈1480	2×10^{-5}	[EMIM][FAP]	μ_h = 0.003–0.009 μ_e = 0.04–0.06	[9]
PbS-TBAI	1480	1.3×10^{-5}	$PMMA/Al_2O_3$	μ_h undetermined μ_e = 0.06	[10]
PbS-$MAPbI_3$/CNTs	1490	1.2×10^{-4}	$PMMA/Al_2O_3$	μ_h = 0.2 μ_e = 0.2	This work

in a previously published work.[30] Such deposition conditions results in in the ≈3–6 nm layer on a flat SiO_2 surface. Then an ≈10 nm PMMA layer was spin-coated from 6 mg mL^{-1} solution in acetonitrile at 3000 rpm and dried on a hotplate for 1 min at 120 °C. The gate dielectric was finished by growing 80 nm of aluminum oxide at 100 °C by atomic layer deposition from trimethylaluminum and water precursors (Picosun R200 advanced deposition system). Finally, the device fabrication was finished by thermal evaporation of gold gate electrode through a shadow mask. The device was annealed for 20 min at 140 °C inside the N_2-filled glove box.

LEFET Characterization: The capacitance of the gate dielectric on indium tin oxide (ITO)/PMMA/Al_2O_3/Al devices was measured using Solarton 1260 impedance gain-phase analyzer. Electrical characterization of the CQD LEFET was done using a Keithley 4200-SCS semiconductor parameter analyzer. Absorption spectra were recorded using a Shimadzu UV-3600 spectrometer. Electroluminescence and photoluminescence spectra were collected using a spectrometer and recorded by an Andor iDus 1.7 µm InGaAs camera. PL spectra were measured by exciting the sample with the second harmonic (400 nm) of a mode-locked Ti:sapphire laser (Mira 900, Coherent). For the EQE measurements, the response of calibrated photodiode to the emitted light from the LEFETs was measured. The EQE was calculated by using the following formula

$$EQE = \frac{I_{diode}}{I_d} \cdot \frac{1}{S_{av}} \cdot \frac{e}{hc} \cdot \frac{\int \lambda \cdot EL_{norm}(\lambda) d\lambda}{\int EL_{norm}(\lambda) d\lambda} \quad (1)$$

where I_{diode} is the recorded current by a calibrated photodiode and S_{av} is the average sensitivity of this photodiode, I_d is the source-drain current of a transistor.

Supporting Information

Supporting Information is available from the Wiley Online Library or from the author.

Acknowledgements

The authors are thankful to A. Kamp and T. Zaharia for the technical support. The Groningen team is grateful for the financial support of the Dieptestrategie program from Zernike Institute for Advanced Materials. This work was financed through the Materials for Sustainability (Mat4Sus) program (739.017.005) of the Netherlands Organisation for Scientific Research (NWO). S.K. acknowledges the Deutsche Forschungsgemeinschaft (DFG) for a postdoctoral research fellowship (408012143).

Conflict of Interest

The authors declare no conflict of interest.

Data Availability Statement

Research data are not shared.

Keywords

carbon nanotubes, colloidal quantum dots, electroluminescence, field-effect transistors, lead sulfide, light emission

Received: October 15, 2021
Revised: January 25, 2022
Published online: February 25, 2022

[1] C. B. Murray, C. R. Kagan, M. G. Bawendi, *Annu. Rev. Mater. Sci.* **2000**, *30*, 545.
[2] D. V. Talapin, J.-S. Lee, M. V. Kovalenko, E. V. Shevchenko, *Chem. Rev.* **2010**, *110*, 389.
[3] C. R. Kagan, E. Lifshitz, E. H. Sargent, D. V. Talapin, *Science* **2016**, *353*, aac5523.
[4] M. A. Hines, G. D. Scholes, *Adv. Mater.* **2003**, *15*, 1844.
[5] I. Moreels, Y. Justo, B. De Geyter, K. Haustraete, J. C. Martins, Z. Hens, *ACS Nano* **2011**, *5*, 2004.
[6] S. Kahmann, A. Shulga, M. A. Loi, *Adv. Funct. Mater.* **2019**, *30*, 1904174.
[7] H. Lu, G. M. Carroll, N. R. Neale, M. C. Beard, *ACS Nano* **2019**, *13*, 939.
[8] S. Pradhan, F. Di Stasio, Y. Bi, S. Gupta, S. Christodoulou, A. Stavrinadis, G. Konstantatos, *Nat. Nanotechnol.* **2019**, *14*, 72.
[9] J. Schornbaum, Y. Zakharko, M. Held, S. Thiemann, F. Gannott, J. Zaumseil, *Nano Lett.* **2015**, *15*, 1822.
[10] A. G. Shulga, S. Kahmann, D. N. Dirin, A. Graf, J. Zaumseil, M. V. Kovalenko, M. A. Loi, *ACS Nano* **2018**, *12*, 12805.
[11] H. Beygi, S. A. Sajjadi, A. Babakhani, J. F. Young, F. C. J. M. van Veggel, *Appl. Surf. Sci.* **2018**, *459*, 562.
[12] D. M. Balazs, M. A. Loi, *Adv. Mater.* **2018**, *30*, 1800082.
[13] M. V. Kovalenko, M. Scheele, D. V. Talapin, *Science* **2009**, *324*, 1417.
[14] A. Fischer, L. Rollny, J. Pan, G. H. Carey, S. M. Thon, S. Hoogland, O. Voznyy, D. Zhitomirsky, J. Y. Kim, O. M. Bakr, E. H. Sargent, *Adv. Mater.* **2013**, *25*, 5742.
[15] J. Jean, J. Xiao, R. Nick, N. Moody, M. Nasilowski, M. Bawendi, V. Bulović, *Energy Environ. Sci.* **2018**, *11*, 2295.
[16] Q. Lin, H. J. Yun, W. Liu, H.-J. Song, N. S. Makarov, O. Isaienko, T. Nakotte, G. Chen, H. Luo, V. I. Klimov, J. M. Pietryga, *J. Am. Chem. Soc.* **2017**, *139*, 6644.
[17] M. A. M. A. Hines, G. D. G. D. Scholes, *Adv. Mater.* **2003**, *15*, 1844.
[18] M. P. Hendricks, M. P. Campos, G. T. Cleveland, I. Jen-La Plante, J. S. Owen, *Science* **2015**, *348*, 1226.
[19] L. Cademartiri, E. Montanari, G. Calestani, A. Migliori, A. Guagliardi, G. A. Ozin, *J. Am. Chem. Soc.* **2006**, *128*, 10337.
[20] D. Kim, D.-H. Kim, J.-H. Lee, J. C. Grossman, *Phys. Rev. Lett.* **2013**, *110*, 196802.
[21] P. R. Brown, D. Kim, R. R. Lunt, N. Zhao, M. G. Bawendi, J. C. Grossman, V. Bulović, *ACS Nano* **2014**, *8*, 5863.
[22] J. M. Salazar-Rios, W. Talsma, V. Derenskyi, W. Gomulya, T. Keller, M. Fritsch, S. Kowalski, E. Preis, M. Wang, S. Allard, G. C. Bazan, U. Scherf, M. C. dos Santos, M. A. Loi, *Small Methods* **2018**, *2*, 1700335.
[23] V. Derenskyi, W. Gomulya, J. M. S. Rios, M. Fritsch, N. Fröhlich, S. Jung, S. Allard, S. Z. Bisri, P. Gordiichuk, A. Herrmann, U. Scherf, M. A. Loi, *Adv. Mater.* **2014**, *26*, 5969.
[24] D. N. Dirin, S. Dreyfuss, M. I. Bodnarchuk, G. Nedelcu, P. Papagiorgis, G. Itskos, M. V. Kovalenko, *J. Am. Chem. Soc.* **2014**, *136*, 6550.
[25] Z. Yang, J. Z. Fan, A. H. Proppe, F. P. G. De Arquer, D. Rossouw, O. Voznyy, X. Lan, M. Liu, G. Walters, R. Quintero-Bermudez, B. Sun, S. Hoogland, G. A. Botton, S. O. Kelley, E. H. Sargent, *Nat. Commun.* **2017**, *8*, 1325.
[26] W. Wang, M. Zhang, Z. Pan, G. M. Biesold, S. Liang, H. Rao, Z. Lin, X. Zhong, *Chem. Rev.* **2021**, acs. chemrev.1c00478.
[27] D. Bederak, N. Sukharevska, S. Kahmann, M. Abdu-Aguye, H. Duim, D. N. Dirin, M. V. Kovalenko, G. Portale, M. A. Loi, *ACS Appl. Mater. Interfaces* **2020**, *12*, 52959.
[28] M. Held, S. P. Schießl, D. Miehler, F. Gannott, J. Zaumseil, *Appl. Phys. Lett.* **2015**, *107*, 083301.
[29] A. G. Shulga, V. Derenskyi, J. M. Salazar-Rios, D. N. Dirin, M. Fritsch, M. V. Kovalenko, U. Scherf, M. A. Loi, *Adv. Mater.* **2017**, *29*, 1701764.

[30] W. Talsma, A. A. Sengrian, J. M. Salazar-Rios, H. Duim, M. Abdu-Aguye, S. Jung, S. Allard, U. Scherf, M. A. Loi, *Adv. Electron. Mater.* **2019**, *5*, 1900288.
[31] S. Z. Bisri, J. Gao, V. Derenskyi, W. Gomulya, I. Iezhokin, P. Gordiichuk, A. Herrmann, M. A. Loi, *Adv. Mater.* **2012**, *24*, 6147.
[32] D. M. Balazs, N. Rizkia, H.-H. H. Fang, D. N. Dirin, J. Momand, B. J. Kooi, M. V. Kovalenko, M. A. Loi, *ACS Appl. Mater. Interfaces* **2018**, *10*, 5626.
[33] M. A. Loi, C. Rost-Bietsch, M. Murgia, S. Karg, W. Riess, M. Muccini, *Adv. Funct. Mater.* **2006**, *16*, 41.
[34] C. Rost, S. Karg, W. Riess, M. A. Loi, M. Murgia, M. Muccini, *Appl. Phys. Lett.* **2004**, *85*, 1613.
[35] F. Dinelli, R. Capelli, M. A. Loi, M. Murgia, M. Muccini, A. Facchetti, T. J. Marks, *Adv. Mater.* **2006**, *18*, 1416.
[36] A. G. Shulga, L. Piveteau, S. Z. Bisri, M. V. Kovalenko, M. A. Loi, *Adv. Electron. Mater.* **2016**, *2*, 1500467.
[37] J. Zaumseil, R. H. Friend, H. Sirringhaus, *Nat. Mater.* **2006**, *5*, 69.
[38] C. Santato, R. Capelli, M. A. Loi, M. Murgia, F. Cicoira, V. A. L. Roy, P. Stallinga, R. Zamboni, C. Rost, S. F. Karg, M. Muccini, *Synth. Met.* **2004**, *146*, 329.
[39] T. Takagahara, *Phys. Rev. B* **1993**, *47*, 4569.
[40] W. Gomulya, G. D. Costanzo, E. J. F. de Carvalho, S. Z. Bisri, V. Derenskyi, M. Fritsch, N. Fröhlich, S. Allard, P. Gordiichuk, A. Herrmann, S. J. Marrink, M. C. dos Santos, U. Scherf, M. A. Loi, *Adv. Mater.* **2013**, *25*, 2948.
[41] X. Wei, T. Tanaka, S. Li, M. Tsuzuki, G. Wang, Z. Yao, L. Li, Y. Yomogida, A. Hirano, H. Liu, H. Kataura, *Nano Lett.* **2020**, *20*, 410.
[42] N. Sukharevska, D. Bederak, V. M. Goossens, J. Momand, H. Duim, D. N. Dirin, M. V. Kovalenko, B. J. Kooi, M. A. Loi, *ACS Appl. Mater. Interfaces* **2021**, *13*, 5195.
[43] S. Kahmann, M. A. Loi, *Appl. Phys. Rev.* **2020**, *7*, 041305.
[44] M. Yarema, O. Yarema, W. M. M. Lin, S. Volk, N. Yazdani, D. Bozyigit, V. Wood, *Chem. Mater.* **2017**, *29*, 796.